

# Polymer-Based Nano/ Composites: Theory, Synthesis, Modifications, and Properties

Guest Editors: Mircea Chipara, Alan K. T. Lau,  
Mahmood Aliofkhazraei, Angel Romo-Urbe, and Ehsan Bafekrpour





---

# **Polymer-Based Nano/Composites: Theory, Synthesis, Modifications, and Properties**

# **Polymer-Based Nano/Composites: Theory, Synthesis, Modifications, and Properties**

Guest Editors: Mircea Chipara, Alan K. T. Lau,  
Mahmood Aliofkhazraei, Angel Romo-Uribe,  
and Ehsan Bafekrpour



---

Copyright © 2015 Hindawi Publishing Corporation. All rights reserved.

This is a special issue published in "Journal of Nanomaterials." All articles are open access articles distributed under the Creative Commons Attribution License, which permits unrestricted use, distribution, and reproduction in any medium, provided the original work is properly cited.

## Editorial Board

Domenico Acierno, Italy  
Katerina Aifantis, USA  
Sheikh Akbar, USA  
Nageh K. Allam, USA  
Margarida Amaral, Portugal  
Martin Andersson, Sweden  
Raul Arenal, Spain  
Ilaria Armentano, Italy  
Vincenzo Baglio, Italy  
Lavinia Balan, France  
Thierry Baron, France  
Andrew R. Barron, USA  
Reza Bayati, USA  
Hongbin Bei, USA  
Daniel Bellet, France  
Stefano Bellucci, Italy  
Enrico Bergamaschi, Italy  
Samuel Bernard, France  
D. Bhattacharyya, New Zealand  
Sergio Bietti, Italy  
Giovanni Bongiovanni, Italy  
Theodorian Borca-Tasciuc, USA  
Mohamed Bououdina, Bahrain  
Torsten Brezesinski, Germany  
C. Jeffrey Brinker, USA  
Christian Brosseau, France  
Philippe Caroff, Australia  
Victor M. Castaño, Mexico  
Albano Cavaleiro, Portugal  
Bhanu P. S. Chauhan, USA  
Shafiul Chowdhury, USA  
Jin-Ho Choy, Korea  
Kwang-Leong Choy, UK  
Yu-Lun Chueh, Taiwan  
Elisabetta Comini, Italy  
Giuseppe Compagnini, Italy  
David Cornu, France  
Miguel A. Correa-Duarte, Spain  
P. Davide Cozzoli, Italy  
Shadi A. Dayeh, USA  
Luca Deseri, USA  
Yong Ding, USA  
Philippe Dubois, Belgium  
Alain Dufresne, France  
Zehra Durmus, Turkey  
Joydeep Dutta, Oman  
Ali Eftekhari, USA  
Jeffrey Elam, USA  
Samy El-Shall, USA  
Ovidiu Ersen, France  
Claude Estournès, France  
Andrea Falqui, KSA  
Matteo Ferroni, Italy  
E. Johan Foster, USA  
Ilaria Fratoddi, Italy  
Wolfgang Fritzsche, Germany  
Alan Fuchs, USA  
Miguel A. Garcia, Spain  
Siddhartha Ghosh, Singapore  
P. K. Giri, India  
Russell E. Gorga, USA  
Jihua Gou, USA  
Jean M. Greneche, France  
Smrati Gupta, Germany  
Kimberly Hamad-Schifferli, USA  
Simo-Pekka Hannula, Finland  
Michael Harris, USA  
Yasuhiko Hayashi, Japan  
F. Hernandez-Ramirez, Spain  
Michael Z. Hu, USA  
Nay Ming Huang, Malaysia  
Shaoming Huang, China  
David Hui, USA  
Zafar Iqbal, USA  
Balachandran Jeyadevan, Japan  
Xin Jiang, Germany  
Rakesh Joshi, Australia  
Jeong-won Kang, Korea  
Hassan Karimi-Maleh, Iran  
Antonios Kelarakis, UK  
Alireza Khataee, Iran  
Ali Khorsand Zak, Iran  
Philippe Knauth, France  
Ralph Krupke, Germany  
Christian Kübel, Germany  
Prashant Kumar, UK  
Michele Laus, Italy  
Eric Le Bourhis, France  
Burtrand Lee, USA  
Jun Li, Singapore  
Meiyong Liao, Japan  
Shijun Liao, China  
Silvia Licocchia, Italy  
Wei Lin, USA  
Nathan C. Lindquist, USA  
Jun Liu, USA  
Zainovia Lockman, Malaysia  
Nico Lovergine, Italy  
Jim Low, Australia  
Jue Lu, USA  
Songwei Lu, USA  
Ed Ma, USA  
Laura M. Maestro, Spain  
Gaurav Mago, USA  
Muhamamd A. Malik, UK  
Devanesan Mangalaraj, India  
Sanjay R. Mathur, Germany  
Tony McNally, UK  
Yogendra Mishra, Germany  
Paulo Cesar Morais, Brazil  
Paul Munroe, Australia  
Jae-Min Myoung, Korea  
Rajesh R. Naik, USA  
Albert Nasibulin, Russia  
Toshiaki Natsuki, Japan  
Koichi Niihara, Japan  
Natalia Noginova, USA  
Sherine Obare, USA  
Won-Chun Oh, Republic of Korea  
Atsuto Okamoto, Japan  
Abdelwahab Omri, Canada  
Ungyu Paik, Republic of Korea  
Piersandro Pallavicini, Italy  
Edward A. Payzant, USA  
Alessandro Pegoretti, Italy  
Ton Peijs, UK  
Oscar Perales-Pérez, Puerto Rico  
Jorge Pérez-Juste, Spain  
Alexey P. Popov, Finland  
Philip D. Rack, USA  
Peter Reiss, France  
Orlando Rojas, USA  
Marco Rossi, Italy  
Ilker S. Bayer, Italy  
Cengiz S. Ozkan, USA



---

Sudipta Seal, USA  
Shu Seki, Japan  
Vladimir Šepelák, Germany  
Huaiyu Shao, Japan  
Prashant Sharma, USA  
Donglu Shi, USA  
Bhanu P. Singh, India  
Surinder Singh, USA  
Vladimir Sivakov, Germany  
Ashok Sood, USA  
Adolfo Speghini, Italy  
Marinella Striccoli, Italy  
Xuping Sun, KSA  
Ashok K. Sundramoorthy, USA

Angelo Taglietti, Italy  
Bo Tan, Canada  
Leander Tapfer, Italy  
Valeri P. Tolstoy, Russia  
Muhammet S. Toprak, Sweden  
Ramon Torrecillas, Spain  
Achim Trampert, Germany  
Takuya Tsuzuki, Australia  
Tamer Uyar, Turkey  
Bala Vaidhyanathan, UK  
Luca Valentini, Italy  
Rajender S. Varma, USA  
Ester Vazquez, Spain  
Antonio Villaverde, Spain

Ajayan Vinu, Australia  
Ruibing Wang, Macau  
Shiren Wang, USA  
Yong Wang, USA  
Magnus Willander, Sweden  
Ping Xiao, UK  
Zhi Li Xiao, USA  
Yangchuan Xing, USA  
Doron Yadlovker, Israel  
Yoke K. Yap, USA  
Kui Yu, Canada  
William Yu, USA  
Michele Zappalorto, Italy  
Renyun Zhang, Sweden

## Contents

**Polymer-Based Nano/Composites: Theory, Synthesis, Modifications, and Properties**, Mircea Chipara, Alan K. T. Lau, Mahmood Aliofkhaezai, Angel Romo-Urbe, and Ehsan Bafekrpour  
Volume 2015, Article ID 603907, 2 pages

**Preparation and Characterization of Paclitaxel Loaded SF/PLLA-PEG-PLLA Nanoparticles via Solution-Enhanced Dispersion by Supercritical CO<sub>2</sub>**, Zheng Zhao, Yi Li, and Yu Zhang  
Volume 2015, Article ID 913254, 7 pages

**Dynamic Mechanical Analysis and High Strain-Rate Energy Absorption Characteristics of Vertically Aligned Carbon Nanotube Reinforced Woven Fiber-Glass Composites**, Kiyun Kim, P. Raju Mantena, Seyed Soheil Daryadel, Veera M. Boddu, Matthew W. Brenner, and Jignesh S. Patel  
Volume 2015, Article ID 480549, 7 pages

**Oxygen Barrier Properties and Melt Crystallization Behavior of Poly(ethylene terephthalate)/Graphene Oxide Nanocomposites**, Anna Szymczyk, Sandra Paszkiewicz, Iwona Pawelec, Sławomir Lisiecki, Marek Jotko, Zdenko Špitalský, Jaroslav Mosnáček, and Zbigniew Roslaniec  
Volume 2015, Article ID 382610, 10 pages

**An Ensemble Learning for Predicting Breakdown Field Strength of Polyimide Nanocomposite Films**, Hai Guo, Jinghua Yin, Jingying Zhao, Lei Yao, Xu Xia, and Hao Luo  
Volume 2015, Article ID 950943, 11 pages

**Improved Electrical Conductivity of Carbon/Polyvinyl Alcohol Electrospun Nanofibers**, Nader Shehata, Nabil Madi, Mariam Al-Maadeed, Ibrahim Hassounah, and Abdullah Ashraf  
Volume 2015, Article ID 812481, 5 pages

**Development of a Composite Electrospun Polyethylene Terephthalate-Polyglycolic Acid Material: Potential Use as a Drug-Eluting Vascular Graft**, Christoph S. Nabzdyk, Maggie Chun, Saif G. Pathan, David W. Nelson, Jin-Oh You, Matthew D. Phaneuf, Frank W. LoGerfo, and Leena Pradhan-Nabzdyk  
Volume 2015, Article ID 340981, 7 pages

**Synthesis of Salt Responsive Spherical Polymer Brushes**, Na Su, Houbin Li, Yu Huang, and Xiongzhi Zhang  
Volume 2015, Article ID 956819, 7 pages

**Temperature Effect on Electrical Treeing and Partial Discharge Characteristics of Silicone Rubber-Based Nanocomposites**, Mohd Hafizi Ahmad, Nouruddeen Bashir, Zolkafle Buntat, Yanuar Z. Arief, Abdul Azim Abd Jamil, Mohamed Afendi Mohamed Piah, Abubakar A. Suleiman, Steve Dodd, and Nikola Chalashkanov  
Volume 2015, Article ID 962767, 13 pages

**Space Charge Property of Polyethylene/Silica Nanocomposites at Different Elongations**, Can Wang, Youyuan Wang, Peng Fan, and Ruijin Liao  
Volume 2015, Article ID 963960, 14 pages

## Editorial

# Polymer-Based Nano/Composites: Theory, Synthesis, Modifications, and Properties

Mircea Chipara,<sup>1</sup> Alan K. T. Lau,<sup>2</sup> Mahmood Aliofkhazraei,<sup>3</sup>  
Angel Romo-Uribe,<sup>4</sup> and Ehsan Bafekrpour<sup>5</sup>

<sup>1</sup>Department of Physics and Astronomy, The University of Texas Rio Grande Valley, 1201 W. University Drive, Edinburg, TX 78539, USA

<sup>2</sup>Department of Mechanical Engineering, The Hong Kong Polytechnic University, Hung Hom, Hong Kong

<sup>3</sup>Department of Materials Science, Faculty of Engineering, Tarbiat Modares University, Tehran, Iran

<sup>4</sup>Instituto de Ciencias Físicas, Universidad Nacional Autónoma de México (UNAM), Cuernavaca, MOR, Mexico

<sup>5</sup>Centre for Advanced Materials and Performance Textiles, RMIT University, Room 8, Building 512, 25 Dawson Street, Brunswick, VIC 3056, Australia

Correspondence should be addressed to Mircea Chipara; chipara@yahoo.com

Received 25 August 2015; Accepted 25 August 2015

Copyright © 2015 Mircea Chipara et al. This is an open access article distributed under the Creative Commons Attribution License, which permits unrestricted use, distribution, and reproduction in any medium, provided the original work is properly cited.

The need for better materials has driven us to composites, obtained by combining two or more materials with different physical and chemical properties. The first composite (wattle and daub) was discovered about 6,000 years ago and the first polymer-based composite (Bakelite) was patented in 1907. In polymer-based composites, one or more materials labelled as fillers are dispersed within a polymeric matrix (homopolymer, copolymer, block copolymer, or polymer blend). While it is possible to speculate in more detail about the terminology of polymer-based nanocomposites, the general perception is that a nanosized filler is required.

The nanorevolution opened the door to the fabrication of submicron confined particles. Typically, such particles known as “nanoparticles” have at least one dimension less than 100 nm. Two main techniques, namely, bottom-up and top-down, are competing for the fabrication of nanoparticles. In the bottom-up approach atoms and molecules are organized as nanoparticles while the top-down approach starts for micron or larger particles and reduces their dimensions. Typical bottom-up paths are represented by chemical synthesis, sputtering, electrodeposition, and chemical vapor deposition while among the top-down techniques it is possible to include the energetic mechanical milling and sonication.

The possibility to obtain particles confined at nanometer scale ignited an intense worldwide theoretical and experimental research aiming at synthesizing new nanoparticles

and at better understanding their properties. The reasons behind this effort derive from the amazing new or enhanced features of nanoparticles, triggered by the transition from the “classical” behavior to the “quantum behavior.” The submicron confinement of matter (of quantum nature) is responsible for important changes such as the shift of electronic energy levels towards higher energies as the size of the confinement is decreased, as observed in quantum wells, where the energy levels  $E$  for an electron in an infinite one-dimensional well of width  $L$  are  $E_n = \hbar^2 n^2 / (8mL^2)$ , where  $m$  is the mass of the electron and  $n$  the quantum number associated with the energy level. Another example is the dependence of the energy gap  $E_G$  of semiconducting nanoparticles on their radius  $E_G(R) = E_G(\infty) + \hbar^2 \pi^2 / (2R^2) (1/m_e + 1/m_h)$ , where  $E_G(\infty)$  is the gap energy for an infinite particle,  $m_e$  is the electron mass,  $m_h$  is the hole’s mass,  $\hbar$  is Planck’s constant,  $R$  is the radius of the nanoparticle, and  $E_G(R)$  is the gap energy of a particle of radius  $R$ .

Surface dominating effects may have important contributions to the physical properties of nanoparticles. However, some surface dominating effects have not a quantum nature being a consequence of the fact that the number of atoms located on the surface of nanoparticles is no more negligible compared to the number of atoms located within the core of the nanoparticles, as it was for micron scale or larger particles.

Polymer-based nanocomposites are materials obtained by dispersing such nanoparticles within various polymeric matrices such as homopolymers, copolymers, block copolymers, and polymer blends. This includes matrices with a wide variety of physical and chemical properties starting from structural capabilities to high elastic features, from hydrophobicity to hydrophilicity, and from electrical insulating features (polyethylene) to semiconductors or conductors (doped polyaniline, polyacetylenes). An amazing feature of these polymeric matrices is that they are porous, leaving the confined nanoparticle relatively exposed. This has been already speculated in various applications such as polymer deposited catalysts.

The overall physical and chemical properties of polymer-based nanocomposites are controlled by the properties of the nanoparticles, the features of the polymeric matrix, and the interactions between nanoparticles and the polymeric matrices. In polymer-based nanocomposites the huge surface area of the nanoparticles results in a large fraction of polymer being confined within the polymer-nanoparticles interface and eventually in a gradual transition of the physical and chemical properties from “bulk” matrix-controlled features to interphase or “surface” dominated characteristics. A good dispersion of the nanoparticles is mandatory to observe such transition. Typically, the enhanced thermal stability of polymer-based nanocomposites and the shifts of the main phase transitions occurring within the polymeric matrix as a result of the loading with nanoparticles are the main consequences of a thick polymer-nanoparticle interface.

All these competing factors resulted in a huge number of polymer-based nanocomposites with diverse applications, amazing physical and chemical features, and almost infinite possibilities. This issue focuses on various aspects of polymer-based nanocomposites, starting from synthesis and characterization up to applications. Owing to the structure of the polymeric matrix, many emerging applications are expected in the area of biology and medicine. The issue provides a relevant snapshot of the actual status of polymer-based nanocomposites starting from fabrication issues up to final (potential) applications.

*Mircea Chipara*  
*Alan K. T. Lau*  
*Mahmood Aliofkhazraei*  
*Angel Romo-Urbe*  
*Ehsan Bafekrpour*

## Research Article

# Preparation and Characterization of Paclitaxel Loaded SF/PLLA-PEG-PLLA Nanoparticles via Solution-Enhanced Dispersion by Supercritical CO<sub>2</sub>

Zheng Zhao,<sup>1,2,3</sup> Yi Li,<sup>2</sup> and Yu Zhang<sup>4</sup>

<sup>1</sup>State Key Laboratory of Advanced Technology for Materials Synthesis and Processing, Wuhan University of Technology, Wuhan 430070, China

<sup>2</sup>Institute of Textiles and Clothing, The Hong Kong Polytechnic University, Kowloon, Hong Kong

<sup>3</sup>Biomedical Materials and Engineering Research Center of Hubei Province, Wuhan University of Technology, Wuhan 430070, China

<sup>4</sup>Department of Mechanical Engineering, The Hong Kong Polytechnic University, Kowloon, Hong Kong

Correspondence should be addressed to Yi Li; [tliyi@polyu.edu.hk](mailto:tliyi@polyu.edu.hk)

Received 10 March 2015; Revised 31 May 2015; Accepted 17 June 2015

Academic Editor: Mircea Chipara

Copyright © 2015 Zheng Zhao et al. This is an open access article distributed under the Creative Commons Attribution License, which permits unrestricted use, distribution, and reproduction in any medium, provided the original work is properly cited.

Paclitaxel loaded silk fibroin/PLLA-PEG-PLLA (PTX-SF/PLLA-PEG-PLLA) nanoparticles with a mean particle size of about 651 nm were fabricated successfully by the SEDS process. Fourier transform infrared (FTIR) spectroscopy analysis indicated that the PTX was encapsulated by SF/PLLA-PEG-PLLA nanoparticles. X-ray powder diffraction (XRPD) analysis supported the results of FTIR analysis and also suggested that the crystalline state of PTX was decreased obviously. Furthermore, the UV-Vis/HPLC analysis showed that drug load (DL) and encapsulation efficiency (EE) were 18.1% and 90.2%, respectively. The *in vitro* drug release experiment suggested that the PTX-SF/PLLA-PEG-PLLA nanoparticles exhibited a sustained release and only 16.1% and 24.5% of paclitaxel were released at pH 7.4 and 6.0, respectively, in one week. The PTX-SF/PLLA-PEG-PLLA nanoparticles drug delivery system with pH-dependent release property has potential application in the field of tumor therapy.

## 1. Introduction

Paclitaxel (PTX), a mitotic inhibitor used in cancer chemotherapy, has exhibited its potency against many kinds of cancers, including advanced ovarian, lung, and breast cancers [1, 2]. The anticancer mechanism of PTX involves binding to microtubules, forming dysfunctional microtubules, and thus resulting in cell death [3]. However, its poor solubility in water drastically limits its clinical application in its natural form. To enhance drug solubility, paclitaxel is commercially formulated at 6 mg/mL in a vehicle composed of 1:1 blend of Cremophor EL and ethanol to make Taxol. Unfortunately, Cremophor EL is toxic and can cause severe side-effects, including hypersensitivity reactions, nephrotoxicity, and neurotoxicity [4, 5]. Also, the anticancer drug cannot be selectively accumulated into tumors tissues. The nonspecific distribution will reduce bioavailability and therapeutic efficiency of the anticancer drug because the drug spreads

randomly during systemic circulation and effects cells (healthy or tumor cells) indiscriminately [6].

In order to improve the therapeutic efficacy of PTX and reduce side-effects, many researchers have developed alternative drug delivery systems, including parenteral emulsions, liposomes, and nanoparticles [7–10]. Among them, polymer nanoparticle drug delivery systems have attracted much attention owing to high bioavailability and sustained drug release characteristics [11, 12]. Besides, it enables many different routes of drug administration, including injection, transdermal absorption, and oral application and inhalation. In particular, nanoparticles can extravasate into the tumor tissue via the leaky vessels surrounding tumors and then preferentially accumulate in solid tumors due to the enhanced permeation and retention (EPR) effect [13].

Suitable polymer should not only be biodegradable in response to biological condition but also exhibit excellent biocompatibility in human body. Biodegradable polymer can

be divided into natural and synthetic biodegradable polymer. Natural biodegradable polymer such as silk fibroin (SF) has been widely used in biomedical fields owing to its unique properties, including good biocompatibility, biodegradability, and low inflammatory response [14–16]. Recently, SF nanoparticles have been utilized to load anticancer drug PTX [17, 18]. However, natural polymer suffers from the high natural variability and the difficulties in processing.

Synthetic biodegradable polymers such as poly(L,L-lactide) and its copolymers with polyethylene glycol (PEG) with precise chemical composition can overcome the disadvantages of silk fibroin above and are more easily designed for specific application, such as controlled rates of dissolution, permeability, degradation, and erosion [19–22]. Therefore, it has been commonly used as drug carrier in biomedical fields. However, the main disadvantage of these synthetic polymers is undesirable biological responses to cells owing to high crystallinity, strong hydrophobicity, and lack of bioactive functions [23].

The combination of a synthetic polymer with natural polymer especially silk fibroin can overcome their disadvantages and is an effective strategy to fabricate novel nanoparticles as carrier for PTX with the desired physical and chemical properties, mechanical strength, and biological responses. Most importantly, silk fibroin has many bioactive groups, which can provide sites for conjugating with tumor-specific ligands to achieve tumor-targeted drug delivery.

In our previous study, natural silk fibroin (SF) has been used to modify synthetic poly(l-lactide)-poly(ethylene glycol)-poly(l-lactide) (PLLA-PEG-PLLA) to obtain SF/PLLA-PEG-PLLA composite nanoparticles prepared via solution-enhanced dispersion by supercritical CO<sub>2</sub> (SEDS) [23]. In the SEDS process, the supercritical CO<sub>2</sub> (scCO<sub>2</sub>) acts as antisolvent. In addition, the high velocity of the scCO<sub>2</sub> breaks up the polymer solution into very small droplets and enhances mass transfer between the scCO<sub>2</sub> and the droplets, instantaneously, resulting in phase separation and supersaturation of the polymer solution, thus leading to nucleation and precipitation of the polymer particle [24–26]. The incorporation of silk fibroin into the PLLA-PEG-PLLA nanoparticles improved biocompatibility and provided chemical modification. Moreover, the SF/PLLA-PEG-PLLA nanoparticles could be internalized by cells effectively [23]. Therefore, using the silk fibroin/PLLA-PEG-PLLA nanoparticles to load drugs and form a nanoparticle drug delivery system may be a potential application in the field of biomedical engineering.

In this study, the SEDS process was used to prepare a PTX loaded SF/PLLA-PEG-PLLA (PTX-SF/PLLA-PEG-PLLA) nanoparticles delivery system. The surface morphology, physical and chemical properties, drug load, encapsulation efficiency, and *in vitro* drug release properties of PTX-SF/PLLA-PEG-PLLA nanoparticles were measured.

## 2. Materials and Methods

**2.1. Materials.** Paclitaxel (PTX) was purchased from the Jiangsu Nanjing Zelang Medicine Technology Co., Ltd. (China). CO<sub>2</sub> with a purity of 99.9% was supplied by the Hong Kong Specialty Gases Co., Ltd. (Hong Kong). The solvent,

Dichloromethane (DCM), was purchased from the Advanced Technology & Industrial Co., Ltd. (Hong Kong). PLLA-PEG-PLLA triblock polymer (MW 100 kDa, PEG 10%) was purchased from Department of Medical Polymer Shandong Institute (Jinan, China). All other compounds were of analytical purity.

### 2.2. Methods

**2.2.1. Preparation of SF/PLLA-PEG-PLLA Nanoparticles and PTX Loaded SF/PLLA-PEG-PLLA Nanoparticles by the SEDS Process.** The SF/PLLA-PEG-PLLA composite nanoparticles can be prepared by the SEDS process given in [23]. For the preparation of PTX loaded SF/PLLA-PEG-PLLA (PTX-SF/PLLA-PEG-PLLA) composite nanoparticles, the method was described as follows. Briefly, PTX and PLLA-PEG-PLLA were dissolved in dichloromethane (DCM) solution together. Then water insoluble silk fibroin nanoparticles were dispersed into DCM solution to form suspension (for weight, PTX : silk fibroin nanoparticles : PLLA-PEG-PLLA = 5 : 4 : 16), and the final solution concentration of PTX-SF/PLLA-PEG-PLLA was 0.5% (w/v). Figure 1 shows a schematic diagram of the SEDS apparatus for preparation of the PTX-SF/PLLA-PEG-PLLA nanoparticles, which consists of three major components: a CO<sub>2</sub> supply system, a particle suspension delivery system and a high pressure vessel. In the particle suspension delivery system, an “injector” was made from a stainless steel cylinder and a piston with an O-ring seal. Using a SEDS process, when the desired pressure and temperature were stabilized, the suspension was injected through a stainless steel coaxial nozzle into the high-pressure vessel. The pressure, temperature, the flow rates of supercritical CO<sub>2</sub>, and the flow rates of suspension were kept at 10 MPa, 35°C; 25 NL·h<sup>-1</sup>, and 0.5 mL·min<sup>-1</sup>, respectively.

**2.2.2. Surface Morphology and Particle Size Distribution.** The surface morphology of samples was visualized by a field emission scanning electron microscopy (FE-SEM, JEOL, JSM-6490, Japan). Before analysis, samples were attached onto a carbon paint and then placed on an aluminum sample holder. The samples were made conductive by sputtering a thin layer of gold onto their surface. The particle size (PS) and particle size distribution (PSD) of PTX-SF/PLLA-PEG-PLLA nanoparticles dispersed in ethanol by sonication were measured by a laser diffraction particle size analyzer with a liquid module (LS 13320, Beckman Coulter, USA).

**2.2.3. FTIR Analysis.** The samples were combination with potassium bromide. Then the mixtures of the samples and potassium bromide were pressed into a transparent tablet. The FTIR spectra for the samples were recorded on an FTIR Perkin Elmer 1720 (Perkin Elmer, USA) in the transmission mode with the wave number ranging from 4,000 to 400 cm<sup>-1</sup>.

**2.2.4. XRPD Analysis.** Powder X-ray diffraction (XRPD) was performed by an X-ray diffractometer with a Cu K $\alpha$  ( $\lambda$  = 1.5405 Å) radiation (D8 Advance, Bruker AXS, Germany). The measurement was carried out in a  $2\theta$  range of 5~45° with

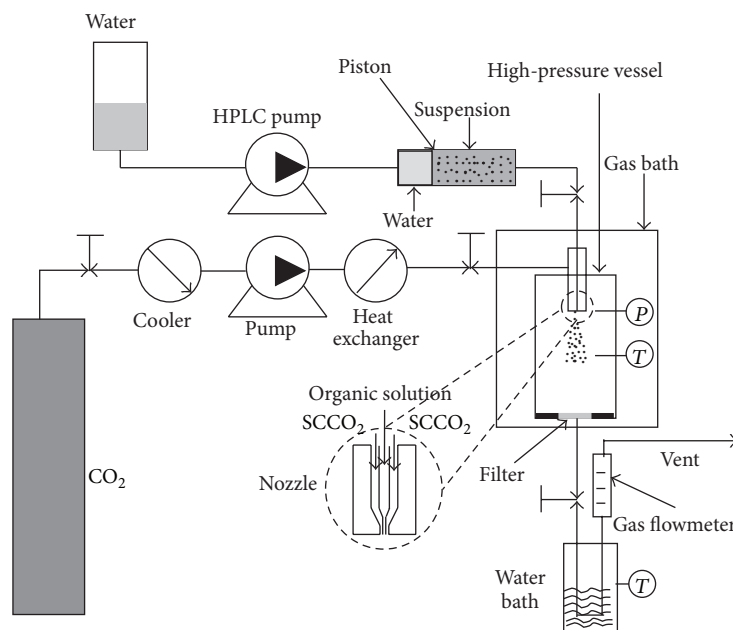


FIGURE 1: The schematic diagram of the SEDS apparatus for preparation of silk fibroin/PLLA-PE-PLLA composite nanoparticles.

0.02° step size and 10° min<sup>-1</sup> scan speed with a 2D detector at 40 kV and 40 mA.

**2.2.5. Drug Load (DL) and Encapsulation Efficiency (EE).** The contents of PTX were analyzed by UV-Vis/HPLC (Waters 1100) system with the following conditions: stationary phase: reverse-phase column (4.6 mm × Agilent Eclipse XDB-C18, 4.6 mm × 250 mm internal diameter, pore size 5 μm); mobile phase: mixture of acetonitrile and water (50 : 50 v/v); elution flow rate: 1 mL/min; detection wavelength: 227 nm. All the solvent and distilled water used for aqueous solutions and buffer should be filtered via a 0.22 μm membrane filter before use. The content of PTX in the samples was measured based on the peak area at the retention time. A calibration curve of standard PTX dissolving in mixture of acetonitrile and water (50 : 50 v/v) was utilized to calculate the content of PTX in the samples. All the samples were conducted in triplicate.

The actual content of paclitaxel (PTX) in PTX-SF/PLLA-PEG-PLLA nanoparticles can be determined by dissolving PTX-SF/PLLA-PEG-PLLA nanoparticles (3.0 mg accurately weighed) in 1 mL of DCM, and then 3 mL of an acetonitrile/water (50 : 50 v/v) mixture was added. After being completely mixed, the solution was filtered and then a nitrogen stream was introduced to volatilize DCM under stirring at room temperature until a clear solution was obtained. The clear solution was put into a vial for UV-Vis/HPLC assay according to calibration curve. The theoretical drug content, the actual drug load, and encapsulation efficiency were calculated by (1), (2), and (3), respectively. Each experiment was carried out in independent triplicate:

$$\text{Theoretical drug load} = \frac{W_1}{W_2} \times 100\%, \quad (1)$$

$$\text{Actual drug load} = \frac{W_3}{W_2} \times 100\%, \quad (2)$$

$$\text{Encapsulation efficiency} = \frac{W_3}{W_1} \times 100\%. \quad (3)$$

$W_1$  is the weight of theoretical PTX in the PTX-SF/PLLA-PEG-PLLA nanoparticles;  $W_2$  is the gross weight of the PTX-SF/PLLA-PEG-PLLA nanoparticles;  $W_3$  is the weight of the actual PTX encapsulated in the PTX-SF/PLLA-PEG-PLLA nanoparticles.

**2.2.6. In Vitro Drug Release.** Approximately 2 mg of PTX-SF/PLLA-PEG-PLLA nanoparticles was put into the pre-treated dialysis bag, and then the bag was placed into a bottle with 100 mL of PBS (pH 7.4) and incubated in a water-bath shaker at 37°C and 60 rpm. Ten milliliters of solution was periodically removed and replaced by fresh PBS (pH 7.4). The released drug was analyzed by UV-Vis/HPLC assay. As a control, an *in vitro* drug release experiment using free drug (of equivalent weight to that in the drug-loaded nanoparticles) was performed in similar conditions. The *in vitro* drug release curves were drawn based on the cumulative release percentage of PTX (% w/w) in PBS solution over long periods of time.

### 3. Results and Discussion

**3.1. Surface Morphology and Structure of PTX-SF/PLLA-PEG-PLLA Nanoparticles.** Figures 2(a) and 2(b) show the FE-SEM photographs of SF/PLLA-PEG-PLLA and PTX-SF/PLLA-PEG-PLLA nanoparticles obtained by the SEDS process, respectively. The particle size distribution of the PTX-SF/PLLA-PEG-PLLA nanoparticles is shown in Figure 3. According to our previous study, the SF/PLLA-PEG-PLLA

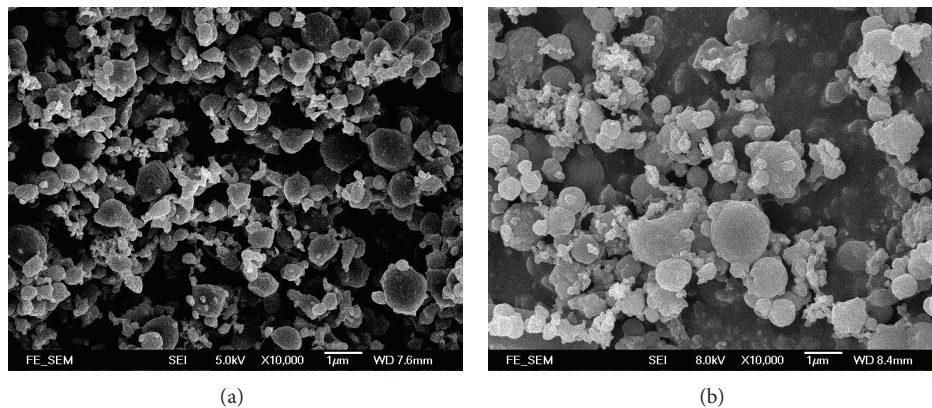


FIGURE 2: FE-SEM photographs of SF/PLLA-PEG-PLLA nanoparticles (a) and PTX-SF/PLLA-PEG-PLLA nanoparticles (b) obtained by the SEDS process.

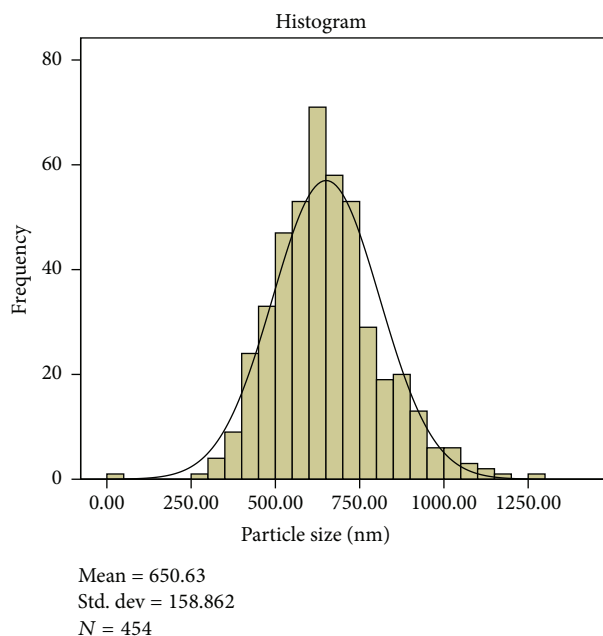


FIGURE 3: Particle size distribution of PTX-SF/PLLA-PEG-PLLA obtained by the SEDS process.

nanoparticles exhibit a composite structure with mean particle size of 634 nm and silk fibroin wrapped with PLLA-PEG-PLLA triblock polymer [23]. According to Figures 2(b) and 3, the PTX-SF/PLLA-PEG-PLLA nanoparticles possess a spherical shape with a mean particle size of about 651 nm and particle size distribution is 0.635. It suggested that the SEDS process is an effective method to prepare SF/PLLA-PEG-PLLA and PTX-SF/PLLA-PEG-PLLA nanoparticles.

**3.2. FTIR Analysis.** Figure 4 shows FTIR spectra of free PTX, physical mixtures of SF and PLLA-PEG-PLLA (SF+PLLA-PEG-PLLA), SF/PLLA-PEG-PLLA, and PTX-SF/PLLA-PEG-PLLA prepared by the SEDS process. The characteristic absorption peaks at  $1759\text{ cm}^{-1}$  are attributed to

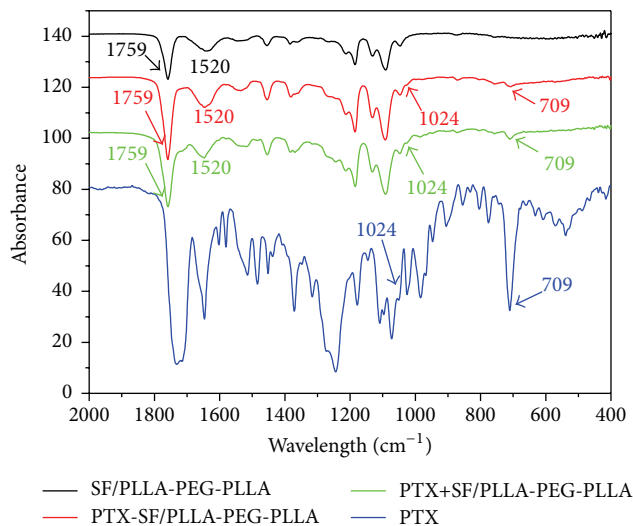


FIGURE 4: FTIR spectra of PTX, SF/PLLA-PEG-PLLA nanoparticles, physical mixture of PTX and SF/PLLA-PEG-PLLA nanoparticles, and PTX-SF/PLLA-PEG-PLLA nanoparticles.

the C=O stretching in PLLA-PEG-PLLA. The characteristic peak of amide II at  $1520\text{ cm}^{-1}$  is assigned to the  $\beta$ -sheet of silk fibroin. The major characteristic absorption peak of C-C stretching is shown for crystalline PTX at  $709\text{ cm}^{-1}$ . After the SEDS process, the main peaks ( $709\text{ cm}^{-1}$ ) appear at the same position compared with the physical mixtures, which suggests that the resulting products contain PTX. The presence of the peak at  $1024\text{ cm}^{-1}$  further demonstrates that PTX has been encapsulated by SF/PLLA-PEG-PLLA nanoparticles successfully.

**3.3. XRPD Analysis.** To investigate the physical state of the drug-loaded polymer nanoparticles prepared by the SEDS process, XRPD analysis was performed on the drug-loaded polymer nanoparticles. Figure 5 shows XRPD patterns of free PTX, physical mixtures of SF and PLLA-PEG-PLLA

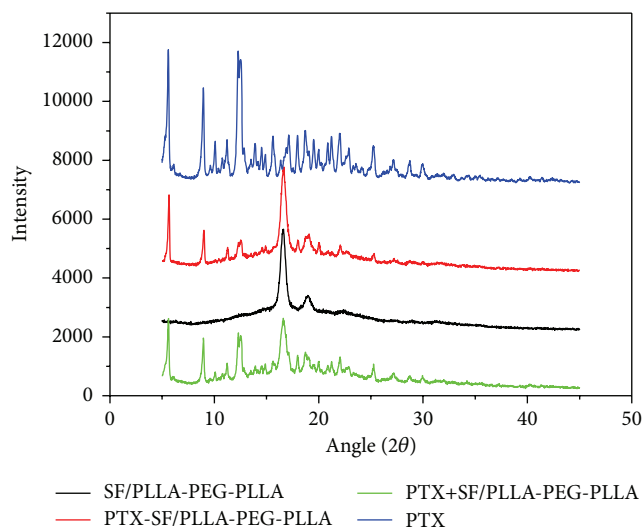


FIGURE 5: XRPD patterns of free PTX, SF/PLLA-PEG-PLLA, and PTX-SF/PLLA-PEG-PLLA prepared by the SEDS process.

(SF+PLLA-PEG-PLLA), SF/PLLA-PEG-PLLA, and PTX-SF/PLLA-PEG-PLLA prepared by the SEDS process. Original paclitaxel exhibited the main characteristic XRPD peaks at  $2\theta = 5.6^\circ, 9.1^\circ, 10.1^\circ, 12.7^\circ, 15.6^\circ,$  and  $25.3^\circ$ . After the SEDS process, nearly all the main characteristic peaks of crystalline PTX became weak, especially peaks at  $2\theta = 10.1^\circ$  and  $15.6^\circ$ . In the physical mixtures, the weak characteristic peaks of crystalline PTX at  $10.1^\circ$  can still be observed in the XRD patterns. This indicated that the SEDS process reduces the crystallinity of PTX obviously.

**3.4. Drug Load (DL) and Encapsulation Efficiency (EE).** DL and EE are two kinds of important parameters to determine the drug loading properties of nanoparticles. In the present study, the theoretical weight ratio of drug to polymer was selected as 1:4 (i.e., theoretical DL of 20%). The results of HPLC assay indicate the DL and EE are 18.1% and 90.2%, respectively. Many researchers have studied preparation of PTX loaded polymer nanoparticles by supercritical antisolvent process. Kang et al. prepared PTX-PLLA microparticles and found the theoretical DL and DL and EE of PTX-PLLA microparticles were 20%, 14.33%, and 62.68%, respectively [27]. Lee et al. also obtain PTX-PLLA particles. The results indicated that when the theoretical DL ranges from 3% to 10%, DD and EE are 1.98~7.87% and 59.3%~78.7%, respectively [28]. Li et al. studied the effect of process parameters on coprecipitation of PTX and PLLA by supercritical antisolvent process and found that DL was influenced by different process parameters such as solvent, the concentration of solute, and flow rate of solution [29]. Besides, Ouyang et al. fabricated the PTX-PLA-PEG-PLA microparticles by similar technique. When theoretical DL is 20%, DL ranges from 5.1% to 7.1% for different PEG contents, and EE ranges from 25.5% to 35.5% [30]. The different DL and EE may result from the different precipitation kinetics of the drug and polymer in the supercritical antisolvent process [27, 30]. Further studies are

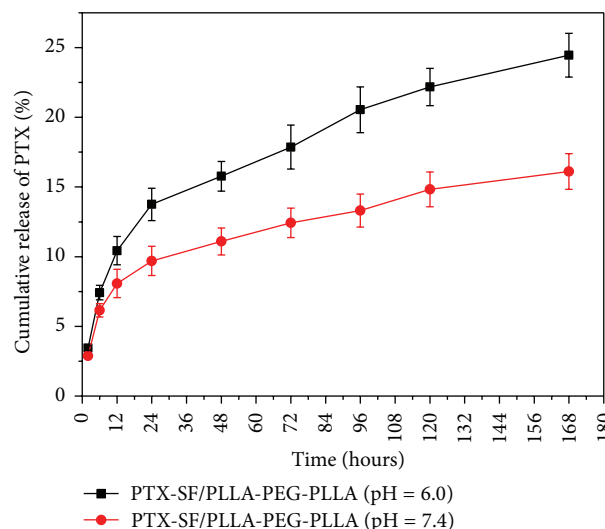


FIGURE 6: *In vitro* release profile of PTX from PTX-SF/PLLA-PEG-PLLA nanoparticles in PBS buffer (pH 6.0 and 7.4).

demanded to explore the actual reason. As nearly all the drug is loaded on the SF/PLLA-PEG-PLLA nanoparticles, it would be commercially attractive.

**3.5. *In Vitro* Drug Release.** In terms of the unique microenvironment surrounding tumor cells, in which the average extracellular pH value in tumors is between 6.0 and 7.0, however, the extracellular pH value in normal tissues is about 7.4.

The *in vitro* release profile of PTX from nanoparticles was studied in different pH conditions (pH 6.0 and 7.4). Figure 6 shows the *in vitro* release profile of PTX from PTX loaded SF/PLLA-PEG-PLLA (PTX-SF/PLLA-PEG-PLLA) nanoparticles in PBS buffer (pH 6.0 and 7.4). As shown in Figure 5, the drug release in PBS buffer (pH 7.4) was slower than that in PBS buffer (pH 6.0). And 16.1% and 24.5% of paclitaxel were released at pH 7.4 and 6.0, respectively, in one week. Therefore, there was no burst effect and PTX can be released in a controlled way from SF/PLLA-PEG-PLLA nanoparticles. Furthermore, nanoencapsulation of PTX by SF/PLLA-PEG-PLLA nanoparticles could improve the solubility of PTX.

The faster release of PTX from the PTX-SF/PLLA-PEG-PLLA nanoparticles at lower pH conditions results from two possible reasons. One is that lower pH may cause faster degradation of SF/PLLA-PEG-PLLA polymer. The other is that the amino group of the drug could be protonated at lower pH condition. This pH-dependent release property may be beneficial for tumor treatment [31, 32]. It is likely that the release of PTX from SF/PLLA-PEG-PLLA nanoparticles within healthy physiological pH levels (pH 7.4) is slow, sustained, and relatively suppressed during systemic circulation. When SF/PLLA-PEG-PLLA nanoparticles were delivered into the location of solid tumor, an enhanced release of PTX from nanoparticles could be triggered by the mildly acidic tumor microenvironment (pH 6.0) to ensure that the intracellular drug concentration reaches the therapeutic dose.

Therefore, pH-dependent release property may decrease the side-effect of PTX to healthy cells owing to relatively low PTX concentration and enhance the therapeutic efficiency against tumor cells.

#### 4. Conclusions

PTX-SF/PLLA-PEG-PLLA nanoparticles with mean particle size of 651 nm were prepared by the SEDS process successfully. FTIR and XRPD analysis indicated PTX was encapsulated by SF/PLLA-PEG-PLLA nanoparticles. Furthermore, the PTX became more amorphous after the SEDS process. The PTX-SF/PLLA-PEG-PLLA nanoparticles exhibited a controlled drug release. In particular the drug release rate in PBS solution could be accelerated with decrease of pH value from 7.4 to 6.0. This pH-dependent release property may decrease the side-effect of PTX to healthy cells and enhance the therapeutic efficiency against tumor cells due to the acidic tumor microenvironment. In terms of these characteristics, PTX-SF/PLLA-PEG-PLLA nanoparticles have potential application in the field of tumor therapy.

#### Conflict of Interests

The authors declare that there is no conflict of interests regarding the publication of this paper.

#### Acknowledgments

The authors would like to thank the Hong Kong Research Grant Council and the Hong Kong Polytechnic University through Projects PolyU5242/09E and G-YM63. Also, the authors would like to thank the support of Natural Science Foundation of Hubei Province through Project 2014CFB839, Doctoral Research Fund of Wuhan University of Technology through Project 471-40120093, Opening Project KJS1415 of National Engineering Laboratory for Modern Silk, and Guangdong Provincial Department of Science and Technology through Projects 2012B050800002 and 2012B091000143.

#### References

- [1] H.-Y. Cho, C. K. Lee, and Y.-B. Lee, "Preparation and evaluation of PEGylated and folate-PEGylated liposomes containing paclitaxel for lymphatic delivery," *Journal of Nanomaterials*, vol. 2015, Article ID 471283, 10 pages, 2015.
- [2] F. Danhier, P. Danhier, C. J. De Saeleleer et al., "Paclitaxel-loaded micelles enhance transvascular permeability and retention of nanomedicines in tumors," *International Journal of Pharmaceutics*, vol. 479, no. 2, pp. 399–407, 2015.
- [3] G. Ruan and S.-S. Feng, "Preparation and characterization of poly(lactic acid)-poly(ethylene glycol)-poly(lactic acid) (PLA-PEG-PLA) microspheres for controlled release of paclitaxel," *Biomaterials*, vol. 24, no. 27, pp. 5037–5044, 2003.
- [4] F. Danhier, N. Lecouturier, B. Vroman et al., "Paclitaxel-loaded PEGylated PLGA-based nanoparticles: *in vitro* and *in vivo* evaluation," *Journal of Controlled Release*, vol. 133, no. 1, pp. 11–17, 2009.
- [5] P.-P. Lv, W. Wei, H. Yue, T.-Y. Yang, L.-Y. Wang, and G.-H. Ma, "Porous quaternized chitosan nanoparticles containing paclitaxel nanocrystals improved therapeutic efficacy in non-small-cell lung cancer after oral administration," *Biomacromolecules*, vol. 12, no. 12, pp. 4230–4239, 2011.
- [6] A. K. Singla, A. Garg, and D. Aggarwal, "Paclitaxel and its formulations," *International Journal of Pharmaceutics*, vol. 235, no. 1-2, pp. 179–192, 2002.
- [7] T. Yang, M.-K. Choi, F.-D. Cui et al., "Preparation and evaluation of paclitaxel-loaded PEGylated immunoliposome," *Journal of Controlled Release*, vol. 120, no. 3, pp. 169–177, 2007.
- [8] R. T. Liggins and H. M. Burt, "Paclitaxel-loaded poly (L-lactic acid) microspheres 3: blending low and high molecular weight polymers to control morphology and drug release," *International Journal of Pharmaceutics*, vol. 282, no. 1-2, pp. 61–71, 2004.
- [9] Z. Zhang and S.-S. Feng, "The drug encapsulation efficiency, *in vitro* drug release, cellular uptake and cytotoxicity of paclitaxel-loaded poly(lactide)-tocopheryl polyethylene glycol succinate nanoparticles," *Biomaterials*, vol. 27, no. 21, pp. 4025–4033, 2006.
- [10] K. M. Huh, H. S. Min, S. C. Lee, H. J. Lee, S. Kim, and K. Park, "A new hydrotropic block copolymer micelle system for aqueous solubilization of paclitaxel," *Journal of Controlled Release*, vol. 126, no. 2, pp. 122–129, 2008.
- [11] Y. B. Patil, U. S. Toti, A. Khair, L. Ma, and J. Panyam, "Single-step surface functionalization of polymeric nanoparticles for targeted drug delivery," *Biomaterials*, vol. 30, no. 5, pp. 859–866, 2009.
- [12] Z. Keresztesy, M. Bodnár, E. Ber et al., "Self-assembling chitosan/poly- $\gamma$ -glutamic acid nanoparticles for targeted drug delivery," *Colloid and Polymer Science*, vol. 287, no. 7, pp. 759–765, 2009.
- [13] L. Brannon-Peppas and J. O. Blanchette, "Nanoparticle and targeted systems for cancer therapy," *Advanced Drug Delivery Reviews*, vol. 56, no. 11, pp. 1649–1659, 2004.
- [14] Y. Lian, J.-C. Zhan, K.-H. Zhang, and X.-M. Mo, "Fabrication and characterization of curcumin-loaded silk fibroin/P(LLA-CL) nanofibrous scaffold," *Frontiers of Materials Science*, vol. 8, no. 4, pp. 354–362, 2014.
- [15] B.-J. Dong and Q. Lu, "Conductive Au nanowires regulated by silk fibroin nanofibers," *Frontiers of Materials Science*, vol. 8, no. 1, pp. 102–105, 2014.
- [16] Z. Zhao, Y. Li, and M. Xie, "Silk fibroin-based nanoparticles for drug delivery," *International Journal of Molecular Sciences*, vol. 16, no. 3, pp. 4880–4903, 2015.
- [17] M. Chen, Z. Shao, and X. Chen, "Paclitaxel-loaded silk fibroin nanospheres," *Journal of Biomedical Materials Research, Part A*, vol. 100, no. 1, pp. 203–210, 2012.
- [18] P. Wu, Q. Liu, R. Li et al., "Facile preparation of paclitaxel loaded silk fibroin nanoparticles for enhanced antitumor efficacy by locoregional drug delivery," *ACS Applied Materials and Interfaces*, vol. 5, no. 23, pp. 12638–12645, 2013.
- [19] T. Deepak, D. Michel, and P. Yashwant, *Nanoparticulate Drug Delivery Systems*, Informa Healthcare USA, New York, NY, USA, 2007.
- [20] B. Dhurai, N. Saraswathy, R. Maheswaran et al., "Electrospinning of curcumin loaded chitosan/poly (lactic acid) nanofilm and evaluation of its medicinal characteristics," *Frontiers of Materials Science*, vol. 7, no. 4, pp. 350–361, 2013.

- [21] C. G. Mothé, A. D. Azevedo, W. S. Drumond, S. H. Wang, and R. D. Sinisterra, "Preparation and characterization of poly(L-lactide)-b-poly(ethylene glycol)-b-poly(L-lactide) (PLLA-PEG-PLLA) microspheres having encapsulated tetracycline," *Journal of Thermal Analysis and Calorimetry*, vol. 106, no. 3, pp. 671–677, 2011.
- [22] A.-Z. Chen, L. Li, S.-B. Wang et al., "Study of Fe<sub>3</sub>O<sub>4</sub>-PLLA-PEG-PLLA magnetic microspheres based on supercritical CO<sub>2</sub>: preparation, physicochemical characterization, and drug loading investigation," *The Journal of Supercritical Fluids*, vol. 67, pp. 139–148, 2012.
- [23] Z. Zhao, Y. Li, Y. Zhang et al., "Development of silk fibroin modified poly(L-lactide)-poly(ethylene glycol)-poly(L-lactide) nanoparticles in supercritical CO<sub>2</sub>," *Powder Technology*, vol. 268, no. 1, pp. 118–125, 2014.
- [24] A.-Z. Chen, L. Li, S.-B. Wang et al., "Nanonization of methotrexate by solution-enhanced dispersion by supercritical CO<sub>2</sub>," *Journal of Supercritical Fluids*, vol. 67, pp. 7–13, 2012.
- [25] Z. Zhao, A. Z. Chen, Y. Li et al., "Fabrication of silk fibroin nanoparticles for controlled drug delivery," *Journal of Nanoparticle Research*, vol. 14, no. 4, article 736, 2012.
- [26] Z. Zhao, Y. Li, A.-Z. Chen et al., "Generation of silk fibroin nanoparticles via solution-enhanced dispersion by supercritical CO<sub>2</sub>," *Industrial & Engineering Chemistry Research*, vol. 52, no. 10, pp. 3752–3761, 2013.
- [27] Y. Kang, J. Wu, G. Yin et al., "Characterization and biological evaluation of paclitaxel-loaded poly(L-lactic acid) microparticles prepared by supercritical CO<sub>2</sub>," *Langmuir*, vol. 24, no. 14, pp. 7432–7441, 2008.
- [28] L. Y. Lee, C. H. Wang, and K. A. Smith, "Supercritical antisolvent production of biodegradable micro- and nanoparticles for controlled delivery of paclitaxel," *Journal of Controlled Release*, vol. 125, no. 2, pp. 96–106, 2008.
- [29] W. Li, G. Liu, L. Li, J. Wu, Y. Lü, and Y. Jiang, "Effect of process parameters on co-precipitation of paclitaxel and poly(L-lactic acid) by supercritical antisolvent process," *Chinese Journal of Chemical Engineering*, vol. 20, no. 4, pp. 803–813, 2012.
- [30] P. Ouyang, Y.-Q. Kang, G.-F. Yin, Z.-B. Huang, Y.-D. Yao, and X.-M. Liao, "Fabrication of hydrophilic paclitaxel-loaded PLA-PEG-PLA microparticles via SEDS process," *Frontiers of Materials Science in China*, vol. 3, no. 1, pp. 15–24, 2009.
- [31] J. Liu, Y. Huang, A. Kumar et al., "PH-sensitive nano-systems for drug delivery in cancer therapy," *Biotechnology Advances*, vol. 32, no. 4, pp. 693–710, 2014.
- [32] S. J. T. Rezaei, H. S. Abandansari, M. R. Nabid, and H. Niknejad, "PH-responsive unimolecular micelles self-assembled from amphiphilic hyperbranched block copolymer for efficient intracellular release of poorly water-soluble anticancer drugs," *Journal of Colloid and Interface Science*, vol. 425, pp. 27–35, 2014.

## Research Article

# Dynamic Mechanical Analysis and High Strain-Rate Energy Absorption Characteristics of Vertically Aligned Carbon Nanotube Reinforced Woven Fiber-Glass Composites

**Kiyun Kim,<sup>1</sup> P. Raju Mantena,<sup>1</sup> Seyed Soheil Daryadel,<sup>1</sup> Veera M. Boddu,<sup>2</sup> Matthew W. Brenner,<sup>2</sup> and Jignesh S. Patel<sup>2</sup>**

<sup>1</sup>*Composite Structures and Nano-Engineering Research, Department of Mechanical Engineering, University of Mississippi, University, MS 38677, USA*

<sup>2</sup>*U.S. Army Engineer Research and Development Center-Construction Engineering Research Laboratory (ERDC-CERL), Champaign, IL 61821, USA*

Correspondence should be addressed to Kiyun Kim; [kky2729@gmail.com](mailto:kky2729@gmail.com)

Received 19 May 2015; Revised 16 July 2015; Accepted 21 July 2015

Academic Editor: Mircea Chipara

Copyright © 2015 Kiyun Kim et al. This is an open access article distributed under the Creative Commons Attribution License, which permits unrestricted use, distribution, and reproduction in any medium, provided the original work is properly cited.

The dynamic mechanical behavior and energy absorption characteristics of nano-enhanced functionally graded composites, consisting of 3 layers of vertically aligned carbon nanotube (VACNT) forests grown on woven fiber-glass (FG) layer and embedded within 10 layers of woven FG, with polyester (PE) and polyurethane (PU) resin systems (FG/PE/VACNT and FG/PU/VACNT) are investigated and compared with the baseline materials, FG/PE and FG/PU (i.e., without VACNT). A Dynamic Mechanical Analyzer (DMA) was used for obtaining the mechanical properties. It was found that FG/PE/VACNT exhibited a significantly lower flexural stiffness at ambient temperature along with higher damping loss factor over the investigated temperature range compared to the baseline material FG/PE. For FG/PU/VACNT, a significant increase in flexural stiffness at ambient temperature along with a lower damping loss factor was observed with respect to the baseline material FG/PU. A Split Hopkinson Pressure Bar (SHPB) was used to evaluate the energy absorption and strength of specimens under high strain-rate compression loading. It was found that the specific energy absorption increased with VACNT layers embedded in both FG/PE and FG/PU. The compressive strength also increased with the addition of VACNT forest layers in FG/PU; however, it did not show an improvement for FG/PE.

## 1. Introduction

Development of novel, light-weight, high-strength, and high-temperature resistant materials has been the focus of increased research for many applications [1] such as aerospace and automobile structures, where the material experiences severe thermal gradients and requires high flexural rigidity and high vibration damping. Due to the increasing demand of required conflicting properties, the newly developed functionally graded materials (FGM) have been a broad research area on account of their tailored properties [2, 3]. Investigation of carbon nanotubes' (CNT) role in CNT-polymer composites and their dynamic behavior can also help to develop such FGM [4]. CNT can enhance the mechanical

properties of FGM, due to their unique material properties, such as high stiffness, strength, and toughness [5, 6]. These nano-enhanced FGM are being considered for blast/ballistic protective structures and other armor applications.

Zeng et al. [7] studied the mechanical properties of VACNT based sandwich composites using DMA. It was observed that VACNT based sandwich composites showed higher flexural rigidity and damping compared to samples consisting of carbon fiber fabric stacks without VACNT. In previous research [8] conducted at the Blast and Impact Dynamics laboratory, University of Mississippi, the dynamic mechanical behavior and high strain-rate response of a FGM system consisting of VACNT grown on a silicon (Si) wafer substrate have been investigated. It was found that

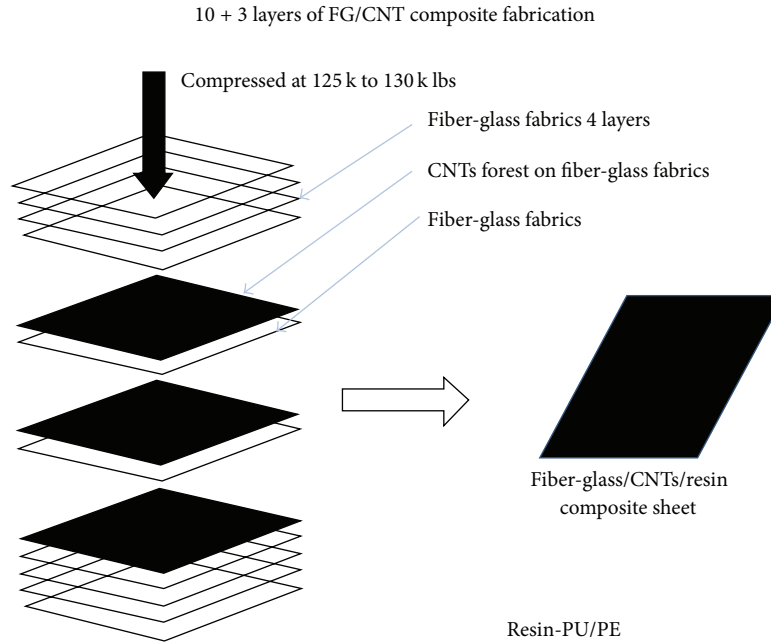


FIGURE 1: Schematic of the FG/PE/VACNT and FG/PU/VACNT samples with 10 layers of woven fiber-glass + 3 layers of embedded VACNT [9].

VACNT forests grown on Si wafer substrate exhibited significantly higher flexural stiffness, damping, and specific energy absorption.

In the current study, dynamic mechanical behavior and energy absorption characteristics of a VACNT-enhanced FGM system are investigated. VACNT forests were grown on the woven FG fabric layers with two different thermoset resin systems, PE and PU, and embedded within the specimens. Two different experimental techniques, DMA and SHPB, were used for evaluating their dynamic properties.

## 2. Materials and Methods

**2.1. Specimen Preparation.** 10-layer woven FG fabrics with PE resin (E15-8082) and 10-layer woven FG fabrics with PU resin (3475 Urethane Casting) were prepared as baseline composites (FG/PE and FG/PU) by the autoclave process.

Carbon nanotubes were grown on 12'' by 12'' sheet of desized glass fabric. Three sheets of the fabric were arranged on each of three racks in a steel chamber ( $\sim 18'' \times 18'' \times 9''$ ) which was heated to about 650°C. A solution of 4% by wt. ferrocene in m-xylene was prepared to implement the floating catalyst fabrication of CNTs and fed through three inlet manifolds, each of which was externally heated to about 350°C to vaporize the solution. Nitrogen and hydrogen, at a flow rate of 2000 and 300 cubic cm/min, respectively, carried the vapor into the reaction chamber containing the glass fabrics. The fabrics were processed for 60 min. The temperature in the reaction chamber, however, fluctuated ( $\pm 50^\circ\text{C}$ ) significantly around 600°C during the CNT growth process. A total ferrocene/catalyst solution of about 300–400 mL was used. FG/PE/VACNT and FG/PU/VACNT specimens having

3 layers of VACNT grown/embedded within 10 layers of woven FG along with two different resin systems (PE and PU) were fabricated, by hand lay-up and compression. A schematic of FG/PE/VACNT and FG/PU/VACNT is shown in Figure 1. The composites were then cut into individual samples, as required for DMA (60 mm long  $\times$  10 mm wide  $\times$  6 mm thick rectangular beams) and SHPB (6 mm  $\times$  6 mm  $\times$  6 mm square specimens) tests. More details of the specimen preparation and fabrication are given in [9].

**2.2. DMA Technique.** Dynamic mechanical behavior of FG/PE, FG/PU, FG/PE/VACNT, and FG/PU/VACNT specimens was investigated using a TA Instruments Model Q800 DMA [10]. Rectangular beam specimens, with 60 mm in length, 10 mm in width, and 6 mm in thickness, provided by ERDC-CERL (U.S. Army Engineer Research and Development Center-Construction Engineering Research Laboratory (ERDC-CERL), Champaign, IL 61821, USA) were used for this study. Mechanical properties such as storage modulus (flexural stiffness), loss modulus (energy dissipation),  $\tan \delta$  (inherent damping), and glass transition temperature ( $T_g$ ) were obtained in the three-point oscillatory bending mode. Roller pins on each side (with a span of 50 mm) were used to support the specimens and force applied in the middle of the span. All the specimens were subjected to 1 Hz single frequency with 10  $\mu\text{m}$  midspan displacement amplitude. For these experiments, only the heating temperature ramp (from ambient 30°C to 200°C) was implemented, with the temperature elevated in 2°C/min steps up to the final temperature. Poisson's ratio of 0.3 is input as a constant parameter for all samples.

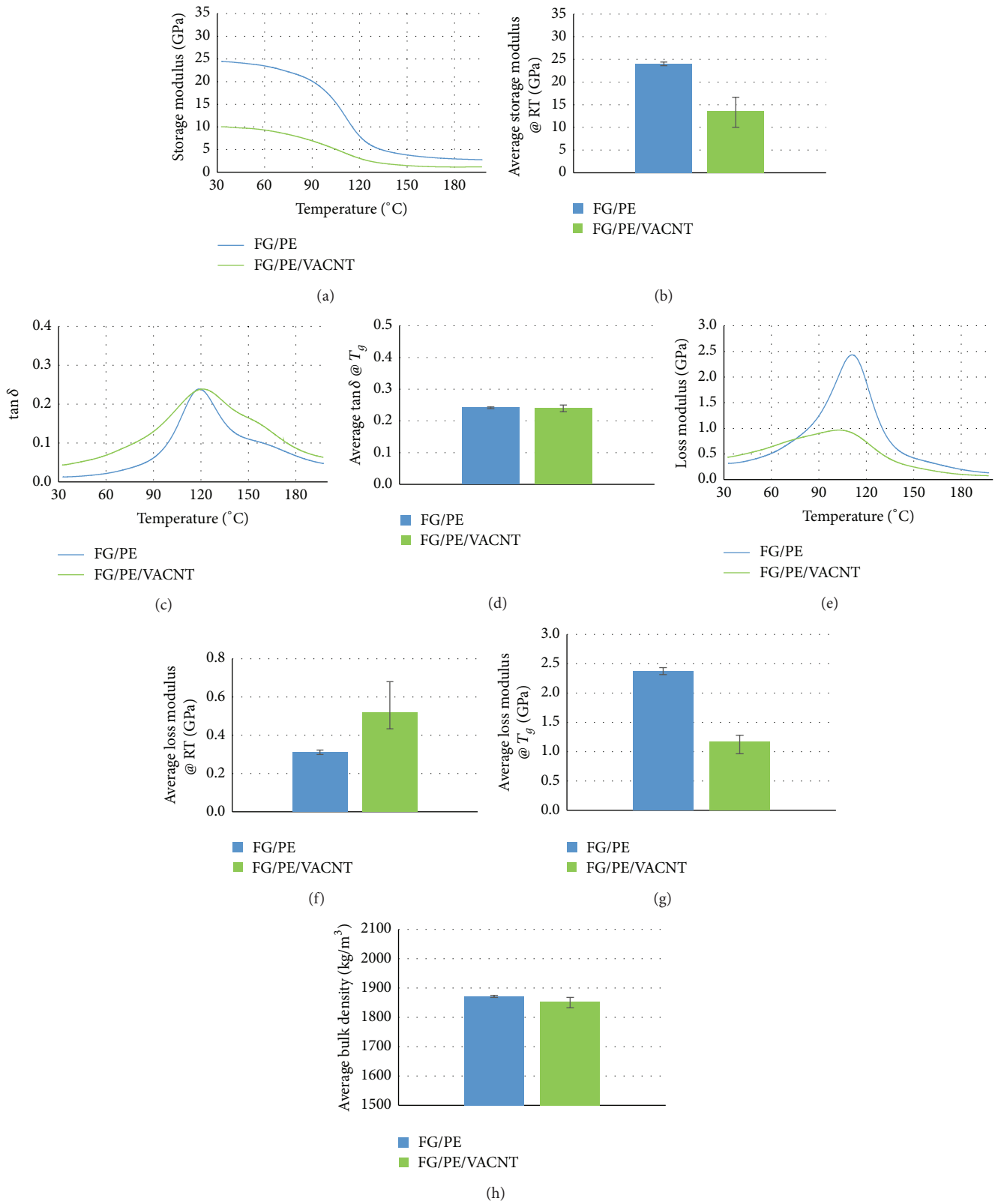


FIGURE 2: DMA response of 10-layer woven fiber-glass with PE resin (FG/PE) and 10-layer woven fiber-glass with PE resin along with embedded 3 layers of VACNT (FG/PE/VACNT): (a) storage modulus, (b) storage modulus at RT, (c) damping loss factor, (d) damping loss factor at  $T_g$ , (e) loss modulus, (f) loss modulus at RT, (g) loss modulus at  $T_g$ , and (h) average bulk density of specimens (three each).

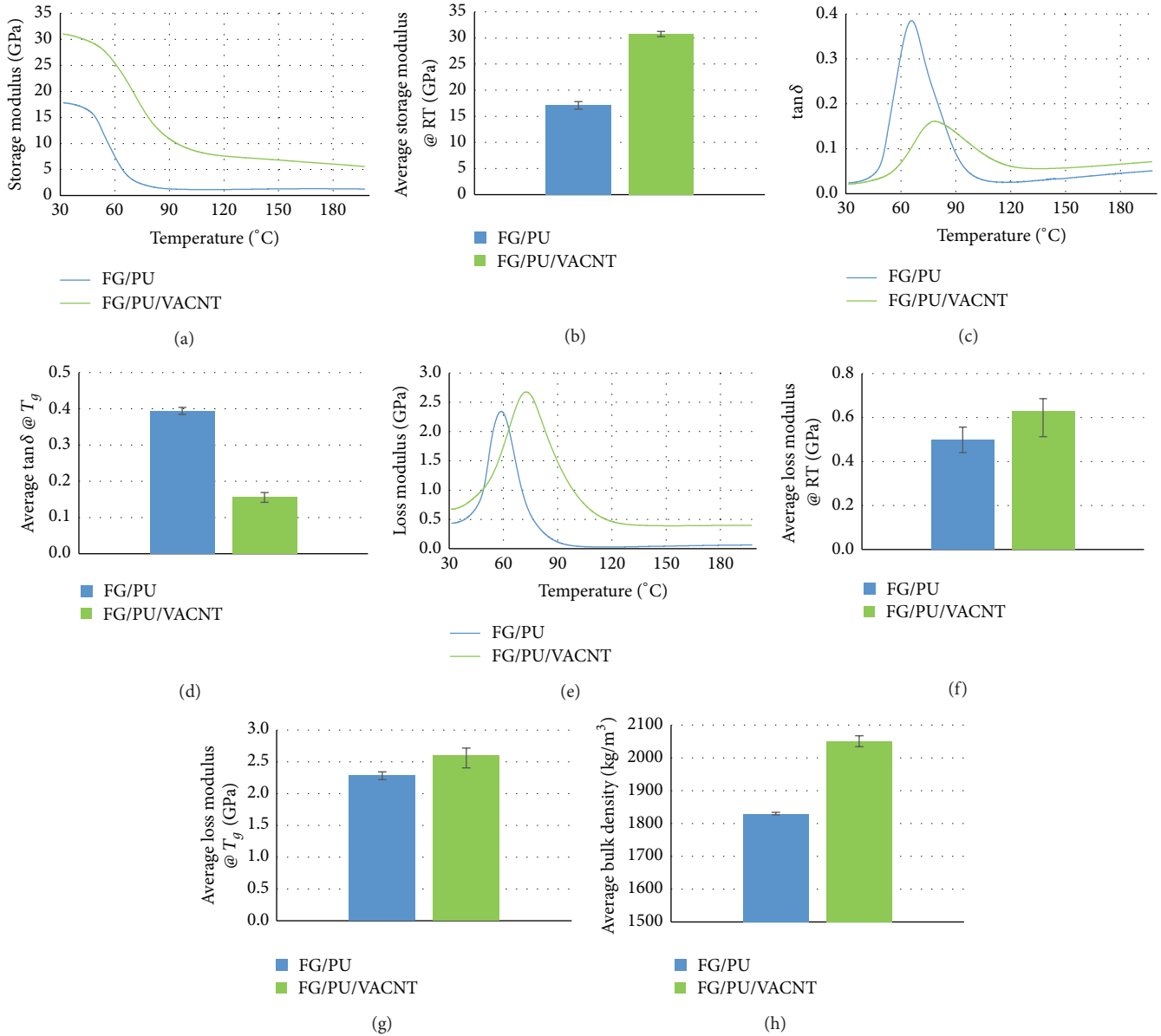


FIGURE 3: DMA response of 10-layer woven fiber-glass with PU resin (FG/PU) and 10-layer woven fiber-glass with PU resin along with embedded 3 layers of VACNT (FG/PU/VACNT): (a) storage modulus, (b) storage modulus at RT, (c) damping loss factor, (d) damping loss factor at  $T_g$ , (e) loss modulus, (f) loss modulus at RT, (g) loss modulus at  $T_g$ , and (h) average bulk density of specimens (three each).

**2.3. SHPB Technique.** The high strain-rate compressive tests were conducted on FG/PE, FG/PU, FG/PE/VACNT, and FG/PU/VACNT specimens using a modified SHPB in the Blast and Impact Dynamics Lab at the University of Mississippi, MS. Aluminum bars of 19.02 mm diameter were used as striker, incident, and transmission bars. Square specimens were cut precisely (6 mm × 6 mm × 6 mm) and tested with compression SHPB apparatus to evaluate the dynamic mechanical properties such as compressive strength, specific energy absorption, and rate of specific energy. Polyurea pulse shaper was used to minimize the wave dispersion and achieve the required stress equilibrium [11]. Glycerin was also used for

holding specimens in-between incident and transmission bar ends to minimize the interfacial friction.

### 3. Results and Discussion

**3.1. DMA Results.** The DMA experiments were conducted on FG/PE, FG/PU, FG/PE/VACNT, and FG/PU/VACNT samples (three samples each) to compare and investigate effects of the embedded VACNT layers on specimens' dynamic mechanical behavior. The output data graphs, the storage modulus (flexural stiffness), the loss modulus (energy dissipation), and the damping loss factor ( $\tan \delta$ , ratio of dissipated

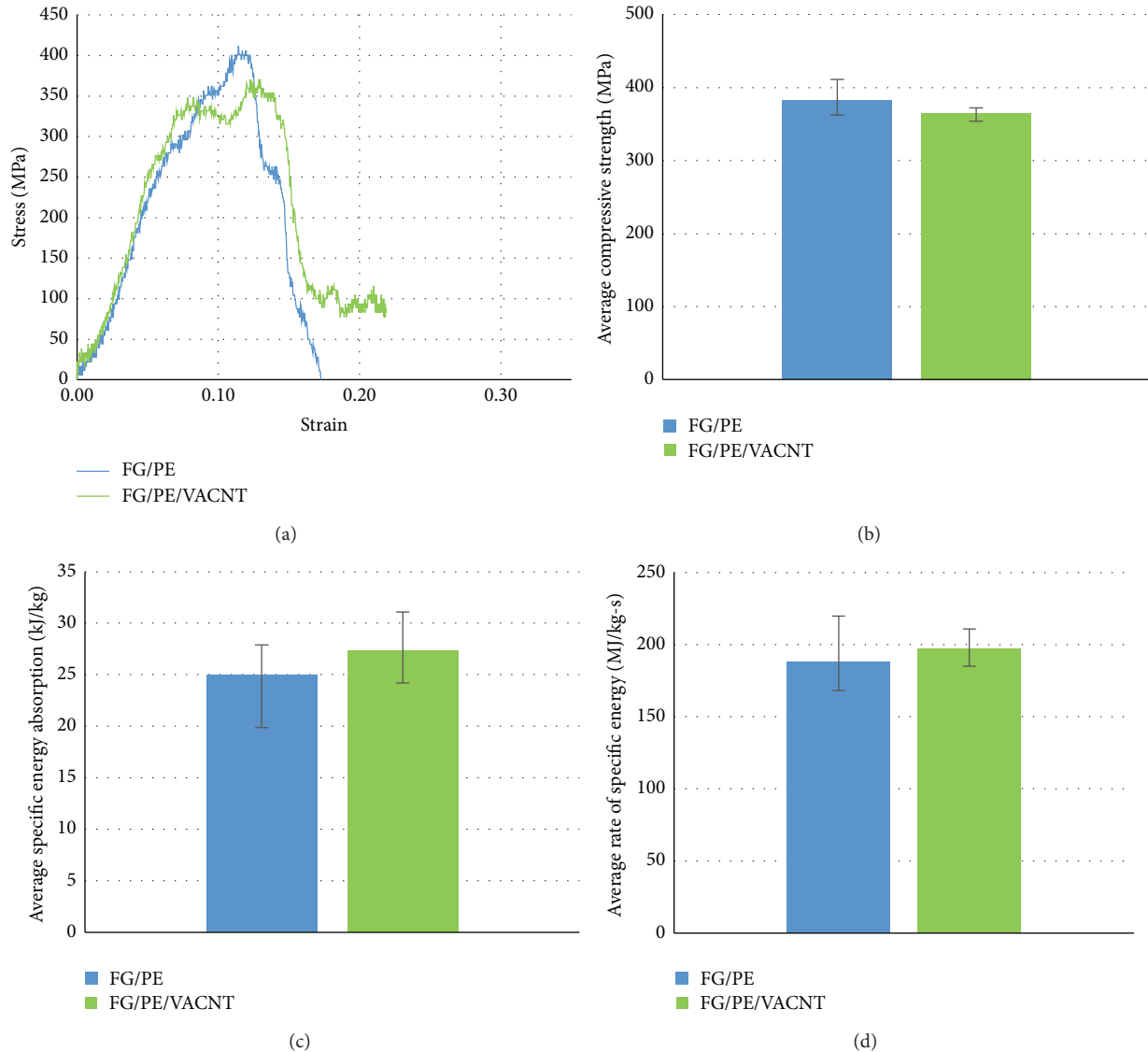


FIGURE 4: SHPB compression test response of FG/PE and FG/PE/VACNT composites evaluated over strain rate of 700 to 800/s: (a) stress-strain curve of FG/PE and FG/PE/VACNT, (b) compressive strength, (c) average specific energy absorption, and (d) rate of specific energy absorption.

energy to stored energy) for FG/PE and FG/PE/VACNT specimens are presented in Figure 2. As can be seen, at room temperature (RT) FG/PE/VACNT samples exhibited 40% drop in storage modulus compared to the baseline FG/PE samples. The  $\tan \delta$  of FG/PE/VACNT specimens over the test temperature range from 32°C to 200°C (or frequency, by the time-temperature correspondence principle for viscoelastic materials) appeared to be consistently higher (by about 60%), but it was found to be similar as baseline FG/PE at  $T_g$  (120°C). The loss modulus of FG/PE/VACNT was higher at RT compared to the baseline FG/PE, but it was much lower at  $T_g$  (120°C). The average bulk density of FG/PE/VACNT was slightly lower than the FG/PE specimens. Glass transition temperature was almost the same for both composites (120°C).

In Figure 3, the dynamic mechanical behavior of FG/PU/VACNT and FG/PU specimens is compared. It was found

that the storage modulus of FG/PU/VACNT increased (from about 18 GPa to 31 GPa at RT) in comparison with the baseline FG/PU samples. Additionally, FG/PU/VACNT exhibited higher loss modulus at both RT and  $T_g$ . The average bulk density and  $T_g$  also increased. However, a significant drop in inherent damping ( $\tan \delta$ ) was observed at  $T_g$  with the addition of VACNT layers (FG/PU/VACNT).

In contrast to previous investigation of VACNT grown on silicon wafer substrate [8], the addition of VACNT layers did not show an increase in damping loss factor ( $\tan \delta$ ) in FG/PE/VACNT and FG/PU/VACNT samples. However, a significant drop in damping has been observed in FG/PU/VACNT samples. The hand lay-up with subsequent pressurization of the green samples may be the major factor in reduction of damping. Increased binding of the polymers with

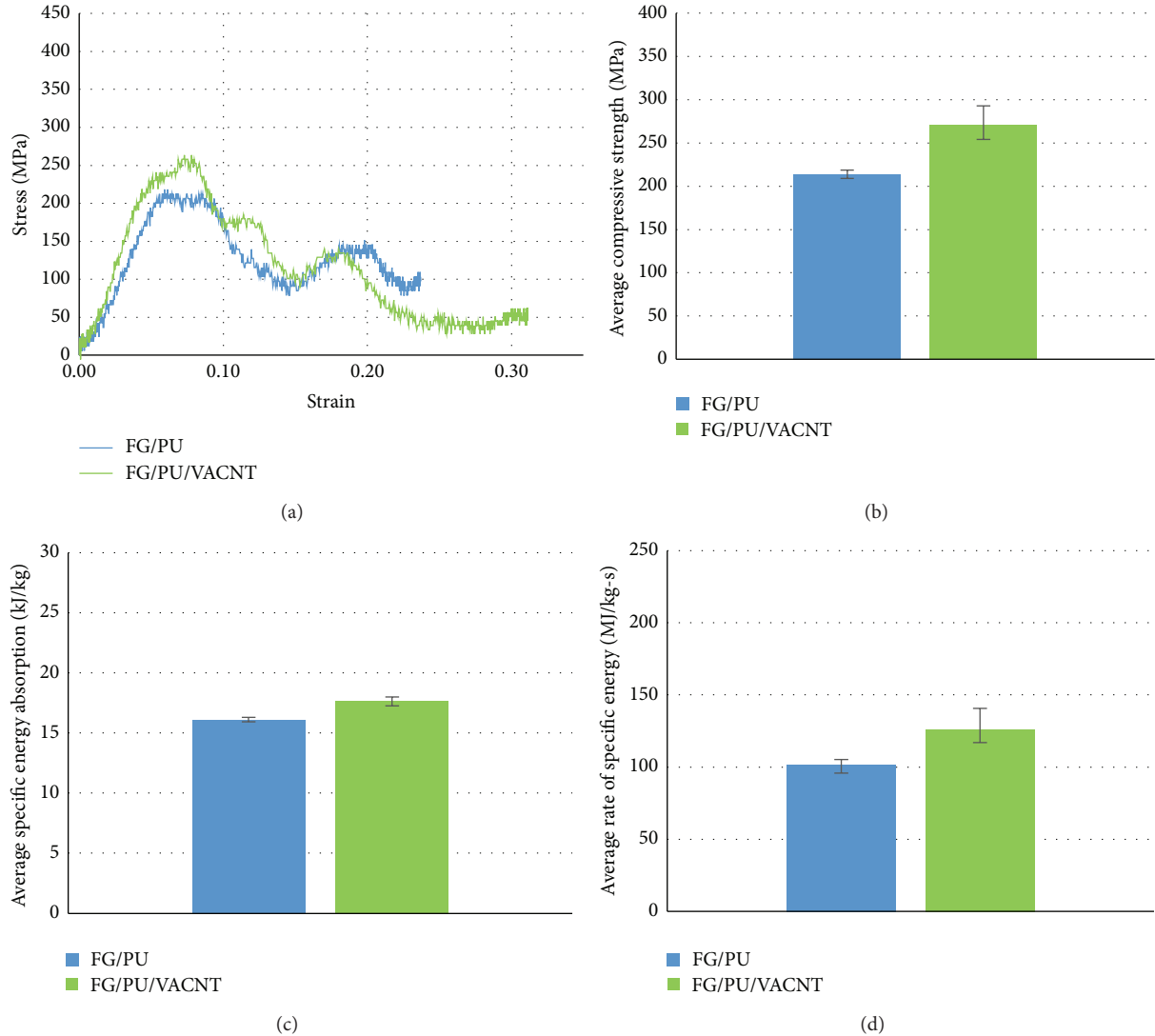


FIGURE 5: SHPB compression test response of FG/PU and FG/PU/VACNT composites evaluated over strain rate of 700 to 800/s: (a) stress-strain curve of FG/PU and FG/PU/VACNT, (b) compressive strength, (c) average specific energy absorption, and (d) rate of specific energy absorption.

the VACNT surface under pressure may also be contributing to the reduced damping.

**3.2. SHPB Results.** The compression SHPB apparatus was used to evaluate the energy absorption characteristics of FG/PE, FG/PU, FG/PE/VACNT, and FG/PU/VACNT specimens. A typical SHPB compression response for FG/PE and FG/PE/VACNT specimens at strain rate of 700 to 800/s is shown in Figure 4. FG/PE/VACNT displayed higher specific energy absorption and rate of specific energy compared to the baseline FG/PE. However, compressive strength in FG/PE/VACNT was marginally lower than baseline FG/PE.

SHPB compression tests were also performed on baseline FG/PU and FG/PU/VACNT specimens at strain rate of 600 to 800/s. Figure 5 shows typical stress-strain curves of FG/PU and FG/PU/VACNT and compares them in terms of average compressive strength, specific energy absorption, and rate

of specific energy. FG/PU/VACNT exhibited higher specific energy absorption and rate of specific energy with respect to the baseline FG/PU. It was also found that the average compressive strength of FG/PU/VACNT increased about 30% with respect to FG/PU (from 214 MPa to 270 MPa).

## 4. Conclusions

Dynamic mechanical behavior and energy absorption characteristics of 10-layer woven fiber-glass fabric with two different resin systems (PE and PU) have been investigated as the baseline; and effects of embedding VACNT layers within these baseline composites were studied. From DMA response, FG/PE/VACNT exhibited a significantly lower flexural stiffness at ambient temperature along with higher damping loss factor over the investigated temperature range with respect to baseline FG/PE. However damping loss

factor was found to be similar as the baseline FG/PE at  $T_g$ . FG/PU/VACNT showed a significantly higher flexural stiffness at ambient temperature along with lower damping loss factor over the investigated temperature range compared to the baseline FG/PU. The loss modulus at RT increased with the addition of VACNT forest layers in both baseline composites (FG/PE and FG/PU), but only FG/PU/VACNT showed an increased loss modulus at  $T_g$ . From SHPB response, FG/PE/VACNT and FG/PU/VACNT showed improved specific energy absorption and rate of specific energy absorption compared to the baseline materials FG/PE and FG/PU. The compressive strength of FG/PU/VACNT increased by about 30% with the addition of VACNT forest layers.

## Conflict of Interests

The authors declare that there is no conflict of interests regarding the publication of this paper.

## Acknowledgments

The financial support from the U.S. Army Engineer Research and Development Center-Construction Engineering Research Laboratory (ERDC-CERL), Champaign, IL, USA, Grant W9132T-12-P0057 is gratefully acknowledged. The authors would like to thank Dr. Brahma Pramanik for his help in performing the DMA and SHPB experiments.

## References

- [1] I. C. Finegan and R. F. Gibson, "Recent research on enhancement of damping in polymer composites," *Composite Structures*, vol. 44, no. 2-3, pp. 89-98, 1999.
- [2] R. M. Mahamood, E. T. Akinlabi, M. Shukla, and S. Pityana, "Functionally graded material: an overview," in *Proceedings of the World Congress on Engineering (WCE '12)*, vol. 3, pp. 1593-1597, London, UK, 2012.
- [3] S. Thomopoulos, T. F. Martin, and R. N. Grishanin, Eds., *Structural Interfaces and Attachments in Biology*, Springer, New York, NY, USA, 2013.
- [4] P. M. Ajayan and J. M. Tour, "Materials science: nanotube composites," *Nature*, vol. 447, no. 7148, pp. 1066-1068, 2007.
- [5] J. N. Coleman, U. Khan, W. J. Blau, and Y. K. Gun'ko, "Small but strong: a review of the mechanical properties of carbon nanotube-polymer composites," *Carbon*, vol. 44, no. 9, pp. 1624-1652, 2006.
- [6] E. T. Thostenson, Z. Ren, and T.-W. Chou, "Advances in the science and technology of carbon nanotubes and their composites: a review," *Composites Science and Technology*, vol. 61, no. 13, pp. 1899-1912, 2001.
- [7] Y. Zeng, L. Ci, B. J. Carey, R. Vajtai, and P. M. Ajayan, "Design and reinforcement: vertically aligned carbon nanotube-based sandwich composites," *ACS Nano*, vol. 4, no. 11, pp. 6798-6804, 2010.
- [8] P. R. Mantena, T. Tadepalli, B. Pramanik et al., "Energy dissipation and the high-strain rate dynamic response of vertically aligned carbon nanotube ensembles grown on silicon wafer substrate," *Journal of Nanomaterials*, vol. 2013, Article ID 259458, 7 pages, 2013.
- [9] K. Kim, *Dynamic mechanical analysis and high strain-rate energy absorption characteristics of vertically aligned carbon nanotube (VACNT) reinforced woven fiber-glass composites [M.S. thesis]*, The University of Mississippi, Oxford, Miss, USA, 2015.
- [10] T. A. Instruments, "Q800 Dynamic Mechanical Analysis Brochure," 2010, <http://www.tainstruments.com/pdf/brochure/dma.pdf>.
- [11] W. W. Chen and B. Song, *Split Hopkinson (Kolsky) Bar: Design, Testing and Applications*, Springer, New York, NY, USA, 2011.

## Research Article

# Oxygen Barrier Properties and Melt Crystallization Behavior of Poly(ethylene terephthalate)/Graphene Oxide Nanocomposites

Anna Szymczyk,<sup>1</sup> Sandra Paszkiewicz,<sup>2</sup> Iwona Pawelec,<sup>1</sup> Sławomir Lisiecki,<sup>3</sup> Marek Jotko,<sup>3</sup> Zdenko Špitalský,<sup>4</sup> Jaroslav Mosnáček,<sup>4</sup> and Zbigniew Roslaniec<sup>2</sup>

<sup>1</sup>Institute of Physics, West Pomeranian University of Technology, Piastow Avenue 19, 70310 Szczecin, Poland

<sup>2</sup>Institute of Materials Science and Engineering, West Pomeranian University of Technology, Piastow Avenue 19, 70310 Szczecin, Poland

<sup>3</sup>Center of Bioimmobilisation and Innovative Packaging Materials, Faculty of Food Sciences and Fisheries, West Pomeranian University of Technology, Klemensa Janickiego Street 35, 71270 Szczecin, Poland

<sup>4</sup>Polymer Institute, Slovak Academy of Sciences, Dúbravská Cesta 9, 845 41 Bratislava 45, Slovakia

Correspondence should be addressed to Anna Szymczyk; [aszymczyk@zut.edu.pl](mailto:aszymczyk@zut.edu.pl)

Received 9 February 2015; Revised 18 May 2015; Accepted 24 May 2015

Academic Editor: Mircea Chipara

Copyright © 2015 Anna Szymczyk et al. This is an open access article distributed under the Creative Commons Attribution License, which permits unrestricted use, distribution, and reproduction in any medium, provided the original work is properly cited.

Poly(ethylene terephthalate) nanocomposites with low loading (0.1–0.5 wt%) of graphene oxide (GO) have been prepared by using *in situ* polymerization method. TEM study of nanocomposites morphology has shown uniform distribution of highly exfoliated graphene oxide nanoplatelets in PET matrix. Investigations of oxygen permeability of amorphous films of nanocomposites showed that the nanocomposites had better oxygen barrier properties than the neat PET. The improvement of oxygen permeability for PET nanocomposite films over the neat PET is approximately factors of 2–3.3. DSC study on the nonisothermal crystallization behaviors proves that GO acts as a nucleating agent to accelerate the crystallization of PET matrix. The evolution of the lamellar nanostructure of nanocomposite and neat PET was monitored by SAXS during nonisothermal crystallization from the melt. It was found that unfilled PET and nanocomposite with the highest concentration of GO (0.5 wt%) showed almost similar values of the long period ( $L = 11.4$  nm for neat PET and  $L = 11.5$  nm for PET/0.5GO).

## 1. Introduction

Since the discovery in 2004 by Novoselov et al. [1], graphene has initiated a growing interest in using it as a filler to polymer materials. Graphene is a one-atom-thick, two-dimensional sheet composed of  $sp^2$  carbon atoms arranged in a plane structure [2], owning high intrinsic mobility ( $2 \cdot 10^5$  cm<sup>2</sup>/Vs) [3, 4], excellent thermal conductivity (2000–5000 W/m·K), extraordinary thermal stability [5–7], remarkable structural flexibility [8, 9] and large surface area [10], with mechanical strength (with Young modulus of 1 TPa and ultimate strength of 130 GPa [9]) approximately 100 times greater than steel, which makes graphene the strongest material ever measured. Because of such superior properties, graphene has attracted much attention for a wide range of applications, including nanocomposites [11–13], sensors [14, 15], field effect transistors [16], transparent conductive films [17], and many more. Graphene is not naturally abundant due to its instability and

tendency to form three-dimensional structures (agglomeration). It can be synthesized by a variety of methods, such as chemical vapor deposition (CVD) [18, 19] arc discharge [20], epitaxial growth on SiC [21–23], chemical conversion [24], reduction of CO [25], unzipping carbon nanotubes [26, 27], and separation/exfoliation of graphite or graphite derivatives (such as graphite oxide (GO) and graphite fluoride) [28]. In addition, fast and low cost production of graphene and few-layer graphene (FLG) with high yield, where the synthesis consisted of mechanical ablation of pencil lead on a harsh glass surface with simultaneous ultrasonication followed by a purification to remove the inorganic binder present in the pencil lead was demonstrated by Janowska et al. [29]. Among those methods, it has been proven that the reduction of exfoliated graphene oxide (GO) is a reliable strategy owing to its cost-effective and massive scalability. Generally, GO is obtained by oxidation of the natural flake graphite in the presence of strong oxidants such as potassium permanganate

mixed with concentrated sulfuric acid, followed by sonication [30, 31]. After oxidation, abundant functional groups (e.g., hydroxyl, carboxyl, epoxy, and ketone) were introduced onto the graphitic layers, and simultaneously part of  $sp^2$ -carbons were converted into  $sp^3$  ones [32]. It is generally considered that the epoxy and carbonyl groups are attached above and below basal planes, while the carboxyl groups are located at the edges [33, 34].

Incorporation of nanofillers into a polymer matrix gives rise to a new class of materials known as polymer nanocomposites, which have greater potential for many applications. Significant improvement in properties of the composites depends mainly on the size and shape of particles nanofiller [35], surface area, degree of surface development, surface energy, and the spatial distribution of the polymer matrix of nanoparticles. It is assumed that the degree of exfoliation plays the critical role in determining the nanocomposites properties. The more homogeneous dispersions of the layered nanofillers (expanded graphite or others graphene derivatives) are, the greater improvements in properties can be obtained. Properties of polymer nanocomposites depend significantly not only on the degree of granularity and uniform dispersion of nanoparticles, but also on the type of polymer matrix and the nature of the nanofiller. In the case of the thermoplastic matrix (such as poly(ethylene terephthalate) (PET) and poly(trimethylene terephthalate) (PTT)), nanofiller may also affect the crystallization rate and degree of crystallinity and the nature of the crystalline phase [36]. Crystallinity is an important field of interest in polymer science and engineering as the crystallinity affects physical properties such as modulus, tensile strength, toughness, hardness, and gas permeability.

Poly(ethylene terephthalate) (PET) is widely used in a range of high barrier applications because of its good mechanical properties and low cost. PET bottles are widely used in fruit juices, drinks, medicines, and food packaging. However, PET material has the poor barrier properties compared with glass and metal containers. Recently, packing industry has been very interested in improvement of barrier properties of PET for additional applications, due to the observed trend to a progressive change towards the use of containers of plastic material. The improvement of PET permeability to oxygen and even carbon dioxide can broaden its application to packing materials which are more sensitive to them. Enhanced barrier properties of PET properties can be achieved with the graphene nanoplatelets (GNPs) due to their unique morphology and size. Also graphene oxide possesses an excellent gas barrier without any chemical reduction [37]. Previous studies reported that GO layers and poly(ethylenimine) (PEI) layers deposited on a PET film surface PET decreased the oxygen transmittance rate (OTR) and light transmittance, and the electric conductivity increased [38]. Kim et al. [37] reported that the oxygen permeability of the poly(vinyl alcohol) (PVA)/reduced graphene oxide (RGO) (0.3 wt%) composite coated film was 17 times lower than that of the pure poly(ethylene terephthalate) (PET) film. Both the diffusivity and the solubility are reduced by dispersing RGO into PVA.

Graphene and graphene oxide and their uses in barrier polymers are broadly discussed in literature [37–41]. The platelet size, stacking orientation, and degree of graphene exfoliation in the polymer matrix are governing factors in determining the gas transport [39].

In our earlier work it was established that by using *in situ* polymerization method it is possible to obtain nanocomposites with highly exfoliated graphene sheets in PET matrix with electrical percolation threshold at 0.05 wt% loading of expanded graphite [42].

In the present study, up to 0.5 wt% of GO was introduced in PET matrix. The effect of GO presence in PET matrix on oxygen barrier properties and nonisothermal crystallization behavior of the obtained PET nanocomposites were investigated. The last studies are of great practical importance because the production of PET the production of PET products, including fiber spinning, extrusion, and injection molding, is largely controlled through nonisothermal crystallization processes. In fact, the interaction between the polymer and the functionalized groups on the surface of graphene sheets can alter the thermal properties of the nanocomposites.

## 2. Experimental

**2.1. Materials.** Poly(ethylene terephthalate) (PET) has been synthesized by using the following chemicals: dimethyl terephthalate (DMT) (Sigma-Aldrich); ethanediol (ED) (Sigma-Aldrich), zinc acetate (ester exchange catalyst)  $Zn(CH_3COO)_2$  (Sigma-Aldrich); antimony trioxide–polycondensation catalyst:  $Sb_2O_3$  (Sigma-Aldrich); thermal stabilizer Irganox 1010 (Ciba-Geigy, Switzerland).

Graphene oxide (GO) with average particle size of  $5\ \mu m$  was provided by Polymer Institute of Slovak Academy of Sciences, where the natural graphite was converted to expanded graphite through chemical oxidation in the presence of concentrated  $H_2SO_4$  and  $HNO_3$  acids reported in [43]. C1s XPS spectra of GO are as follows:  $sp^2$ -C: 60.00%;  $sp^3$ -C: 12.92%; C–O: 9.22%; C=O: 6.42%; COO: 2.95%;  $\pi$ - $\pi$ : 8.49%. O1s XPS spectra of GO are as follows: C=O: 37.45%, C–O: 52.49%, Na–O: 5.86%, and  $SiO_2$ : 4.20%. Before adding nanofillers to the reaction mixture, they were combined with ethanediol in order to split agglomerates and to improve further exfoliation.

**2.2. Preparation of PET/GO Nanocomposite.** PET/GO nanocomposites were prepared by *in situ* polymerization in the steel reactor (Autoclave Engineers, USA) with capacity of  $1000\ cm^3$ . The process was conducted in two stages and followed the same procedure as described in our previous publications [42, 44, 45]. Before polymerization, the desired amount of GO was dispersed in ca. 250–300 mL of ED by using for 15 min intensive mixing with high-speed stirrer (Ultra-Turax T25) and then through ultrasonication for 15 min using sonicator (Homogenizer HD 2200, Sonoplus, with frequency of 20 kHz and 75% of power 200 W). Additionally, to improve the dispersion/exfoliation of GO in ED an ultrapower lower sonic bath (BANDELIN, Sonorex digitec,

with frequency of 35 kHz and power 140 W) was applied for 20 hours.

**2.3. Characterization Techniques.** The inherent viscosity  $[\eta]$  of the polymers was determined at 30°C using an Ubbelohde viscometer (with capillary  $I_c$ ,  $K = 0.03294$ ), as described elsewhere [42, 45–47]. The polymer solution had a concentration of 0.5 g/dL in mixture phenol/1,1,2,2-tetrachloroethane (60/40 by weight). The polymer nanocomposite solution was filtered through 0.2  $\mu\text{m}$  pore size polytetrafluoroethylene (PTFE) filter (Whatman; membrane type TE 35) to ensure that the intrinsic viscosity is not affected by present GO. After filtration, the polymer was precipitated and redissolved. The values of average viscosity molar mass of PET homopolymer was calculated according to the Mark–Houwink equation  $[\eta] = 3.72 \times 10^{-4} \cdot M^{0.73}$  [48].

The melt volume rate (MVR) was measured using a melt indexer (CEAST, Italy) as melt flow in  $\text{cm}^3$  per 10 min, at temperature of 280°C and at orifice diameter 1.050 mm and under 2.160 kg load, according to ISO 1133 specification.

The structure of nanocomposites was observed by transmission electron microscopy (TEM) analysis, which was carried out by a JEOL JEM-1200 Electron Microscope using an acceleration voltage of 80 kV. The TEM samples were thinly sliced (~100 nm) using Reichert Ultracut R ultramicrotome. The thin slice obtained was collected onto a 300 mesh copper grid.

Oxygen permeability was measured using a Mocon-Ox-Tran 2/10 instrument. Oxygen permeability was performed using 5  $\text{cm}^2$  samples of investigated polymer films in accordance with ASTM D3985-05 and ISO 15105-2 Standards. All film samples were additionally conditioned for 3 h in the test chamber of OX-Tran apparatus in test parameters (23°C and 0% humidity rate RH). The measurement was automatically terminated when apparatus obtained stable subsequent results. Samples were dried in vacuum at 80°C for 24 h, compression-moulded, and quenched into amorphous films. The temperature of the press was 255°C and pressure of 15 bar. Films with comparable thickness (330  $\mu\text{m}$ ) were prepared.

XRD diffraction patterns were recorded using a PANalytical X'Pert PRO diffractometer powered by a Philips PW3040/60 X-ray generator and fitted with an X'Celerator detector. The X-ray source (CuK $\alpha$  radiation, wavelength  $\lambda = 1.5418 \text{ \AA}$ ) was generated using an applied voltage of 40 kV and a filament current of 35 mA. The data were collected and recorded in the  $2\theta$  range 4–40 with a step of 0.02.

The nonisothermal crystallization behaviours of samples were investigated using a differential scanning calorimetry (DSC, TA Instruments Q-1000). The samples were heated from room temperature to 270°C at heating rate 10°C/min and maintained for 3 min in the DSC cell to destroy any nuclei that might act as seed crystals. The samples were then cooled to 20°C at constant rate of 3, 5, and 10°C/min, respectively. All the DSC measurements were carried out in nitrogen atmosphere, and the weight of each sample was about 10 mg. The enthalpy of crystallization ( $\Delta H_c$ ) was determined from

the areas of the crystallization peaks. The degree of crystallinity ( $x_c$ , mass fraction) of the samples was calculated using the equation

$$x_c = \frac{\Delta H_c}{\Delta H^0 (1 - w)}, \quad (1)$$

where  $\Delta H^0$  (140 J/g) [44] is the enthalpy of melting for 100% crystalline PET,  $\Delta H_c$  is the enthalpy of crystallization of the sample, and  $w$  is the content of GO.

Small angle X-ray scattering (SAXS) measurements were performed at beam line A2 at HASYLAB (DESY, Hamburg). The wavelength of the X-ray beam was  $\lambda = 0.15 \text{ nm}$ . Scattering patterns were collected by a two-dimensional MAR-CCD-165 detector placed at a distance of 2443 mm from the sample. The scattering-vectors were calibrated using a dray rat-tail tendon protein. The specimens (~25 mg) were mounted in Mettler hot stage and encased between aluminium-foil windows and were heated and cooled at heating rates of 5°C/min over a temperature range of 25–275°C. During cooling from the melt, data was collected with time scanning 60 and accumulation time 20 s. For SAXS data analysis, a computer program SAXSDAT [49] was used. Subsequently the linear correlation function  $CF(x)$  (2) Fourier-transformed from the corresponding one-dimensional SAXS data  $I(s)$  measured is calculated in this work following procedures described in [49]:

$$CF(x) = \frac{1}{Q} \int_0^\infty I(s) s^2 \cos(2\pi sx) ds. \quad (2)$$

The parameter  $Q$  in (2) is a measure of the scattering power of the system:

$$Q = \int_0^\infty I(s) s^2 ds = K \alpha_s (\rho_c - \rho_a)^2 \varphi_L (1 - \varphi_L), \quad (3)$$

where  $\rho_c$  is the electron density of the lamellar crystals,  $\rho_a$  is the electron density of the amorphous material between adjacent lamellae,  $\alpha_s$  is the volume fraction of the lamellar crystals in the irradiated sample volume, and  $K$  is the a constant depending on the experimental conditions. From the correlation function, we estimate long period  $L$  (the first maximum) and the linear crystallinity  $\varphi_L$  using the equation [49–51]

$$\varphi_L (1 - \varphi_L) = \frac{P}{L}, \quad (4)$$

where  $P$  is the position of the first intercept of the correlation function with the  $x$ -axis. The thickness of the crystalline ( $l_c$ ) and amorphous ( $l_a$ ) layers in the stacks was calculated according to

$$\begin{aligned} l_l &= \varphi_L L, \\ l_a &= (1 - \varphi_L) L. \end{aligned} \quad (5)$$

The relationship between volume fraction of crystallinity and linear crystallinity is expressed as  $x_v = \alpha_s \varphi_L$ , where  $\alpha_s$  is the fraction of the total volume of the sample occupied by stacks of lamellae [51]. Using the densities of the crystalline ( $d_c = 1.445 \text{ g/cm}^3$ ) and amorphous ( $d_a = 1.331 \text{ g/cm}^3$ ) phases

TABLE 1: Physical properties of neat PET and PET/GO nanocomposites.

Sample	$[\eta]$ dL/g	$M_v \times 10^4$ g/mol	MVR cm <sup>3</sup> /10 min
PET	0.536	2.124	72.8 ± 1.9
PET/0.1GO	0.532	2.100	72.5 ± 1.8
PET/0.3GO	0.529	2.090	71.9 ± 2.5
PET/0.5GO	0.499	1.927	72.8 ± 1.4

$[\eta]$ : intrinsic viscosity;  $M_v$ : average viscosity molecular weight; MVR: melt volume rate at 280°C.

for PET [52], the volume fraction crystallinity ( $x_v = \phi_L$ ) was transformed into mass fraction of crystallinity  $x_{c,m}$  according to Swam equation [53]:

$$x_{c,m} = \left[ 1 + \frac{d_a}{d_c} \left( \frac{1 - x_v}{x_v} \right) \right]^{-1}. \quad (6)$$

### 3. Results and Discussion

**3.1. Characterization of the PET/GO Nanocomposites.** PET nanocomposites with low loading of graphene oxide (GO) were synthesized by *in situ* polymerization of monomers in the presence of GO sheets. Ultrasonication graphite oxide in monomer (ED) before synthesis and then polymerization was found to be an effective way to obtain PET nanocomposites with highly exfoliated GO into while maintaining a very high aspect. Additionally, for comparison purposes, unmodified PET was synthesized and characterized in the same manner as the nanocomposite. The characteristics of the obtained nanocomposites are presented in Table 1. The intrinsic viscosity of neat PET was 0.536 dL/g.

The presence of the GO in the polymerization mixture affected the reaction, leading to the slightly decrease of intrinsic viscosity. As shown in Table 1, the intrinsic viscosity decreased with the addition of GO to 0.499. The PET matrix in synthesized nanocomposites have high molecular weight, which is ranged between 21 000 and 19 200 g/mol and is close to the value for neat PET. The comparable value of melt volume rate for neat PET and PET/GO nanocomposites was due to the polymer-functionalized graphene sheets interactions.

The dispersion and exfoliation of functionalized graphene sheets (GO) in PET matrix were investigated using TEM analysis and representative images for composite with loading of 0.3 and 0.5 wt% are shown in Figure 1.

TEM images of the PET/GO nanocomposites demonstrate that the highly exfoliated graphene oxide nanoplatelets were rather uniformly dispersed in PET matrix. The presence of more or less transparent and graphene nanoplatelets conforms with high degree of exfoliation, although predominance of folded multilayer graphene and some small aggregates on the nanoscopic scale was observed. This was due to the extremely high specific area of GO and the strong particle-matrix interactions that take place. The fact that the graphene oxide flakes remain well-exfoliated and highly dispersed within PET matrix suggests these composites to potentially display gas barrier property improvement.

TABLE 2: Oxygen permeability of PET/GO nanocomposite films.

Sample	GO wt %	Thickness $\mu\text{m}$	O <sub>2</sub> transmission rate <sup>a</sup> cm <sup>3</sup> /m <sup>2</sup> 24 h
PET	—	320	48.6 ± 3.7
PET/0.1GO	0.1	326	23.7 ± 2.3
PET/0.3GO	0.3	322	18.6 ± 1.6
PET/0.5GO	0.5	320	14.6 ± 2.1

<sup>a</sup>Measured at 23°C and 0% relative humidity.

**3.2. Oxygen Permeability of PET/GO Nanocomposites.** Graphene nanoplatelets are believed to increase gas barrier properties in nanocomposites. The tortuous path being created by the graphene particles in PET nanocomposites can retards the diffusion of the gas molecules through the PET matrix region. The influence of functionalized graphene (GO) content on the barrier performance to oxygen was studied by investigating oxygen transmission rate of PET/GO nanocomposites.

Gas barrier properties of PET films can be influenced by sample crystallinity and thickness [54]. In order to avoid crystallinity effect on oxygen barrier properties of PET/GO nanocomposites the amorphous films with comparable thickness were prepared.

Figure 2 shows X-ray diffraction patterns of GO, neat PET, and PET/GO composite films. The X-ray patterns for PET and PET/GO nanocomposite films have a broad amorphous halo confirming that prepared films were amorphous. The X-ray diffraction patterns for GO give peaks at  $2\theta = 12.5^\circ$  and  $2\theta = 26.3^\circ$ . The first peak corresponds to an interlayer spacing of 0.71 nm (002) indicating the presence of oxygen functional group. The second peak corresponds to (002) plane of graphite with interlayer spacing of 0.34 nm. The presence of any GO peaks in the XRD spectra of PET/GO nanocomposites can suggests that GO was well exfoliated and homogenous dispersed in the PET matrix. On the other hand, GO content in PET matrix can be too low to observe these peaks on X-ray diffraction spectra of PET/GO nanocomposite films.

The oxygen barrier properties through neat PET and PET/GO composite films with comparable thickness are listed in Table 2. The obtained results of oxygen transmission rate (OTR) for amorphous PET films are comparable with literature data [54]. As expected, the permeability of O<sub>2</sub> through the PET/GO nanocomposite films was found considerably reduced at low loading of GO. The improvement of O<sub>2</sub> permeability for PET nanocomposite films over the neat PET is approximately factors of 2–3.3.

Based on many studies of gas barrier properties of polymer-layered silicate nanocomposites, it was established that enhancements in gas barrier properties depend on factors such as the relative orientation of the nanofiller sheets in the polymer matrix and the state of aggregation and dispersion in polymer matrix, that is, intercalated, exfoliated, or mixed morphology [55]. For PET nanocomposites containing graphene nanoplatelets the mechanism of gas barrier properties enhancement can be influenced by many factors similar to polymer-layered silicate nanocomposites, for which the level of exfoliation of silicate layers is a critical

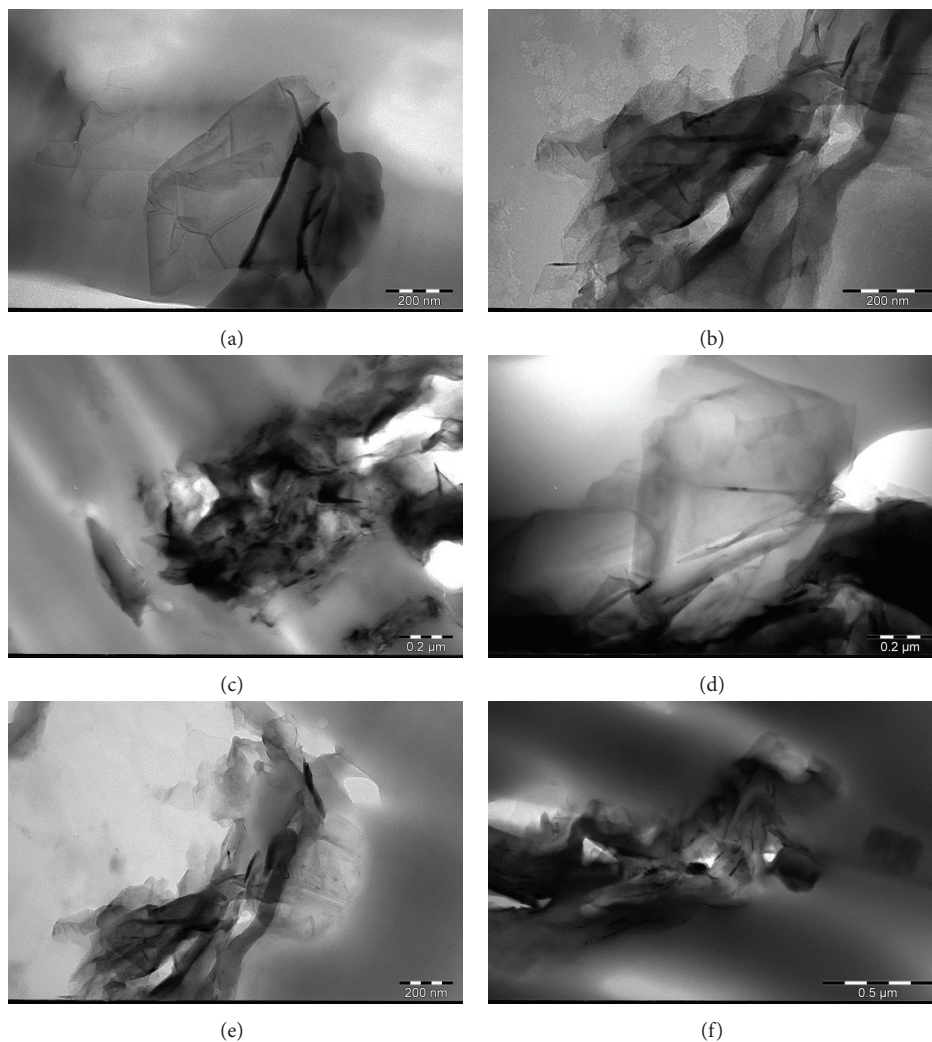


FIGURE 1: TEM images of PET/GO nanocomposite with 0.3 wt% (a–b) and 0.5 wt% (c–f) of GO. Image magnification: (a) 150 k, (b) 200 k, (c) 50 k, (d) 150 k, (e) 120 k, and (f) 100 k.

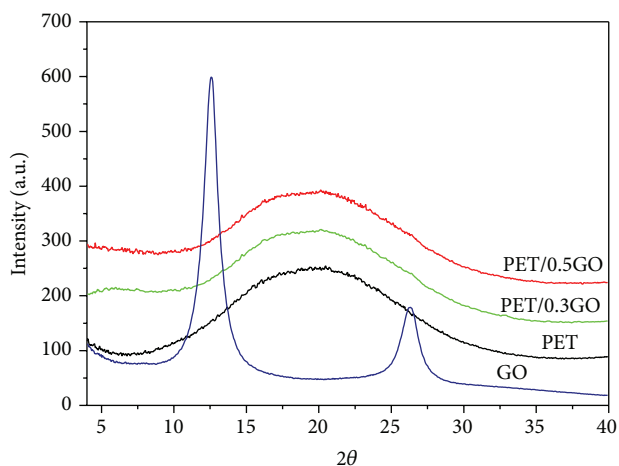


FIGURE 2: XRD diffractograms for GO, neat PET, and PET/GO nanocomposite films.

factor in determining the maximum performance of polymer silicate nanocomposites for barrier applications [56].

### 3.3. Effect of GO on Crystallization of PET Nanocomposites.

The effect of graphene oxide nanoplatelets on the non-isothermal crystallization of PET was investigated using DSC. Figure 3 shows the DSC cooling curves obtained at different cooling rates. Additionally, temperature-resolved SAXS studies of morphological changes in melt-crystallized PET and PET/GO composite with the highest concentration of GO (0.5 wt%) were carried out.

The values of the nonisothermal crystallization onset temperatures ( $T_{c,on}$ ), crystallization peak temperatures ( $T_c$ ), and the crystallization enthalpies of all the samples under different cooling rates (3, 5, and 10°C/min) are presented in Table 3. For all samples, the crystallization onset temperature and crystallization peak temperature decrease as the cooling rate increases. Compared with neat PET, it is observed that at given cooling rate, the onset and peak crystallization temperatures of the PET/GO nanocomposites was increased due to the presence of GO. It can be also seen that the width of crystallization peak for nanocomposites was less than for neat PET. The value of ( $T_{c,on} - T_c$ ) reflects the overall crystallization rate of the sample; the lower value of the

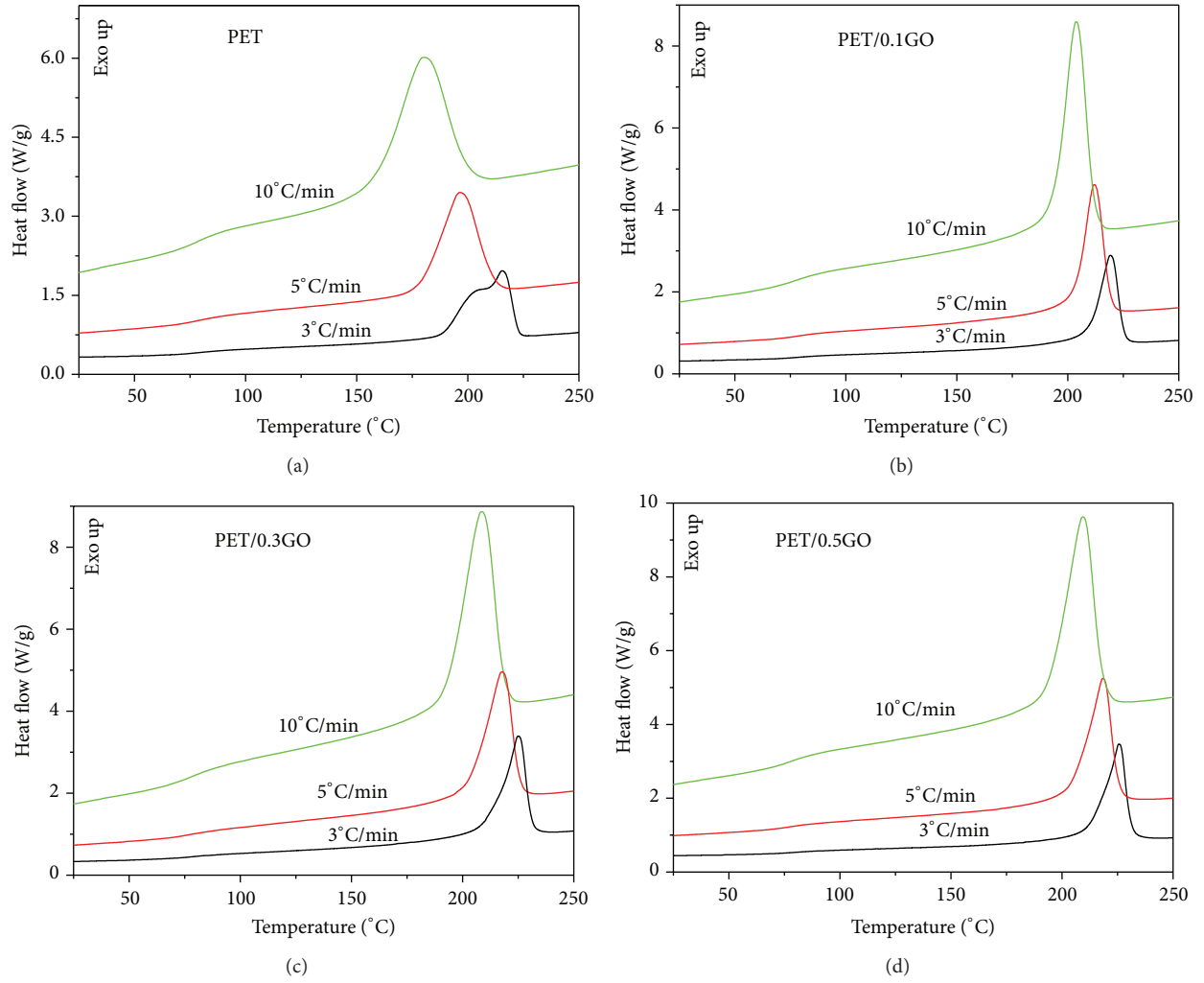


FIGURE 3: DSC thermograms of neat PET (a) and PET/GO nanocomposites with 0.1 (b), 0.3 (c), and 0.5 (d) wt% of GO at different cooling rates.

TABLE 3: DSC data obtained from the cooling runs for PET/GO nanocomposites.

Sample	Scan rate °C/min	$T_{c,on}$ °C	$T_c$ °C	$T_{c,on} - T_c$ °C	$\Delta H_c$ J/g	$x_c$
PET	3	222	215	7	52.9	0.378
	5	211	196	15	47.7	0.341
	10	200	180	20	42.7	0.305
PET/0.1GO	3	225	219	6	51.4	0.367
	5	219	212	7	47.8	0.342
	10	212	203	9	43.2	0.309
PET/0.3GO	3	231	225	6	63.2	0.453
	5	225	217	8	56.2	0.403
	10	218	208	10	51.5	0.369
PET/0.5GO	3	231	225	6	63.6	0.456
	5	225	218	7	57.9	0.416
	10	218	209	9	52.5	0.377

$T_{c,on}$ ,  $T_c$ : onset and peak crystallization temperature,  $\Delta H_c$ : enthalpy of crystallization, and  $x_c$ : mass fraction of crystallinity.

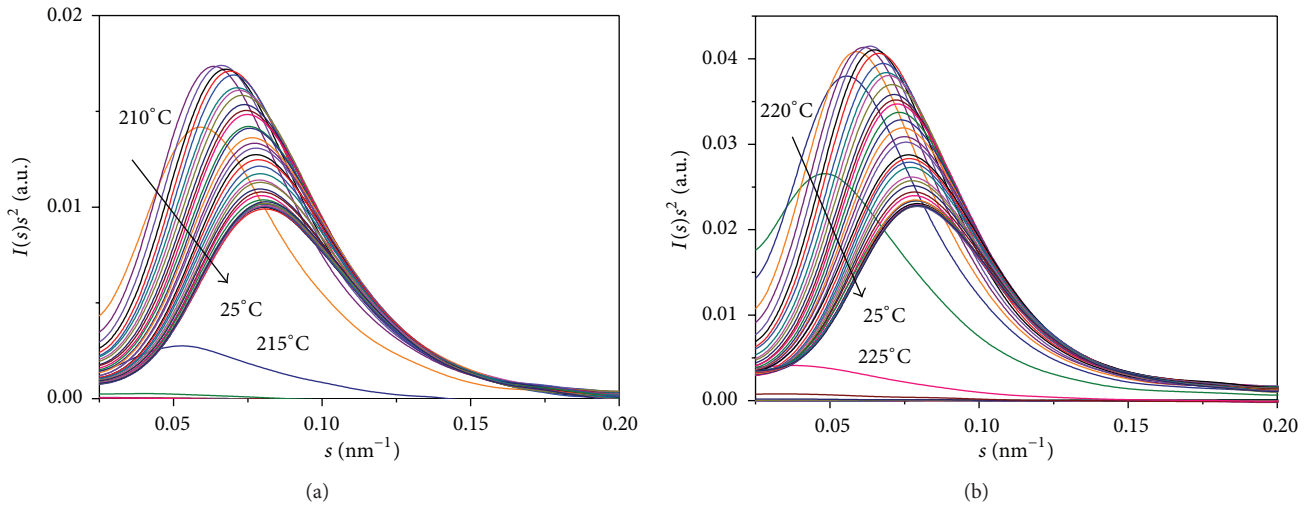


FIGURE 4: The evolution of the Lorentz corrected SAXS patterns (after background correction) during crystallization of (a) neat PET and (b) PET/0.5GO nanocomposite.

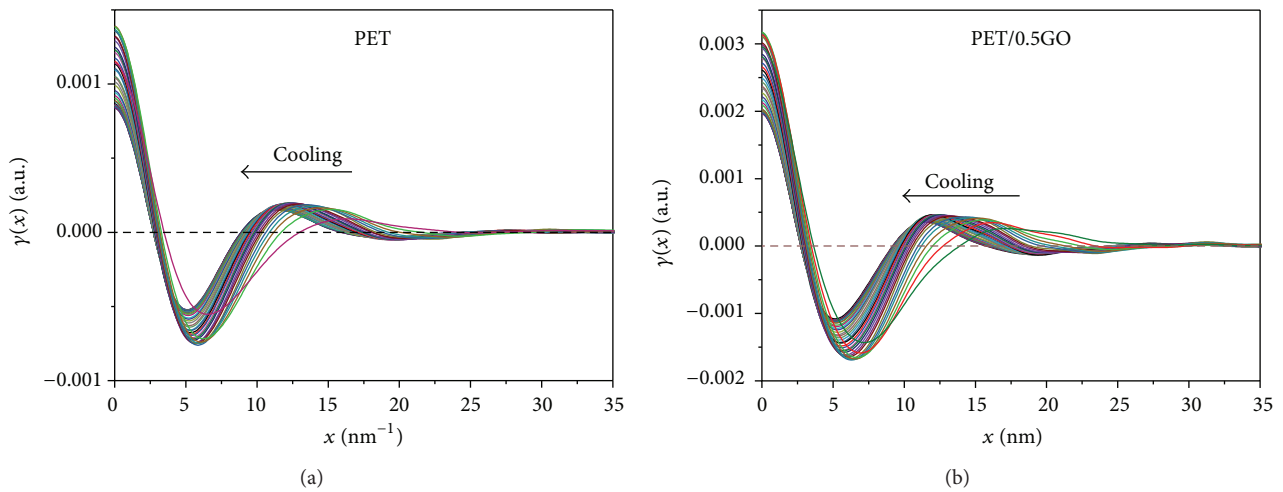


FIGURE 5: One-dimensional correlation function for neat PET (a) and PET/0.5GO nanocomposite (b) during cooling at  $5^\circ\text{C}/\text{min}$  from the melt.

$(T_{c,on} - T_c)$  for nanocomposites especially at higher cooling rates (Table 3) indicates the higher overall crystallization rate. Moreover, the nonisothermally crystallized PET composites with 0.3 and 0.5 wt% of GO have higher degree of crystallinity than neat PET. These can indicate the efficiency of graphene oxide nanoplatelets at low loading as nucleation agents for crystallization of PET.

Effect of the presence of GO in PET matrix on the evolution of the lamellar nanostructure was monitored by SAXS during nonisothermal crystallization from the melt. The correlation function  $\gamma(x)$  has been applied to follow the changes of the nanostructure of PET/GO composite and neat PET during crystallization from the melt. Figure 4 displays the evolution of SAXS patterns for neat PET and nanocomposite (PET/0.5GO) during cooling. According to procedure reported in [49–51] analysis of the  $\gamma(x)$  (Figure 5) allows to determine:  $L$ ,  $l_c$ ,  $l_a$ , and crystallinity within the lamellar stacks ( $\phi_L$ ).

Figure 6 summarizes the results of the nanostructure studies during melt crystallization of neat PET and nanocomposite with loading of 0.5 wt% of GO. These data indicate that the average values of lamellar thickness accompanied by the decrease of the amorphous layer  $l_a$  decreases with decreasing temperature and consistent with previous data for other crystalline polymers and their nanocomposites [57–59]. The observed in the higher-temperature region sharp decrease of the average value of  $l_a$  could be connected with the sequential formation of either new crystal lamellae or lamellar stacks or both in the interlamellar amorphous regions [58, 59].

Finally, unfilled PET and nanocomposite showed almost the similar values of the long period ( $L = 11.4$  nm for neat PET and  $L = 11.5$  nm for PET/0.5GO, Table 4). Nanocomposite has comparable thickness of crystalline lamellae (Table 4) as neat PET. Slightly higher value of  $l_c$  for nanocomposite in comparison to unfilled PET was observed. The obtained volume and mass fraction crystallinity for

TABLE 4: Parameters of nanostructure determined from correlation function for neat PET and PET/0.5GO nanocomposite.

Sample	$L$ [nm]	$l_c$ [nm]	$l_a$ [nm]	$E$ [nm]	$\varphi_L$	$x_{c,m}$
PET	11.40	4.412	6.988	2.103	0.387	0.406
PET/0.5GO	11.51	4.627	6.883	1.969	0.402	0.422

$L$ : long period;  $l_c$ : thickness of crystalline lamellae;  $l_a$ : thickness of amorphous layer;  $E$ : thickness of transition layer;  $\varphi_L$ : volume fraction of crystallinity;  $x_{c,m}$ : mass fraction of crystallinity determined from (6).

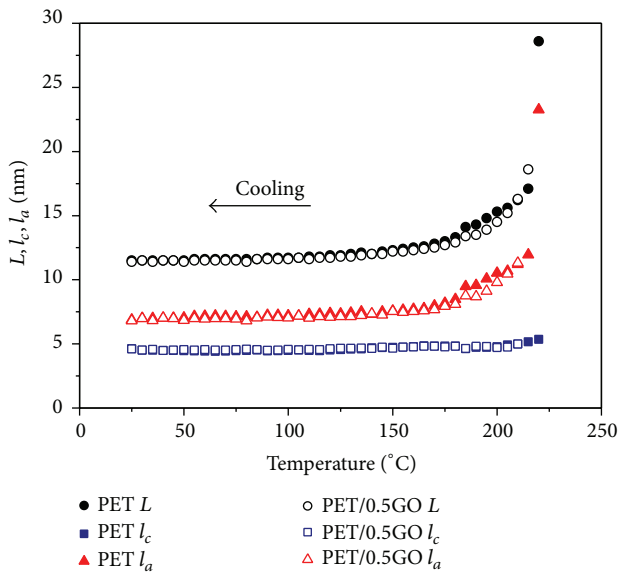


FIGURE 6: Changes of long period ( $L$ ), thickness of crystalline, and amorphous layer ( $l_c$ ,  $l_a$ ) calculated from the one-dimensional correlation function for neat PET and PET/0.5GO nanocomposite during crystallization from the melt.

nanocomposite (0.402 and 0.422) are slightly higher than for neat PET (0.387 and 0.406).

The observed difference between values of mass fraction crystallinity determined by DSC (Table 3) and SAXS (Table 4) can be explained by different sample size, differences in thermal history, and the different selectivity of the method. Such differences can be excluded only by the simultaneous measurements with different techniques at the same sample volume, which reflect an identical thermophysical history.

#### 4. Conclusions

The obtained PET nanocomposites with low loading of GO prepared by *in situ* polymerization show uniform dispersion of highly exfoliated graphene oxide nanosheets in PET matrix. Study of the oxygen transmission rate through nanocomposite and neat PET films has shown that the high aspect ratio and exfoliated structure of GO in PET matrix improved their oxygen barrier properties. The improvement of oxygen permeability for PET nanocomposite films at 0.3–0.5 wt% loading of GO over the neat PET is approximately factors of 2–3.3. These improvements of oxygen barrier properties of PET are important from the application point of view

in packing industry. For example oxygen sensitive materials can be stored in PET containers and their life time can be elongated. DSC study of nonisothermal crystallization of nanocomposites have shown that the graphene oxide nanosheets displayed a nucleating effect on the PET crystallization due to the increase in the onset and peak crystallization temperature of nanocomposites compared to neat PET. The degree of crystallinity of the nanocomposites containing of 0.3 and 0.5 wt% of GO are higher than for the neat PET. Analysis of nanostructure parameters obtained from SAXS measurements for PET/0.5GO composite and neat PET have shown that nonisothermally crystallized composite and neat PET have comparable values of long period.

#### Conflict of Interests

The authors declare that there is no conflict of interests regarding the publication of this paper.

#### Acknowledgments

The authors thank the financial support from MNT ERA-NET 2012 Project (APGRAPHEL) for sponsoring the study. The experiments performed at A2 in HASYLAB (DESY) were done using the beamtime of the proposal I-20110255EC. Iwona Pawelec would like to acknowledge financial support from West Pomeranian University of Technology (Dean's grant for young scientists).

#### References

- [1] K. S. Novoselov, A. K. Geim, S. V. Morozov et al., "Electric field effect in atomically thin carbon films," *Science*, vol. 306, no. 5696, pp. 666–669, 2004.
- [2] H. Kim, A. A. Abdala, and C. W. MacOsko, "Graphene/polymer nanocomposites," *Macromolecules*, vol. 43, no. 16, pp. 6515–6530, 2010.
- [3] K. I. Bolotin, K. J. Sikes, Z. Jiang et al., "Ultrahigh electron mobility in suspended graphene," *Solid State Communications*, vol. 146, no. 9–10, pp. 351–355, 2008.
- [4] K. S. Novoselov, A. K. Geim, S. V. Morozov et al., "Two-dimensional gas of massless Dirac fermions in graphene," *Nature*, vol. 438, no. 7065, pp. 197–200, 2005.
- [5] A. A. Balandin, S. Ghosh, W. Bao et al., "Superior thermal conductivity of single-layer graphene," *Nano Letters*, vol. 8, no. 3, pp. 902–907, 2008.
- [6] A. A. Balandin, "Thermal properties of graphene and nanostructured carbon materials," *Nature Materials*, vol. 10, no. 8, pp. 569–581, 2011.
- [7] J. D. Renteria, D. L. Nika, and A. A. Balandin, "Graphene thermal properties: applications in thermal management and energy storage," *Applied Sciences*, vol. 4, no. 4, pp. 525–547, 2014.
- [8] D. A. Dikin, S. Stankovich, E. J. Zimney et al., "Preparation and characterization of graphene oxide paper," *Nature*, vol. 448, no. 7152, pp. 457–460, 2007.
- [9] C. Lee, X. Wei, J. W. Kysar, and J. Hone, "Measurement of the elastic properties and intrinsic strength of monolayer graphene," *Science*, vol. 321, no. 5887, pp. 385–388, 2008.

- [10] A. Peigney, C. Laurent, E. Flahaut, R. R. Bacsa, and A. Rousset, "Specific surface area of carbon nanotubes and bundles of carbon nanotubes," *Carbon*, vol. 39, no. 4, pp. 507–514, 2001.
- [11] S. Stankovich, D. A. Dikin, G. H. B. Dommett et al., "Graphene-based composite materials," *Nature*, vol. 442, no. 7100, pp. 282–286, 2006.
- [12] H. J. Salavagione, G. Martínez, and M. A. Gómez, "Synthesis of poly(vinyl alcohol)/reduced graphite oxide nanocomposites with improved thermal and electrical properties," *Journal of Materials Chemistry*, vol. 19, no. 28, pp. 5027–5032, 2009.
- [13] T. Ramanathan, A. A. Abdala, S. Stankovich et al., "Functionalized graphene sheets for polymer nanocomposites," *Nature Nanotechnology*, vol. 3, no. 6, pp. 327–331, 2008.
- [14] L. Al-Mashat, K. Shin, K. Kalantar-Zadeh et al., "Graphene/polyaniline nanocomposite for hydrogen sensing," *The Journal of Physical Chemistry C*, vol. 114, no. 39, pp. 16168–16173, 2010.
- [15] Y. Dan, Y. Lu, N. J. Kybert, Z. Luo, and A. T. C. Johnson, "Intrinsic response of graphene vapor sensors," *Nano Letters*, vol. 9, no. 4, pp. 1472–1475, 2009.
- [16] Y. B. Zhang, Y.-W. Tan, H. L. Stormer, and P. Kim, "Experimental observation of the quantum Hall effect and Berry's phase in graphene," *Nature*, vol. 438, no. 7065, pp. 201–204, 2005.
- [17] S. Park and R. S. Ruoff, "Chemical methods for the production of graphenes," *Nature nanotechnology*, vol. 4, no. 4, pp. 217–224, 2009.
- [18] X. Wang, H. You, F. Liu et al., "Large-scale synthesis of few-layered graphene using CVD," *Chemical Vapor Deposition*, vol. 15, no. 1–3, pp. 53–56, 2009.
- [19] Y. Wang, X. Chen, Y. Zhong, F. Zhu, and K. P. Loh, "Large area, continuous, few-layered graphene as anodes in organic photovoltaic devices," *Applied Physics Letters*, vol. 95, no. 6, Article ID 063302, 2009.
- [20] S. Karmakar, N. V. Kulkarni, A. B. Nawale et al., "A novel approach towards selective bulk synthesis of few-layer graphenes in an electric arc," *Journal of Physics D: Applied Physics*, vol. 42, no. 11, Article ID 115201, 2009.
- [21] W. A. de Heer, C. Berger, X. Wu et al., "Epitaxial graphene," *Solid State Communications*, vol. 143, no. 1–2, pp. 92–100, 2007.
- [22] P. W. Sutter, J.-I. Flege, and E. A. Sutter, "Epitaxial graphene on ruthenium," *Nature Materials*, vol. 7, no. 5, pp. 406–411, 2008.
- [23] Th. Seyller, A. Bostwick, K. V. Emtsev et al., "Epitaxial graphene: a new material," *Physica Status Solidi (B)*, vol. 245, no. 7, pp. 1436–1446, 2008.
- [24] Y. Carissan and W. Klopffer, "Growing graphene sheets from reactions with methyl radicals: a quantum chemical study," *ChemPhysChem*, vol. 7, no. 8, pp. 1770–1778, 2006.
- [25] C.-D. Kim, B.-K. Min, and W.-S. Jung, "Preparation of graphene sheets by the reduction of carbon monoxide," *Carbon*, vol. 47, no. 6, pp. 1610–1612, 2009.
- [26] A. Hirsch, "Unzipping carbon nanotubes: a peeling method for the formation of graphene nanoribbons," *Angewandte Chemie*, vol. 48, no. 36, pp. 6594–6596, 2009.
- [27] L. Jiao, L. Zhang, X. Wang, G. Diankov, and H. Dai, "Narrow graphene nanoribbons from carbon nanotubes," *Nature*, vol. 458, no. 7240, pp. 877–880, 2009.
- [28] K. A. Worsley, P. Ramesh, S. K. Mandal, S. Niyogi, M. E. Itkis, and R. C. Haddon, "Soluble graphene derived from graphite fluoride," *Chemical Physics Letters*, vol. 445, no. 1–3, pp. 51–56, 2007.
- [29] I. Janowska, F. Vigneron, D. Bégin et al., "Mechanical thinning to make few-layer graphene from pencil lead," *Carbon*, vol. 50, no. 8, pp. 3106–3110, 2012.
- [30] W. S. Hummers Jr. and R. E. Offeman, "Preparation of graphitic oxide," *Journal of the American Chemical Society*, vol. 80, no. 6, p. 1339, 1958.
- [31] D. R. Dreyer, S. Park, C. W. Bielawski, and R. S. Ruoff, "The chemistry of graphene oxide," *Chemical Society Reviews*, vol. 39, no. 1, pp. 228–240, 2010.
- [32] W. Gao, L. B. Alemany, L. Ci, and P. M. Ajayan, "New insights into the structure and reduction of graphite oxide," *Nature Chemistry*, vol. 1, no. 5, pp. 403–408, 2009.
- [33] A. B. Bourlinos, D. Gournis, D. Petridis, T. Szabó, A. Szeri, and I. Dékány, "Graphite oxide: chemical reduction to graphite and surface modification with primary aliphatic amines and amino acids," *Langmuir*, vol. 19, no. 15, pp. 6050–6055, 2003.
- [34] S. Stankovich, D. A. Dikin, R. D. Piner et al., "Synthesis of graphene-based nanosheets via chemical reduction of exfoliated graphite oxide," *Carbon*, vol. 45, no. 7, pp. 1558–1565, 2007.
- [35] A. K. Geim and K. S. Novoselov, "The rise of graphene," *Nature Materials*, vol. 6, no. 3, pp. 183–191, 2007.
- [36] Y. Wang, C. Shen, and J. Chen, "Nonisothermal cold crystallization kinetics of poly(ethylene terephthalate)/clay nanocomposite," *Polymer Journal*, vol. 35, no. 11, pp. 884–889, 2003.
- [37] H. M. Kim, J. K. Lee, and H. S. Lee, "Transparent and high gas barrier films based on poly(vinyl alcohol)/graphene oxide composites," *Thin Solid Films*, vol. 519, no. 22, pp. 7766–7771, 2011.
- [38] L. Yu, Y.-S. Lim, J. H. Han et al., "A graphene oxide oxygen barrier film deposited via a self-assembly coating method," *Synthetic Metals*, vol. 162, no. 7–8, pp. 710–714, 2012.
- [39] B. M. Yoo, H. J. Shin, H. W. Yoon, and H. B. Park, "Graphene and graphene oxide and their uses in barrier polymers," *Journal of Applied Polymer Science*, vol. 131, no. 1, Article ID 39628, 2014.
- [40] Y. Su, V. G. Kravets, S. L. Wong, J. Waters, A. K. Geim, and R. R. Nair, "Impermeable barrier films and protective coatings based on reduced graphene oxide," *Nature Communications*, vol. 5, article 4843, 2014.
- [41] H.-D. Huang, P.-G. Ren, J. Chen, W.-Q. Zhang, X. Ji, and Z.-M. Li, "High barrier graphene oxide nanosheet/poly(vinyl alcohol) nanocomposite films," *Journal of Membrane Science*, vol. 409–410, pp. 156–163, 2012.
- [42] S. Paszkiewicz, A. Szymczyk, M. Soccio, J. Mosnáček, T. A. Ezquerro, and Z. Roslaniec, "Electrical conductivity of poly(ethylene terephthalate)/expanded graphite nanocomposites prepared by *in situ* polymerization," *Journal of Polymer Science, Part B: Polymer Physics*, vol. 50, no. 23, pp. 1645–1652, 2012.
- [43] Z. Špitalský, M. Danko, and J. Mosnáček, "Preparation of functionalized graphene sheets," *Current Organic Chemistry*, vol. 15, no. 8, pp. 1133–1150, 2011.
- [44] S. Paszkiewicz, A. Szymczyk, Z. Špitalský, M. Soccio, J. Mosnáček, and Z. Roslaniec, "Morphology and thermal properties of expanded graphite (EG)/poly(ethylene terephthalate) (PET) nanocomposites," *Chemik*, vol. 66, no. 1, pp. 21–30, 2012.
- [45] J. J. Hernández, M. C. García-Gutiérrez, A. Nogales et al., "Influence of preparation procedure on the conductivity and transparency of SWCNT-polymer nanocomposites," *Composites Science and Technology*, vol. 69, no. 11–12, pp. 1867–1872, 2009.
- [46] A. Szymczyk, Z. Roslaniec, M. Zenker et al., "Preparation and characterization of nanocomposites based on COOH functionalized multi-walled carbon nanotubes and on poly(trimethylene terephthalate)," *Express Polymer Letters*, vol. 5, no. 11, pp. 977–995, 2011.

- [47] A. Szymczyk, "Structure and properties of new polyester elastomers composed of poly(trimethylene terephthalate) and poly(ethylene oxide)," *European Polymer Journal*, vol. 45, no. 9, pp. 2653–2664, 2009.
- [48] K. A. Anand, U. S. Agarwal, and R. Joseph, "Carbon nanotubes-reinforced PET nanocomposite by melt-compounding," *Journal of Applied Polymer Science*, vol. 104, no. 5, pp. 3090–3095, 2007.
- [49] S. Rabiej and M. Rabiej, "Determination of the parameters of lamellar structure of semicrystalline polymers using a computer program SAXSDAT," *Polimery*, vol. 56, no. 9, pp. 662–670, 2011.
- [50] W. Ruland, "Small-angle scattering of two-phase systems: determination and significance of systematic deviations from Porod's law," *Journal of Applied Crystallography*, vol. 4, no. 1, pp. 70–73, 1971.
- [51] B. Goderis, H. Reynares, M. H. J. Koch, and V. B. F. Mathot, "Use of SAXS and linear correlation functions for the determination of the crystallinity and morphology of semi-crystalline polymers. Application to linear polyethylene," *Journal of Polymer Science, Part B: Polymer Physics*, vol. 37, no. 14, pp. 1715–1738, 1999.
- [52] J. B. Brolley, D. I. Bower, and I. M. Ward, "Finite difference modeling of the gas transport process in glassy polymers," *Journal of Polymer Science Part B: Polymer Physics*, vol. 34, no. 4, pp. 761–768, 1996.
- [53] P. R. Swam, "Polyethylene specific volume, crystallinity, and glass transition," *Journal of Polymer Science*, vol. 42, no. 140, pp. 525–534, 1960.
- [54] R. Y. F. Liu, Y. S. Hu, M. R. Hibbs et al., "Improving oxygen barrier properties of poly(ethylene terephthalate) by incorporating isophthalate. I. Effect of orientation," *Journal of Applied Polymer Science*, vol. 98, no. 4, pp. 1615–1628, 2005.
- [55] G. Choudalakis and A. D. Gotsis, "Permeability of polymer/clay nanocomposites: a review," *European Polymer Journal*, vol. 45, no. 4, pp. 967–984, 2009.
- [56] R. K. Bharadwaj, "Modeling the barrier properties of polymer-layered silicate nanocomposites," *Macromolecules*, vol. 34, no. 26, pp. 9189–9192, 2001.
- [57] A. Szymczyk and Z. Roslaniec, "Non-isothermal crystallization of poly(trimethylene terephthalate)/single-walled carbon nanotubes nanocomposites," *Polimery*, vol. 57, no. 3, pp. 221–227, 2012.
- [58] A. Sanz, A. Nogales, T. A. Ezquerro, M. Soccio, A. Munari, and N. Lotti, "Cold crystallization of poly(trimethylene terephthalate) as revealed by simultaneous WAXS, SAXS, and dielectric spectroscopy," *Macromolecules*, vol. 43, no. 2, pp. 671–679, 2010.
- [59] R. Verrna, H. Marand, and B. Hsiao, "Morphological changes during secondary crystallization and subsequent melting in poly(ether ether ketone) as studied by real time small angle X-ray scattering," *Macromolecules*, vol. 29, no. 24, pp. 7767–7775, 1996.

## Research Article

# An Ensemble Learning for Predicting Breakdown Field Strength of Polyimide Nanocomposite Films

Hai Guo,<sup>1,2</sup> Jinghua Yin,<sup>1</sup> Jingying Zhao,<sup>2,3</sup> Lei Yao,<sup>1,4</sup> Xu Xia,<sup>1</sup> and Hao Luo<sup>1</sup>

<sup>1</sup>School of Applied Science, Harbin University of Science and Technology, Harbin 150080, China

<sup>2</sup>College of Computer Science and Engineering, Dalian Nationalities University, 18 Liaohe West Road, Dalian Development Zone, Dalian 116600, China

<sup>3</sup>Faculty of Electronic Information and Electrical Engineering, Dalian University of Technology, Dalian 116023, China

<sup>4</sup>Faculty of Engineering, Mudanjiang Normal College, Mudanjiang 157012, China

Correspondence should be addressed to Hai Guo; guohai@dlnu.edu.cn

Received 8 April 2015; Accepted 31 May 2015

Academic Editor: Mircea Chipara

Copyright © 2015 Hai Guo et al. This is an open access article distributed under the Creative Commons Attribution License, which permits unrestricted use, distribution, and reproduction in any medium, provided the original work is properly cited.

Using the method of Stochastic Gradient Boosting, ten SMO-SVR are constructed into a strong prediction model (SGBS model) that is efficient in predicting the breakdown field strength. Adopting the method of in situ polymerization, thirty-two samples of nanocomposite films with different percentage compositions, components, and thicknesses are prepared. Then, the breakdown field strength is tested by using voltage test equipment. From the test results, the correlation coefficient (CC), the mean absolute error (MAE), the root mean squared error (RMSE), the relative absolute error (RAE), and the root relative squared error (RRSE) are 0.9664, 14.2598, 19.684, 22.26%, and 25.01% with SGBS model. The result indicates that the predicted values fit well with the measured ones. Comparisons between models such as linear regression, BP, GRNN, SVR, and SMO-SVR have also been made under the same conditions. They show that CC of the SGBS model is higher than those of other models. Nevertheless, the MAE, RMSE, RAE, and RRSE of the SGBS model are lower than those of other models. This demonstrates that the SGBS model is better than other models in predicting the breakdown field strength of polyimide nanocomposite films.

## 1. Introduction

As one of material products that have been developed for a long time, polyimide film (PI film) has been mainly applied in high and new technology industries such as aerospace, machinery, electrical and electronics engineering, optical communication, LCD, automobile, precision instrument, gas separation, and microelectronics [1]. With the development of nanotechnology, nanoparticles of different sizes, percentage compositions, and components have been mixed with PI by more and more researchers to produce high-quality polyimide nanocomposite films [2, 3].

Breakdown field strength is an important characteristic parameter to characterize polyimide nanocomposite films. It can be calculated by (breakdown voltage)/(film thickness). Many researchers have already made studies and analysis on the breakdown field strength of nanocomposite films [4–6].

There are many factors that can impact the breakdown field strength, including the type of nanoparticle, dielectric constant, electric conductivity, coefficient of thermal conductivity, composition, nanoparticles' size and specific area, and composite film thickness. In order to establish the knowledge base for the material property regarding breakdown field strength of polyimide nanocomposite films, large quantities of experiments have to be prepared and measure related characteristics. Nevertheless, it is also well known that getting properties data is very costly in terms of time and materials. It is for this reason that developing a fast and efficiency method to predict the breakdown field strength of polyimide nanocomposite films is very much in demand.

Intelligent computing and neuronal network have been widely applied in performance prediction, identification, and optimization of nanocomposite films. Yang et al. used a generalized regression neural network (GRNN) to predict

the friction coefficient of  $\text{Cr}_{1-x}\text{Al}_x\text{C}$  film [7]. Cho et al. optimized the characteristics of ITO/Al/ITO multilayer films by advantages of neural network and genetic algorithm [8]. Bahramian made use of an artificial neural network to predict the growth rate of  $\text{TiO}_2$  nanostructured film [9]. Ensemble learning has now become a new hotspot of intelligent computing [10–13]. By using ensemble, several weak classifiers can be constructed into a strong classifier. Some common methods of ensemble learning include boosting, bagging, and stacking. Boosting [14] keeps upgrading weights during data extraction and revises the weights of data set that have been classified wrong. In the end, several weak classifiers are obtained and can be constructed into a strong classifier. Bagging [15] is used the reiterative training to get several classifiers based on a training set. Stacking [16] contains two layers. In the first layer, different algorithms are employed to generate several weak classifiers. At the same time, a new data set with the same size of the original data set is also generated. Then, the new data set together with a new algorithm can be used to construct the classifier of the second layer.

The purpose of this paper is to develop a Stochastic Gradient Boosting + SMO-SVR model (SGBS model) to predict the breakdown field strength of polyimide nanocomposite films. In what follows, film preparation and prediction model are introduced first. The experimental details for sputtering systems and materials are described next. Then, the experimental results are described and the establishment of SGBS model with 10-fold cross validation results is carried out. Comparison experiments between linear regression, BP neural network (BP), general regression neural network (GRNN), SVR (support vector regression), and SMO-SVR models are conducted.

## 2. Nanocomposite Film Preparation and Prediction Model

**2.1. Preparation of Nanocomposite Films.** The method of in situ polymerization is used to prepare the polyimide matrix inorganic nanocomposite film. Experimental materials include 4,4'-diaminodiphenyl ether (ODA), pyromellitic dianhydride (PMDA), dimethylacetamide (DMAc),  $\text{Al}_2\text{O}_3$ , rutile  $\text{TiO}_2$ ,  $\text{BaTiO}_3$ ,  $\text{SiO}_2$ , and ethanol. The detailed purchase information of the above experimental materials is shown in Table 1. Firstly, put PMDA into the solution of ODA in DMAc to produce an amount of polyamide acid of certain viscosity. Secondly, add in different nanoparticles. Finally, let the mixture go through paving membrane heat treatment and imidization transform.

To verify our SGBS model, we have designed and prepared in this paper nanoparticle samples with different types, sizes, ratios, and thicknesses. The SEM image of surface appearance of pure PI is given in Figure 1(a). The surface of film is smooth and its tightness is well. Figure 1(b) shows the SEM image of surface appearance of PI/ $\text{BaTiO}_3$  composite film doped with content of 60 wt%. There are large amounts of  $\text{BaTiO}_3$  nanoparticles exposing on the surface of film with the size from 100 nm to 300 nm. Comparing with the other films, the surface appearance of film has been changed to be

TABLE 1: The detailed purchase information of experimental materials.

Material	Companies
4,4'-Diaminodiphenyl ether	Sinopharm Chemical Reagent Co., Ltd.
Pyromellitic dianhydride	Sinopharm Chemical Reagent Co., Ltd.
Dimethylacetamide	Tianjin Fuyu Fine Chemical Co., Ltd.
$\text{Al}_2\text{O}_3$	Beijing DK Nano Technology Co., Ltd.
Rutile $\text{TiO}_2$	Beijing DK Nano Technology Co., Ltd.
$\text{BaTiO}_3$	Beijing DK Nano Technology Co., Ltd.
$\text{SiO}_2$	Beijing DK Nano Technology Co., Ltd.
Ethanol	Tianjin Fuyu Fine Chemical Co., Ltd.

rough due to the dopant of  $\text{BaTiO}_3$  nanoparticles. Its density has also been decreased. Figure 1(c) shows the SEM image of surface appearance of PI/ $\text{TiO}_2$  composite film doped with content of 5 wt%.  $\text{TiO}_2$  can absorb ultraviolet ray to change the color of film into brown. The surface appearance of film is smooth compared with pure PI film. Figure 1(d) shows the SEM image of surface appearance of PI/ $\text{Al}_2\text{O}_3$  composite film doped with content of 20 wt%. There are some nanoparticles appearing in the surface of film, uniformly, where the diameter of nanoparticles is observed to be 70 nm and some particles are not cluster. In conclusion, the prepared hybrid PI particles are evenly distributed.

**2.2. Standard SMO-SVR Model.** SVM (support vector machine) [17] is one of the most typical machine learning methods in field of statistical learning theory. It has a very good learning ability in a small sampling space. Compared with BP, GRNN, and other neural networks, it has advantages such as structural risk minimization, global optimization solution, high dimensional space, and being linearly separable. It has been widely used for recognitions and regressions.

The core of support vector regression (SVR) is to find out a hyperplane, namely, to a minimized linear function with inequality constraints, giving a training sample

$$S = (x_1, y_1), \dots, (x_n, y_n), \quad (1)$$

where  $x$  means input and  $y$  means output. The training sample needs to be turned into a linearly separable problem when it is a linear inseparability. Generally, the sample space can be mapped from a low-dimensional space into a high dimensional space by using a kernel function. The nonlinear regression function (estimation) is

$$f(x) = \omega\varphi(x) + b, \quad (2)$$

where  $b$  is a threshold,  $\omega$  is a weight, and  $\varphi(x)$  is the nonlinear mapping function. The loss function is shown as follows:

$$c(x, y, f) = |y - f(x)|_\varepsilon. \quad (3)$$

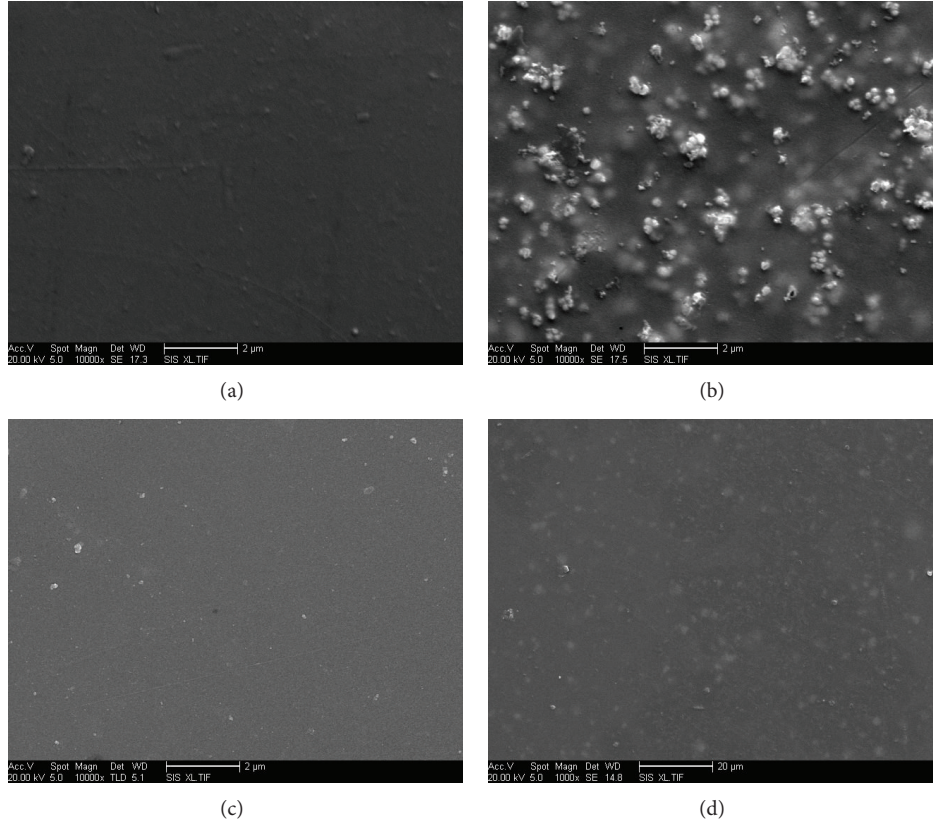


FIGURE 1: SEM image of the nanocomposite film. (a) The SEM image of pure PI film; (b) the SEM image of surface appearance of PI/BaTiO<sub>3</sub> composite film doped with content of 60 wt%; (c) the SEM image of surface appearance of PI/TiO<sub>2</sub> composite film doped with content of 5 wt%; (d) the SEM image of surface appearance of PI/Al<sub>2</sub>O<sub>3</sub> composite film doped with content of 20 wt%.

By importing a Lagrange multiplier, the minimization of the objective function can be expressed as

$$\begin{aligned}
 \min \quad & \frac{1}{2} \|\omega\|^2 + C \sum_{i=1}^n (\xi_i + \xi'_i) \\
 \text{subject to} \quad & y_i - \omega\varphi(x_i) - b \leq \varepsilon + \xi_i \\
 & \omega\varphi(x_i) + b - y_i \leq \varepsilon + \xi'_i \\
 & \xi_i, \xi'_i \geq 0, \quad i = 1, 2, \dots, n.
 \end{aligned} \quad (4)$$

Transform (4) into a dual problem, and we get

$$\begin{aligned}
 \max \quad & \left[ -\frac{1}{2} \sum_{i,j}^n (a_i^* - a_i) (a_j^* - a_j) K(x_i, x_j) \right. \\
 & \left. - \varepsilon \sum_{i=1}^n (a_i^* + a_i) + \sum_{i=1}^n y_i (a_i - a_i^*) \right],
 \end{aligned} \quad (5)$$

where  $C$  is a penalty factor and  $a_i^*$  and  $a_i$  are Lagrangians; then the regression function is

$$f(x) = \sum_{i=1}^N (a_i - a_i^*) K(x_i, x_j) + b, \quad (6)$$

where  $N$  is the number of support vectors in (6) [18]. In this paper, a normalized polynomial kernel has been taken as the kernel function.

John Platt, from Microsoft Research, proposed the SMO (sequential minimal optimization) algorithm in order to shorten the training time of support vector regression in 1998 [19]. SMO can optimize the  $\alpha$  value of two samples at one time. Through the loop iteration with a given times  $M$ , the  $\alpha$  value of all samples can be optimized, as shown in Figure 2. For the data in Table 2, the method of 10-fold cross validation is used to make the model training on the standard SVR and SMO-SVR. The time of modeling SVR and SMO-SVR is 0.26 s and 0.03 s, respectively. SMO can promote the training efficiency of support vector regression while reducing the training time of the model.

*2.3. Promoting the Model by Stochastic Gradient Boosting.* Boosting [20], as one of the most important ensemble learning methods, is to obtain a predictive function by construction and ensemble of a series of predictive functions. The core idea of gradient boosting, proposed by Friedman [21], is to construct an ensemble learning machine by calculating a loss function and letting the function descend along its gradient. In other words, it is to calculate the loss function of previous model, so as to build a new model along the descending gradient direction of the loss function. Eventually, a regression

TABLE 2: Data of breakdown field strengths of nanocomposite films.

Samples	Input								Output
	Type of nanoparticles	Dielectric constant	Thickness of films ( $\mu\text{m}$ )	Thermal conductivity ( $\text{W}/\text{cm}\cdot\text{k}$ )	Electrical resistivity ( $\Omega\cdot\text{m}$ )	Ratio of nanoparticles (wt%)	Size of nanoparticles (nm)	Specific area of nanoparticles ( $\text{m}^2/\text{g}$ )	Breakdown field strength of the hybrid PI (kV/mm)
1	BaTiO <sub>3</sub>	1400	25	0.50	$1 \times 10^5$	10	100	12	157
2	BaTiO <sub>3</sub>	1400	25	0.50	$1 \times 10^5$	15	100	12	137
3	BaTiO <sub>3</sub>	1400	25	0.50	$1 \times 10^5$	20	100	12	125
4	BaTiO <sub>3</sub>	1400	25	0.50	$1 \times 10^5$	25	100	12	119
5	BaTiO <sub>3</sub>	1400	25	0.50	$1 \times 10^5$	30	100	12	105
6	BaTiO <sub>3</sub>	1400	25	0.50	$1 \times 10^5$	50	100	12	72
7	BaTiO <sub>3</sub>	1400	25	0.50	$1 \times 10^5$	60	100	12	54
8	BaTiO <sub>3</sub>	1400	25	0.50	$1 \times 10^5$	70	100	12	41
9	Rutile TiO <sub>2</sub>	100	25	0.40	$9 \times 10^7$	0	35	70	230
10	Rutile TiO <sub>2</sub>	100	25	0.63	$9 \times 10^7$	1	35	70	240
11	Rutile TiO <sub>2</sub>	100	25	0.63	$9 \times 10^7$	3	35	70	210
12	Rutile TiO <sub>2</sub>	100	25	0.63	$9 \times 10^7$	4	35	70	177
13	Rutile TiO <sub>2</sub>	100	25	0.63	$9 \times 10^7$	5	35	70	170
14	Rutile TiO <sub>2</sub>	100	25	0.63	$9 \times 10^7$	7	35	70	160
15	SiO <sub>2</sub>	1.56	25	160	$1 \times 10^{16}$	5	40	300	313
16	SiO <sub>2</sub>	1.56	25	160	$1 \times 10^{16}$	10	40	300	307
17	SiO <sub>2</sub>	1.56	25	160	$1 \times 10^{16}$	15	40	300	327
18	SiO <sub>2</sub>	1.56	25	160	$1 \times 10^{16}$	20	40	300	252
19	SiO <sub>2</sub>	1.56	25	160	$1 \times 10^{16}$	25	40	300	240
20	$\alpha\text{Al}_2\text{O}_3$	10	30	4.10	$1 \times 10^{14}$	4	30	25	275
21	$\alpha\text{Al}_2\text{O}_3$	10	30	4.10	$1 \times 10^{14}$	8	30	25	263
22	$\alpha\text{Al}_2\text{O}_3$	10	30	4.10	$1 \times 10^{14}$	12	30	25	234
23	$\alpha\text{Al}_2\text{O}_3$	10	30	4.10	$1 \times 10^{14}$	16	30	25	212
24	$\alpha\text{Al}_2\text{O}_3$	10	30	4.10	$1 \times 10^{14}$	20	30	25	235
25	$\alpha\text{Al}_2\text{O}_3$	10	30	4.10	$1 \times 10^{14}$	24	30	25	203
26	Al <sub>2</sub> O <sub>3</sub>	8	30	29.31	$1 \times 10^{14}$	15	13	100	190
27	Al <sub>2</sub> O <sub>3</sub>	8	30	29.31	$1 \times 10^{14}$	20	13	100	189
28	Al <sub>2</sub> O <sub>3</sub>	8	30	29.31	$1 \times 10^{14}$	25	13	100	178
29	SiO <sub>2</sub>	1.56	30	160	$1 \times 10^{16}$	10	7	350	307
30	SiO <sub>2</sub>	1.56	30	160	$1 \times 10^{16}$	15	7	350	327
31	SiO <sub>2</sub>	1.56	30	160	$1 \times 10^{16}$	20	7	350	252
32	SiO <sub>2</sub>	1.56	30	160	$1 \times 10^{16}$	25	7	350	240

model can be generated through  $N$  times of iterations. In this paper, we use the Stochastic Gradient Boosting to turn ten SMO-SVR models into a strong predictive model (SGBS model). The algorithmic steps of the SGBS model are shown as follows:

- (1)  $\{X, Y\}$  is a data sample of breakdown field strengths of different nanocomposite thin films, in which  $X = (x_1, x_2, \dots, x_n)$  is input and  $Y = (y_1, y_2, \dots, y_n)$  is output. The loss function is  $L(y_i, F(x_i))$ ,  $i \in \{1, 2, \dots, n\}$ , and the prediction model of SMO-SVR is  $h(X)$ .

- (2) Initialize the model

$$F_0(x) = \arg \min_{\beta} \sum_{i=1}^N L(y_i, \beta). \quad (7)$$

- (3) Calculate the upper limit ( $M$ ) of iterations by cross validation.

- (4) Calculate the gradient direction

$$\tilde{y}_i = - \left[ \frac{\partial L(y_i, F(x_i))}{\partial F(x_i)} \right]_{F(x)=F_{m-1}(x)}, \quad i = 1, \dots, N. \quad (8)$$

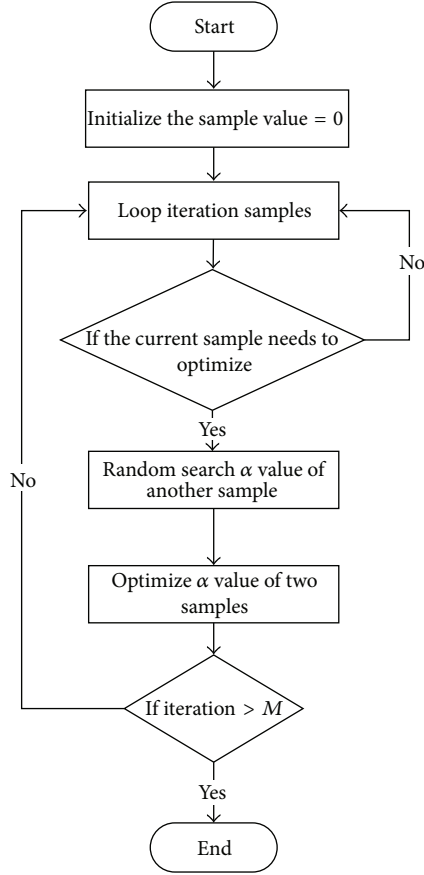


FIGURE 2: Flowchart of the SMO optimization algorithm.

(5) Fit the SMO-SVR by using least squares to obtain the fitting model  $h(x_i, \alpha_m)$ .

(6) Figure out new step length based on the loss function

$$\beta_m = \arg \min \sum_{i=1}^N L(y_i, F_{m-1}(x_i)) + \beta h(x_i, \alpha_m). \quad (9)$$

(7) Generate a new model

$$F_m(x) = F_{m-1}(x) + \beta_m h(x, \alpha_m). \quad (10)$$

(8) Stochastically extract  $f\%$  of the training sample to fit the SMO-SVR during every time of iteration; then we can get the SGBS model after  $M$  times of iterations:

$$F(x) = \sum_{m=1}^M \beta_m h(x, \alpha_m). \quad (11)$$

### 3. Experiment and Result Analysis

**3.1. Construction of the Experimental Sample.** Test the breakdown field strength by using a withstanding voltage tester (type: CS2674C). Voltage range is 0–50 kV; test error is  $\pm 5\%$ ; leakage current measurement range is 0.5–20 mA; measurement error is  $\pm 5\%$ . Take polymethylphenylsiloxane fluid with

high insulation strength (which can be up to 16 kV/mm) as the medium, with the rate of voltage rise of 500 V/s. Test the breakdown field strength of the nanocomposite films prepared in Section 2.1. Select 20 samples as a group for testing each hybrid PI, and take the mean value of the 10 middle breakdown field strengths as the breakdown field strength of the group. Then, calculate the standard deviation. After the experiment we get the data of breakdown field strengths as shown in Table 2. The input  $X$  includes type ( $X_1$ ), doping ratio ( $X_2$ ), electrical resistivity ( $X_3$ ), dielectric constant ( $X_4$ ), thermal conductivity ( $X_5$ ), size ( $X_6$ ), and specific area ( $X_7$ ) of nanoparticles and thickness of the film ( $X_8$ ). The output  $Y$  is the breakdown field strength of the hybrid PI.

#### 3.2. Evaluation Indicators of the Prediction Performance.

There are many indicators for evaluating the prediction performance, such as MAPE (mean absolute percentage error), MAE (mean absolute error), RMSE (root mean squared error), CC (correlation coefficient), RAE (relative absolute error), and RRSE (root relative squared error). In this paper, CC, MSE, RMSE, RSE, and RRSE are taken as evaluation indicators.

CC (correlation coefficient) represents the relevancy of the linear regression relationship between  $f_i$  (independent variable) and  $y_i$  (response variable) of the model. It is a coefficient of a simple linear correlation between  $y_i$  and its estimated values. CC is larger than zero and ranges from 0 to 1. A larger CC means a more relevant linear regression relationship.

MSE (mean absolute error) is to judge the different degree between predicted values and real ones. It is inversely proportional to prediction accuracy. A smaller MSE means a better effect the predictor can be with. It can be expressed as

$$\text{MAE} = \frac{1}{n} \sum_{i=1}^n |f_i - y_i| = \frac{1}{n} \sum_{i=1}^n |e_i|, \quad (12)$$

where  $f_i$  represents predicted values and  $y_i$  represents real values.

RMSE (root mean squared error) is the square root of the ratio of the quadratic sum of deviations between predicted values and real values to the times ( $n$ ) of predictions. It is sensitive to maximum or minimal errors of a group of predicted values and therefore can well reflect prediction accuracy. RMSE is inversely proportional to the prediction accuracy. The smaller the RMSE is, the more accurate the predictor can be. It can be expressed as follows:

$$\text{RMSE} = \sqrt{\frac{\sum_{i=1}^n (f_i - y_i)^2}{n}}. \quad (13)$$

RSE (relative absolute error) is the different degree between the absolute deviation obtained from the prediction model and the absolute deviation obtained by directly speculating the training sample. It is inversely proportional to

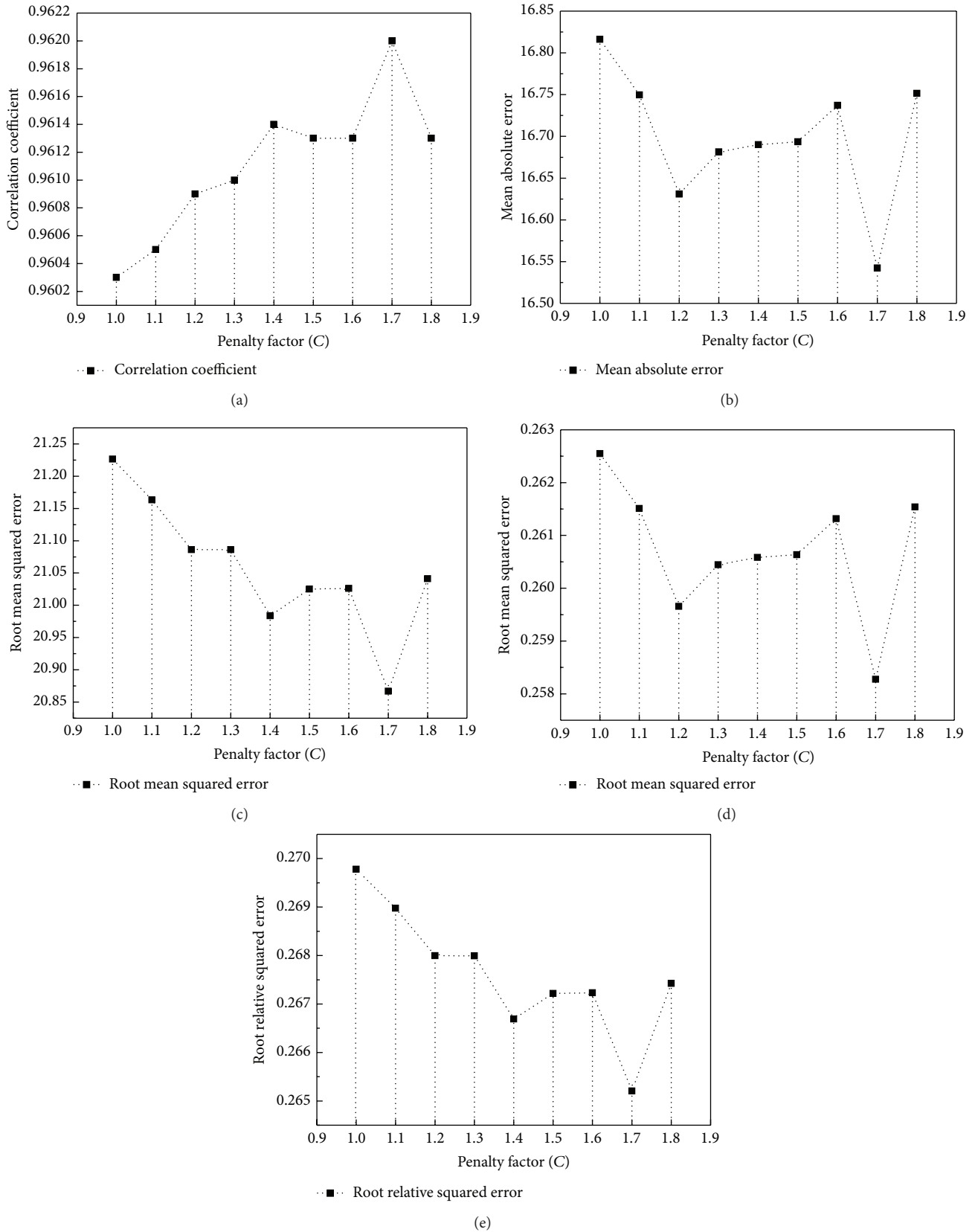
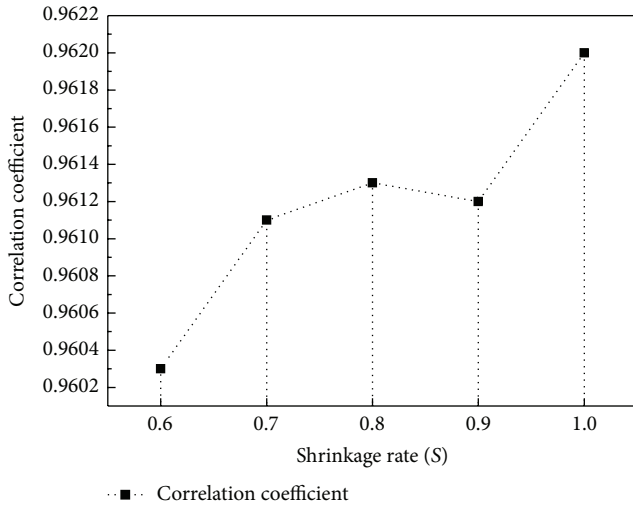
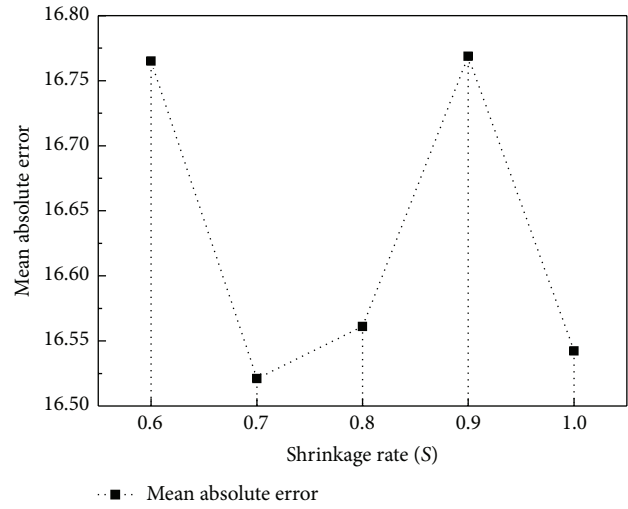


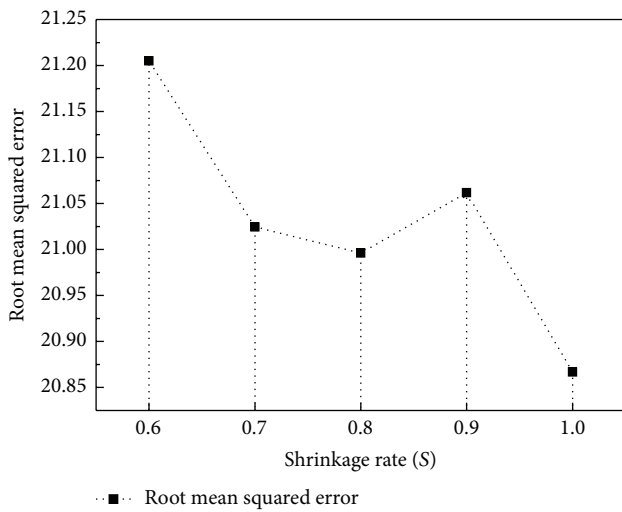
FIGURE 3: The impacts of variation of penalty factor (C) on prediction performance. (a) The correlation coefficient with different penalty factors (C); (b) the mean absolute error with different penalty factors (C); (c) the mean absolute error with different penalty factors (C); (d) the root mean squared error with different penalty factors (C); (e) the root relative squared error with different penalty factor (C).



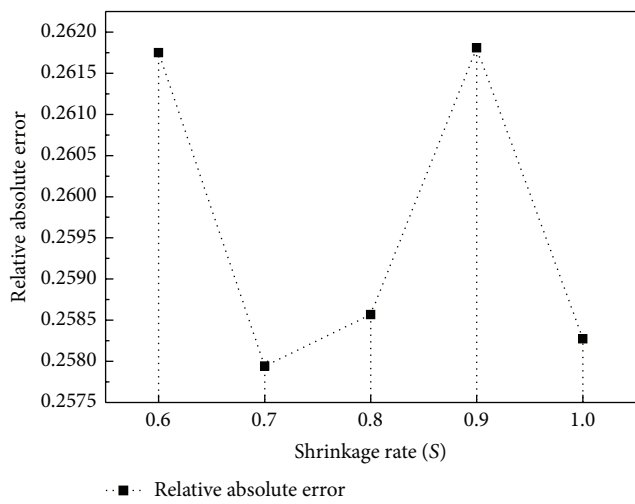
(a)



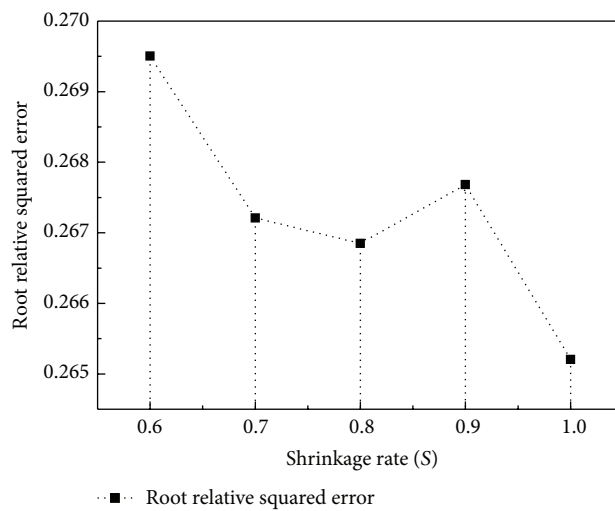
(b)



(c)



(d)



(e)

FIGURE 4: Impact of  $S$  on prediction performance. (a) Correlation coefficient relative to shrinkage rate ( $S$ ) of training samples; (b) mean absolute error relative to shrinkage rate ( $S$ ) of training samples; (c) root mean squared error relative to shrinkage rate ( $S$ ) of training samples; (d) relative absolute error relative to shrinkage rate ( $S$ ) of training samples; (e) root relative squared error relative to shrinkage rate ( $S$ ) of training samples.

TABLE 3: Comparison on prediction performances of three kernel functions.

Indicators	Normalized polynomial	Polynomial	RBF
Correlation coefficient	0.9603	0.9236	0.8901
Mean absolute error	16.8162	23.5927	29.6448
Root mean squared error	21.2266	29.2044	34.7791
Relative absolute error	26.255%	36.8351%	46.2842%
Root relative squared error	26.9779%	37.1173%	44.2024%

prediction accuracy. The smaller the RSE is, the higher the prediction accuracy can be:

$$\text{RSE} = \frac{\sum_{i=1}^n |f_i - y_i|}{\sum_{i=1}^n |\bar{f}_i - y_i|}. \quad (14)$$

RRSE (root relative squared error) can be calculated as follows:

$$\text{RRSE} = \frac{\sum_{i=1}^n |f_i - y_i|^2}{\sum_{i=1}^n |\bar{f}_i - y_i|^2}. \quad (15)$$

RRSE is also inversely proportional to prediction accuracy. The smaller the RRSE is, the higher the prediction accuracy can be [22].

**3.3. Experimental Results and Analysis.** To verify the SGBS prediction model, the type, dielectric constant, electrical resistivity, thermal conductivity, size and specific area of nanoparticles, and the thickness of films in Table 2 are taken as the input  $X$ , and the breakdown field strength of hybrid PI is taken as the output  $Y$ . In this paper, we use Macbook Pro (CPU: Intel I7-2640 M; memory: 16G) as the hardware for experiments and use Matlab 2012a to program prediction model.

*Experiment 1.* Use the method of 10-fold cross validation to fit the data in Table 2. Main parameters of the SGBS model include kernel function,  $C$  and  $S$ , of which  $C$  is the penalty factor of SMO-SVR and  $S$  is the extracting ratio when training the sample. First of all, normalize the sample data. Three kernel functions—normalized polynomial kernel, polynomial kernel, and RBF kernel—are employed to test the sample. The results are listed in Table 3. From the table we know that the normalized polynomial kernel has the highest correlation coefficient but lowest mean absolute error, root mean squared error, relative absolute error, and root relative squared error. Therefore, we choose it as the kernel function for the SGBS model.

For optimization function, the penalty factor of outliers is selected by experience as well as by experiments. Figure 3 shows the comparison on prediction performances of SGBS model when  $C$  varies from 1 to 1.8. Figure 3(a) demonstrates that the correlation coefficient reaches its peak values when  $C = 1.6, 1.7, \text{ and } 1.8$ , which are chosen as the value of  $C$ , for

correlation coefficient is proportional to prediction accuracy. By analyzing Figures 3(b) and 3(d) we know that the mean absolute error and relative absolute error reach their minimal values when  $C = 1.7$ , only larger than the values when  $C = 1.6$  and  $1.8$ . Therefore, they reach optimal performance when  $C = 1.7$ , for mean absolute error and relative absolute error are inversely proportional to prediction accuracy.

By analyzing Figures 3(c) and 3(d) we know that the smallest root mean squared error and root relative squared error appear at  $C = 1.6$ , followed by  $C = 1.7$  and  $C = 1.8$ . Based on the above analysis, this paper takes  $C = 1.7$  as the optimum value.

$S$  is the specify shrinkage rate in Stochastic Gradient Boosting, namely, the proportion of the stochastically extracted training sample. Figure 4 shows the impact of variation of  $S$  on prediction performance when  $C = 1.7$ . When  $S = 1$ , correlation coefficient reaches its peak value, and the prediction attains the best performance as shown in Figure 4(a). By analyzing Figures 4(b)–4(e) we know that when  $S = 1$ , mean absolute error, root mean squared error, relative absolute error, and root relative squared error reach their minimal values, signifying the best prediction performance.

According to the above analysis we know that when  $C = 1.7$  and  $S = 1$  are taken as the optimum values of the SGBS model, the prediction performance is the best. Figure 5 shows the degree of fitting between predicted values and real ones. Figure 6 shows the absolute error ratio of prediction. The tables and figures demonstrate that the error ratios of sample 8 (70 wt%, 100 nm, BaTiO<sub>3</sub>), sample 17 (15 wt%, 40 nm, SiO<sub>2</sub>), and sample 30 (15 wt%, 7 nm, SiO<sub>2</sub>) are all larger than 15%, indicating an ordinary fitting, while the error ratios of other samples are less than 15%, indicating a better fitting. For all the six multicomponent TiO<sub>2</sub> film samples with the thickness of 35 μm, the prediction errors are not larger than 15%. For the eight BaTiO<sub>3</sub> film samples, there is one sample of which the prediction errors are larger than 15%. For all the nine multicomponent Al<sub>2</sub>O<sub>3</sub> film samples, the prediction errors are not larger than 15%, while for the nine multicomponent SiO<sub>2</sub> film samples, there are also two samples of which the prediction errors are larger than 15 wt%. In this model, the prediction performance of the multicomponent Al<sub>2</sub>O<sub>3</sub> and rutile TiO<sub>2</sub> with different thicknesses is better than that of the BaTiO<sub>3</sub> and SiO<sub>2</sub> film samples. For the thirty-two nanocomposite films with different components, mixtures, and thicknesses, there are twenty-nine film samples of which the prediction errors are lower than 15%, proving that the model is of practical value in actual engineering works.

*Experiment 2.* In order to further verify the SGBS model, it needs to be compared to other models, namely, the linear regression, BP neural network, GRNN neural network, SVR (support vector regression), and SMO-SVR, under the same conditions. Comparison results of the prediction performance of these models are shown in Table 4. The correlation coefficient of SGBS model is 0.962, larger than that of the models of linear regression [23], BP neural network [24], GRNN neural network [7], SMO-SVR [25], and SVR [26], proving that the linear regression relationship of the SGBS model is better than that of the other five models. In the SGBS

TABLE 4: Comparisons of models' prediction performance.

Indicators	SGBS	Linear regression	BP	GRNN	SVR	SMO-SVR
CC	0.962	0.9438	0.960	0.957	0.459	0.917
RMSE	20.866	25.235	21.350	21.932	79.662	30.401
RRSE	26.520%	32.072%	27.135%	27.874%	101.246%	38.639%

TABLE 5: The comparison of the predicted and tested values of breakdown field strength.

Measured value [27] (kV/mm)	Predicted value (kV/mm)	MAE	RMSE	RAE (%)	RRSE (%)	Error ratio (%)
233	225.9667	7.0334	7.0334	24.5976	24.5976	3.0185

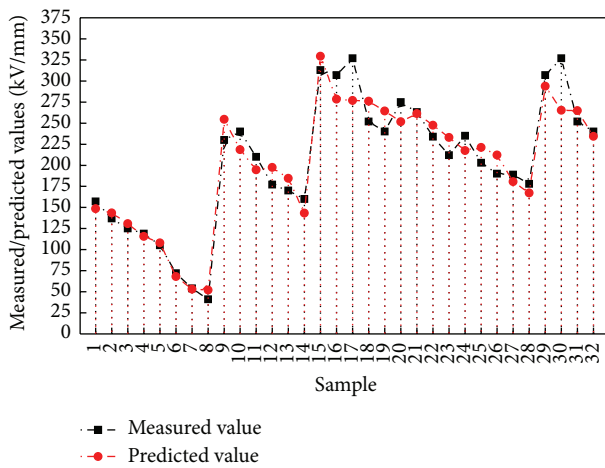


FIGURE 5: Comparison between real values and predicted values of the SGBS mode.

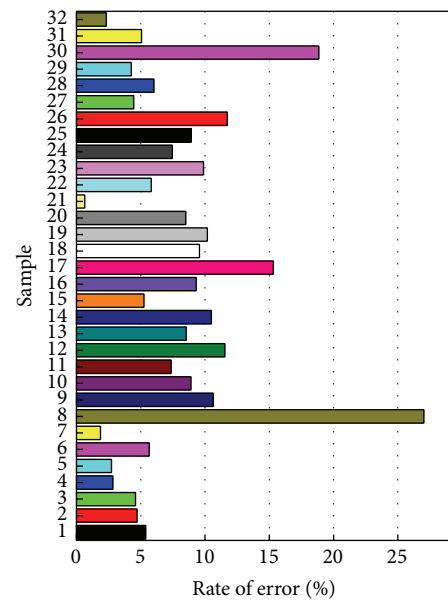


FIGURE 6: Analysis on sample errors.

model, the root mean squared error and root mean squared error are 20.8668 and 26.520%, respectively, lower than those of the other models, certifying its better prediction performance.

*Experiment 3.* In order to validate the generosity of the model, the actual measurement results conducted by Shi et al. in [27] are chosen to do the prediction. In this preference, the particle size is  $30\ \mu\text{m}$ , and the doping ratio is 2 wt% with PI/nano- $\text{Al}_2\text{O}_3$  composite films. The thickness of film is  $30\ \mu\text{m}$ . Its breakdown field strength is 233 kV/mm. Adopting the samples in Table 2 as the training set of SGBS model. For the parameters of the model,  $C = 1.7$ ,  $S = 1$ . Using the 2 wt%-PI/nano- $\text{Al}_2\text{O}_3$  composite films in [27] as testing sample, the results could be obtained as shown in Table 5. For the test result of breakdown field strength that is 233 kV/mm, its prediction value is 225.9667 kV/mm by SGBS model. The error ratio is 3.0185%. The MAE, RMSE, RAE, and RRSE are 7.0334, 7.0334, 24.5976, and 24.5976. The prediction and actual data are in good agreement. This method could predict the PI/nano- $\text{Al}_2\text{O}_3$  composite films effectively.

## 4. Conclusions

This paper presents an ensemble learning method for predicting breakdown field strength of polyimide nanocomposite films. By using the method of Stochastic Gradient Boosting, ten SMO-SVR prediction models are constructed into a strong prediction model (SGBS model) that is efficient in predicting the breakdown field strength. Through analyzing the experiment data we obtain following conclusions:

- (1) In prediction of thirty-two nanocomposite films of different components, particles, and thicknesses ( $25\text{--}30\ \mu\text{m}$ ) by using the method of 10-fold cross validation, there are twenty-nine samples of which the prediction errors are lower than 15%, proving that the SGBS model is efficient in predicting the breakdown field strength of polyimide nanocomposite films.
- (2) Comparisons show that the SGBS model has a larger correlation coefficient than that of linear regression, BP, GRNN, SVR, and SMO-SVR models but smaller

root mean squared error and root relative squared error. Hence, prediction performance of the SGBS model is better than that of the other five models.

- (3) The SGBS model shows a better prediction on  $\text{Al}_2\text{O}_3$  and rutile  $\text{TiO}_2$  films than on  $\text{BaTiO}_3$  and  $\text{SiO}_2$  films.

Next, some other ensemble learning methods will be employed to predict the corona resistance, dielectric constant, dielectric constant, and thermal properties of polyimide nanocomposite films.

## Conflict of Interests

The authors declare that there is no conflict of interests regarding the publication of this paper.

## Acknowledgments

This paper has obtained the support of the National Natural Science Foundation of China (51077028, 51307046, and 60803096) and Heilongjiang Natural Science Foundation of China (A201006), National Basic Research Program of China (2012CB723308), Fund of the State Ethnic Affairs Commission of China, and the Fundamental Research Funds for the Central Universities. Authors also gratefully acknowledge the helpful comments and suggestions of the reviewers who improved the presentation.

## References

- [1] W. J. Lee and Y. B. Kim, "Adhesion and interfacial characteristics of metal/PI composite film modified by  $\text{O}_2$  ion beam," *Thin Solid Films*, vol. 517, no. 3, pp. 1191–1194, 2008.
- [2] N. An, H. Liu, Y. Ding, M. Zhang, and Y. Tang, "Preparation and electroactive properties of a PVDF/nano- $\text{TiO}_2$  composite film," *Applied Surface Science*, vol. 257, no. 9, pp. 3831–3835, 2011.
- [3] K. Sivudu, Y. Mahajan, and S. Joshi, "Nano-enabled tribological thin film coatings: global patent scenario," *Recent Patents on Nanotechnology*, vol. 8, no. 2, pp. 97–116, 2014.
- [4] Y. Song, Y. Shen, H. Liu, Y. Lin, M. Li, and C.-W. Nan, "Improving the dielectric constants and breakdown strength of polymer composites: effects of the shape of the  $\text{BaTiO}_3$  nano-inclusions, surface modification and polymer matrix," *Journal of Materials Chemistry*, vol. 22, no. 32, pp. 16491–16498, 2012.
- [5] L. Jiang, Y. Zhao, and J. Zhai, "A lotus-leaf-like superhydrophobic surface: a porous microsphere/nanofiber composite film prepared by electrohydrodynamics," *Angewandte Chemie*, vol. 43, no. 33, pp. 4338–4341, 2004.
- [6] Z. Zhou, M. Mackey, K. Yin et al., "Fracture phenomena in micro- and nano-layered polycarbonate/poly(vinylidene fluoride-co-hexafluoropropylene) films under electric field for high energy density capacitors," *Journal of Applied Polymer Science*, vol. 131, no. 4, Article ID 39877, 2014.
- [7] Y.-S. Yang, J.-H. Chou, W. Huang, T.-C. Fu, and G.-W. Li, "An artificial neural network for predicting the friction coefficient of deposited  $\text{Cr}_{1-x}\text{Al}_x\text{C}$  films," *Applied Soft Computing Journal*, vol. 13, no. 1, pp. 109–115, 2013.
- [8] E. N. Cho, P. Moon, C. E. Kim, and I. Yun, "Modeling and optimization of ITO/Al/ITO multilayer films characteristics using neural network and genetic algorithm," *Expert Systems with Applications*, vol. 39, no. 10, pp. 8885–8889, 2012.
- [9] A. Bahramian, "Study on growth rate of  $\text{TiO}_2$  nanostructured thin films: simulation by molecular dynamics approach and modeling by artificial neural network," *Surface and Interface Analysis*, vol. 45, no. 11, pp. 1727–1736, 2013.
- [10] G. Wang, J. Sun, J. Ma, K. Xu, and J. Gu, "Sentiment classification: the contribution of ensemble learning," *Decision Support Systems*, vol. 57, no. 1, pp. 77–93, 2014.
- [11] M. Claesen, F. De Smet, J. A. K. Suykens, and B. De Moor, "EnsembleSVM: a library for ensemble learning using support vector machines," *Journal of Machine Learning Research*, vol. 15, pp. 141–145, 2014.
- [12] N. Rooney, H. Wang, and P. S. Taylor, "An investigation into the application of ensemble learning for entailment classification," *Information Processing & Management*, vol. 50, no. 1, pp. 87–103, 2014.
- [13] K. P. Singh, S. Gupta, and D. Mohan, "Evaluating influences of seasonal variations and anthropogenic activities on alluvial groundwater hydrochemistry using ensemble learning approaches," *Journal of Hydrology*, vol. 511, pp. 254–266, 2014.
- [14] J. Xu, Q. Wu, J. Zhang, F. Shen, and Z. Tang, "Boosting separability in semisupervised learning for object classification," *IEEE Transactions on Circuits and Systems for Video Technology*, vol. 24, pp. 1197–1208, 2014.
- [15] F. Mordelet and J.-P. Vert, "A bagging SVM to learn from positive and unlabeled examples," *Pattern Recognition Letters*, vol. 37, no. 1, pp. 201–209, 2014.
- [16] T. P. Williams and J. Gong, "Predicting construction cost overruns using text mining, numerical data and ensemble classifiers," *Automation in Construction*, vol. 43, pp. 23–29, 2014.
- [17] C. Cortes and V. Vapnik, "Support-vector networks," *Machine Learning*, vol. 20, no. 3, pp. 273–297, 1995.
- [18] M. Maalouf, N. Khoury, J. G. Laguros, and H. Kumin, "Support vector regression to predict the performance of stabilized aggregate bases subject to wet-dry cycles," *International Journal for Numerical and Analytical Methods in Geomechanics*, vol. 36, no. 6, pp. 675–696, 2012.
- [19] C. J. C. Burge, "Sequential minimal optimization: a fast algorithm for training support vector machines," NeuroCOLT2 Technical Report Series NC2-TR-1998030, October 1998.
- [20] E. Bauer and R. Kohavi, "Empirical comparison of voting classification algorithms: bagging, boosting, and variants," *Machine Learning*, vol. 36, no. 1, pp. 105–139, 1999.
- [21] J. H. Friedman, "Greedy function approximation: a gradient boosting machine," *The Annals of Statistics*, vol. 29, no. 5, pp. 1189–1232, 2001.
- [22] T. E. Hoff, R. Perez, J. Kleissl, D. Renne, and J. Stein, "Reporting of irradiance modeling relative prediction errors," *Progress in Photovoltaics: Research and Applications*, vol. 21, no. 7, pp. 1514–1519, 2013.
- [23] P. Y. Lai and S. M. S. Lee, "Estimation of central shapes of error distributions in linear regression problems," *Annals of the Institute of Statistical Mathematics*, vol. 65, no. 1, pp. 105–124, 2013.
- [24] Y. Lou, W. Wu, and L. Li, "Inverse identification of the dynamic recrystallization parameters for  $\text{AZ}_{31}$  magnesium alloy using BP neural network," *Journal of Materials Engineering and Performance*, vol. 21, no. 7, pp. 1133–1140, 2012.

- [25] L. Dong, Z. Ren, and Q. Li, "Fault prediction for aircraft control surface damage based on SMO-SVR," *Journal of Beijing University of Aeronautics and Astronautics*, vol. 38, no. 10, pp. 1300–1305, 2012 (Chinese).
- [26] H. Guo, J. Yin, J. Zhao, Z. Huang, and Y. Pan, "Prediction of fatigue life of packaging EMC material based on RBF-SVM," *International Journal of Materials & Product Technology*, vol. 49, no. 1, pp. 5–17, 2014.
- [27] H. Shi, L. Liu, L. Weng, J. Ding, and W. Cui, "The effects of coupling agents on the properties of polyimide/nano- $\text{Al}_2\text{O}_3$  composite films," in *Proceedings of the 6th International Forum on Strategic Technology (IFOST '11)*, vol. 1, pp. 33–36, Harbin, China, August 2011.

## Research Article

# Improved Electrical Conductivity of Carbon/Polyvinyl Alcohol Electrospun Nanofibers

Nader Shehata,<sup>1,2</sup> Nabil Madi,<sup>3</sup> Mariam Al-Maadeed,<sup>3</sup>  
Ibrahim Hassounah,<sup>4</sup> and Abdullah Ashraf<sup>3</sup>

<sup>1</sup>Department of Engineering Mathematics and Physics, Faculty of Engineering, Alexandria University, Elhadara, Alexandria 21544, Egypt

<sup>2</sup>Center of Smart Nanotechnology and Photonics (CSNP), SmartCI Research Center, Alexandria University, Elhadara, Alexandria 21544, Egypt

<sup>3</sup>Center of Advanced Materials (CAM), Qatar University, Doha 2713, Qatar

<sup>4</sup>USTAR Bioinnovation Center, Utah State University, Logan, UT 84341, USA

Correspondence should be addressed to Nader Shehata; [nader83@vt.edu](mailto:nader83@vt.edu)

Received 6 June 2015; Revised 24 July 2015; Accepted 3 August 2015

Academic Editor: Mircea Chipara

Copyright © 2015 Nader Shehata et al. This is an open access article distributed under the Creative Commons Attribution License, which permits unrestricted use, distribution, and reproduction in any medium, provided the original work is properly cited.

Carbon nanofibers (CNFs) gained much interest in the last few years due to their promising electrical, chemical, and mechanical characteristics. This paper investigates a new nanocomposite composed of carbon nanofibers hosted by PVA and both are integrated in one electrospun nanofibers web. This technique shows a simple and cheap way to offer a host for CNFs using traditional deposition techniques. The results show that electrical conductivity of the formed nanofibers has been improved up to  $1.63 \times 10^{-4}$  S/cm for CNFs of weight 2%. The peak temperature of mass loss through TGA measurements has been reduced by 2.3%. SEM images show the homogeneity of the formed PVA and carbon nanofibers in one web, with stretched CNFs after the electrospinning process. The formed nanocomposite can be used in wide variety of applications including nanoelectronics and gas adsorption.

## 1. Introduction

Carbon fibers are of great technological and industrial interest because of their promising characteristics such as high strength to weight ratio, excellent chemical resistance, and superior electrical and thermal conductivity [1, 2]. They have been used to develop high performance fiber-reinforced composites, which are highly desirable in automotive, aerospace, and sport industries. Carbon nanofibers (CNFs) have high specific surface area, which resulted from pore-creating surface modification, which makes them suitable for gas adsorption and water treatment applications [3, 4]. Despite the extended research in carbon composites nanofibers, the present work introduces a new nanocomposite to generate carbon nanofibers embedded into polyvinyl alcohol (PVA) electrospun nanofibers. This novel research aims to offer a cheap and biodegradable host for already

synthesized carbon nanofibers instead of the deposition techniques such as sputtering or physical vapor deposition, which can impact the carbon nanofibers structure. The formed nanofibers should be highly conductive based on the superior conductivity of carbon nanofibers. The formed nanocomposites can be helpful in electronic devices, batteries, and super capacitors [5]. Electrospinning technique is selected as the fabrication method for the proposed nanocomposite because of the simplicity of operation, the feasibility to embed CNFs in the resulting PVA nanofibers, and the potential for scale-up to manufacture large volumes [6, 7]. In this process, high electric field strength is applied between a metallic needle and a metallic target. The strength of the electric field forces the polymer droplet at the needle tip to stretch and to deposit into fibers at the surface of the target [8–11]. The resulting webs can be feasible for many applications as in nanoagriculture, tissue engineering, and biomedical applications [12–16].

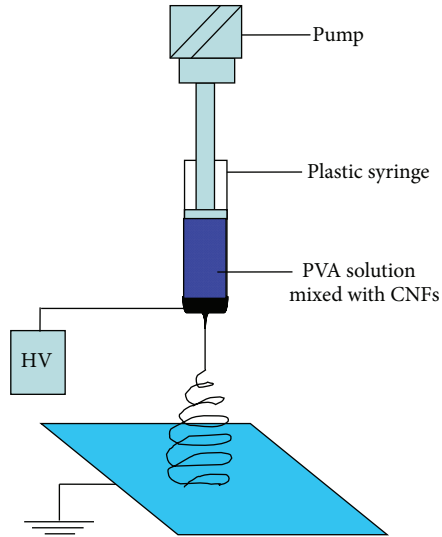


FIGURE 1: Schematic illustration of the setup of the electrospinning device.

## 2. Experimental Work

**2.1. Materials.** Carbon nanofibers from Sigma Aldrich, composed of graphitized (iron-free) conical platelets, have been used. In addition, polyvinyl alcohol (PVA) is used as the host material of electrospun nanofibers, with 88% degree of hydrolysis from Dupont, Taipei, Taiwan. Based on the authors' experimental work, PVA is dissolved in deionized water at concentrations 13 wt% for best electrospun nanofibers. In more detail, the chosen concentration is found to be optimal for producing electrospun mats with minimal visual defects such as pinholes or wet fleeces. Carbon nanofibers with different weight ratios (1 and 2 wt%) are added to the PVA solution and stirred at room temperature for two hours to form a homogeneous gel.

**2.2. Electrospinning.** The electrospinning setup, as shown in Figure 1, consists of a 10 mL plastic syringe with 18-gauge metallic needle, a single polarity, and variable high voltage (0–25 kV) power supply that is connected to the metallic target where the nanofibers can be formed. The distance between the needle tip and the target is held constant at 15 cm. The flow rate of the polymer solution, containing PVA/CNFs, supplied to the syringe is fixed at 0.7 mL/hr. The samples are collected on a flat metallic surface covered with aluminum foil. Each deposition of electrospun fibers is run for a total of 30 minutes with the result that a nonwoven fiber web coats the target.

**2.3. Characterization Methods.** The mean diameter of the electrospun nanofibers is measured by FEI Quanta 200 Environmental Scanning Electron Microscope (ESEM); 5 × 5 mm sections of nanofiber web were mounted on SEM holder. The conductivity of the electrospun nanofibers has been measured through 4-point probe station, in which Keithley 2400 voltameter measures the *I-V* characteristics of the formed nanocomposite. Therefore, circular nanofiber mat

sections were mounted on the SEM aluminum holder and fixed on a glass slide. SEM images of the webs' thickness, required for conductivity measurement, and the nanofibers are captured by ESEM and the thickness of the web has been measured. FTIR spectrum of the electrospun nanocomposite is measured by Infrared Spectrophotometer FTIR 760 (Thermo Nicolet).

Thermogravimetric analyses (TGA) of the electrospun composites have been done to observe the influence of carbon nanofibers on the degradation process of PVA. The electrospun nanofibers have been placed in an aluminum pan and heated from room temperature to 600°C at nitrogen atmosphere with the heating rate of 10°C/min. Differential Scanning Calorimetry (DSC) has been used to analyze the degree of crystallization using Perkin Elmer DSC 7.

## 3. Results and Discussions

Figures 2(a) and 2(b) show SEM images of both the pure electrospun PVA nanofibers and carbon nanofibers, respectively. It can be shown that the average diameter of the PVA electrospun nanofibers is 225 nm, while the average diameter of the carbon nanofibers is 130 nm.

Figures 3(a) and 3(b) show PVA nanofibers mixed with carbon nanofibers by 1 and 2%, respectively. SEM graphs in Figure 3 show that the produced nanofibers are homogeneous and there was no observable separation between PVA nanofibers and carbon nanofibers. The nanofiber diameters of the produced PVA/CNFs composite are approximately of the same ranges of the individual nanofibers shown in Figure 2. Furthermore, carbon nanofibers are hypothesized to be stretched in the formed nanocomposite from our observation of Figure 3(b) compared to CNFs original state as shown in Figure 2(b). That may be explained due to the high electric potential in the electrospinning experiment, which helps the carbon nanofibers to be stretched.

Figure 4 shows FTIR analysis of the formed nanocomposite of CNFs hosted by PVA electrospun nanofibers. It can be observed that the formed peaks belong to the PVA only with no more bonds formed with CNFs. The observed pattern is the same compared to pure PVA nanofibers and PVA with CNFs at different weight ratios of CNFs [17].

The electrical conductivity has been increased with increasing the carbon nanofibers in the PVA nanofibers. The electrical conductivity has been increased from  $1.01 \times 10^{-5}$  S/m (for pure PVA) to  $2.91 \times 10^{-5}$  S/m and  $16.36 \times 10^{-5}$  S/m (for PVA nanofibers with 1 wt% and 2 wt% carbon fibers' content, resp.). The increase of the electrical conductivity of PVA/carbon fiber mat is due to the high conductivity of carbon nanofibers [18].

Figure 5 shows the TGA analysis show of pure PVA and PVA doped with CNFs. The degradation of PVA which occurs at lower temperatures by addition of carbon fibers could be observed. The onset of the weight loss temperature was reduced from 300°C to 279°C (for PVA nanofibers and 2 wt% carbon fibers' content, resp.). The peak of first derivative of weight loss in Figure 6 is moved from 325°C to 318°C. The shifting of both the onset of weight loss and the first derivative

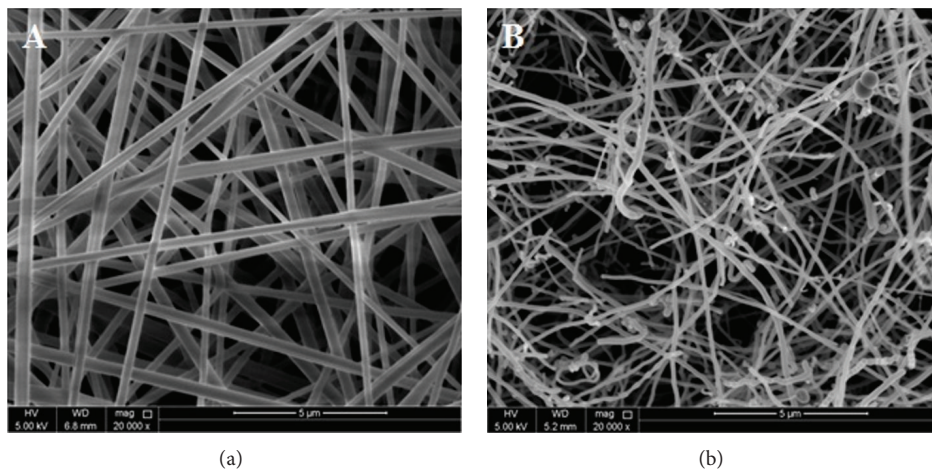


FIGURE 2: SEM images of (a) PVA nanofibers and (b) CNFs.

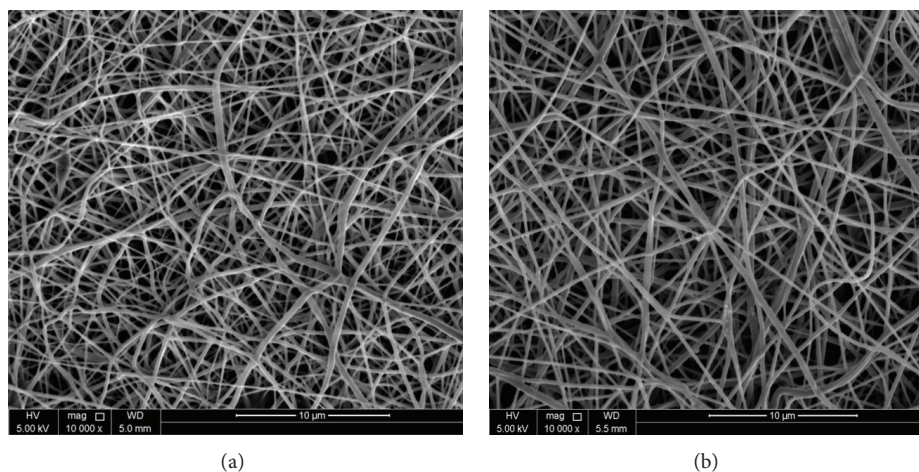


FIGURE 3: SEM images of electrospun nanofibers composed of PVA with (a) 1% wt CNFs and (b) 2% wt CNFs.

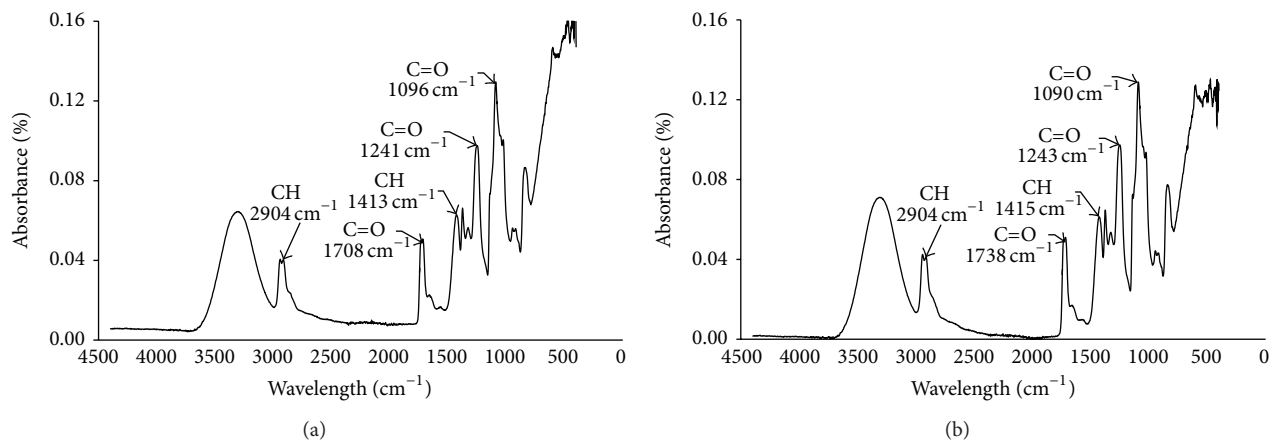


FIGURE 4: FTIR of the electrospun PVA nanofibers (a) and PVA nanofibers contain CNFs (b).

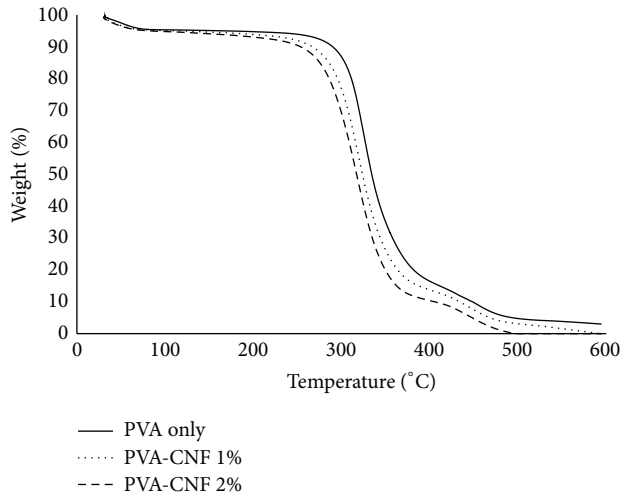


FIGURE 5: Weight loss versus temperature measured by TGA of PVA nanofibers: PVA: CNFs 1% wt nanofibers and PVA: CNFs 2% wt nanofibers.

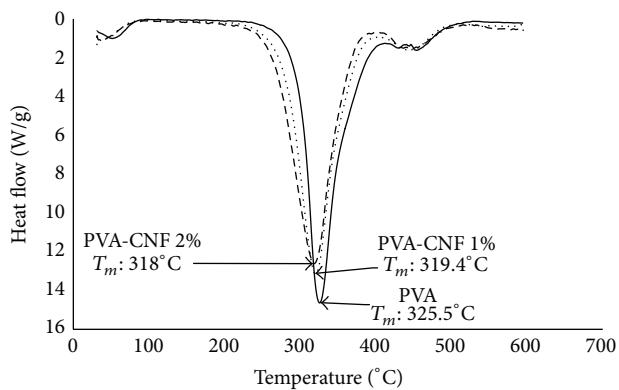


FIGURE 6: First derivative of weight loss versus temperature measured by TGA of PVA nanofibers: PVA: CNFs 1% wt nanofibers and PVA: CNFs 2% wt nanofibers.

weight loss is due to accelerating of thermal degradation of PVA due to distributing of thermal energy within PVA matrix through thermal conductivity of carbon fibers [19].

Regarding the DSC analysis of the corresponding electrospun fibers, the melting point of PVA is shifted arbitrary from 178, 186.5, and 190 °C for PVA and PVA with 1% and 2% CNFs, respectively. The shift of the melting point is attributed to the assistance of carbon nanofibers in increasing the degree of crystallization as they act as nucleating agents in the polymer [20]. By addition of 1 wt% of CNFs, the enthalpy is increased approximately 31% (from 59.3 J/g to 77.6 J/g). Further addition of CNFs results in reduction to 51.4 J/g. The first increase in the enthalpy (which is related to the crystallinity percentage) can be attributed to the increase of crystallization process as carbon nanofibers enhance the nucleation and crystallization of PVA. Further additions of CNFs cause reduction in crystallinity percentage, which may be due to agglomeration of carbon nanofibers inside the PVA

matrix, which reduce the required surfaces for nucleation and crystallization [20].

## 4. Conclusions

This paper investigates a new nanocomposite composed of both PVA and carbon nanofibers integrated in one electrospun nanofibers web. This technique shows a simple and cheap way to offer a host for CNFs without affecting them using traditional deposition techniques. Our results show that thermal and electrical conductivities of the formed nanofibers have been improved with increasing of the carbon nanofibers content. SEM images show the homogeneity of the formed PVA and carbon nanofibers in one web, with stretched CNFs after the electrospinning process. TGA results show that the degradation of PVA nanofibers is favored by addition of carbon nanofibers due to increase of thermal conductivity. DSC results show that addition of carbon nanofibers within PVA nanofibers increases the degree of crystallization of PVA around 31%. The formed nanocomposite can be used in wide variety of applications including nanoelectronics and nanomedicine.

## Conflict of Interests

The authors declare that they have no competing interests.

## Authors' Contribution

Nader Shehata carried out the mixing of CNFs within PVA solution to obtain the optimum concentrations applicable for electrospinning process. In addition, Nader Shehata did the electrospinning process with selection of the optimum process parameters. Nabil Madi and Mariam Al-Maadeed both guided Nader Shehata in the overall work in addition to the critical revision of the paper. Ibrahim Hassounah contributed critically in the explanation of the resulted data especially the FTIR spectroscopy analysis. Abdullah Ashraf followed up the different characterizations done in Central Laboratory Unit (CLU) in Qatar University. All authors read and approved the final paper.

## Acknowledgments

This work was funded by a QSTP grant (Award no. 0906). The authors would like to thank Central Laboratory Unit (CLU) in Qatar University for their assistance through the used characterization facilities. Also, the authors are grateful to the financial support of Center of Advanced Materials (CAM) in Qatar University and Virginia Tech Middle East and North Africa (VT-MENA) program in Egypt.

## References

- [1] J.-B. Donnet, T. K. Wang, S. Rebouillat, and J. Peng, *Carbon Fibers*, Taylor & Francis, New York, NY, USA, 3rd edition, 1998.
- [2] P. Morgan, *Carbon Fibers and Their Composites*, Taylor & Francis, Boca Raton, Fla, USA, 2005.

- [3] N. Yusof and A. F. Ismail, "Post spinning and pyrolysis processes of polyacrylonitrile (PAN)-based carbon fiber and activated carbon fiber: a review," *Journal of Analytical and Applied Pyrolysis*, vol. 93, pp. 1–13, 2012.
- [4] J. Wu and D. D. L. Chung, "Increasing the electromagnetic interference shielding effectiveness of carbon fiber polymer-matrix composite by using activated carbon fibers," *Carbon*, vol. 40, no. 3, pp. 445–447, 2002.
- [5] C. Liu, F. Li, L.-P. Ma, and H.-M. Cheng, "Advanced materials for energy storage," *Advanced Materials*, vol. 22, pp. E28–E62, 2010.
- [6] L. Larrondo and R. S. J. Manley, "Electrostatic fiber spinning from polymer melts. I. Experimental observations on fiber formation and properties," *Journal of Polymer Science: Polymer Physics*, vol. 19, no. 6, pp. 909–920, 1981.
- [7] Y. M. Shin, M. M. Hohman, M. P. Brenner, and G. C. Rutledge, "Electrospinning: a whipping fluid jet generates submicron polymer fibers," *Applied Physics Letters*, vol. 78, no. 8, article 1149, 2001.
- [8] W. Liu, M. Graham, E. A. Evans, and D. H. Reneker, "Poly(meta-phenylene isophthalamide) nanofibers: coating and post processing," *Journal of Materials Research*, vol. 17, no. 12, pp. 3206–3212, 2002.
- [9] I. A. Hassounah, N. A. Shehata, G. C. Kimsawatde et al., "Studying the activity of antituberclousis drugs inside electrospun polyvinyl alcohol, polyethylene oxide, and polycaprolacton nanofibers," *Journal of Biomedical Materials Research Part A*, vol. 102, no. 11, pp. 4009–4016, 2014.
- [10] S. Matsumura, Y. Shimura, K. Terayama, and T. Kiyohara, "Effects of molecular weight and stereoregularity on biodegradation of poly(vinyl alcohol) by *Alcaligenes faecalis*," *Biotechnology Letters*, vol. 16, no. 11, pp. 1205–1210, 1994.
- [11] T. Mori, M. Sakimoto, T. Kagi, and T. Sakai, "Isolation and characterization of a strain of *Bacillus megaterium* that degrades poly(vinyl alcohol)," *Bioscience, Biotechnology and Biochemistry*, vol. 60, no. 2, pp. 330–332, 1996.
- [12] K. Nakamiya and S. K. Toshihiko, "Degradation of synthetic water-soluble hydroquinone peroxidase," *Journal of Fermentation and Bioengineering*, vol. 84, pp. 213–218, 1997.
- [13] R. Marchal, E. Nicolau, J.-P. Ballaguet, and F. Bertoncini, "Biodegradability of polyethylene glycol 400 by complex microfloras," *International Biodeterioration and Biodegradation*, vol. 62, no. 4, pp. 384–390, 2008.
- [14] A. Zgoła-Grześkowiak, T. Grześkowiak, J. Zembruska, and Z. Łukaszewski, "Comparison of biodegradation of poly(ethylene glycol)s and poly(propylene glycol)s," *Chemosphere*, vol. 64, no. 5, pp. 803–809, 2006.
- [15] J. Tao, *Effects of molecular weight and solution concentration on electrospinning of PVA [M.S. thesis]*, Worcester Polytechnic Institut, 2003.
- [16] S. Matsumura, H. Kurita, and H. Shimokobe, "Anaerobic biodegradability of polyvinyl alcohol," *Biotechnology Letters*, vol. 15, no. 7, pp. 749–754, 1993.
- [17] I. Hassounah, N. Shehata, A. Hudson, B. Orler, and K. Meehan, "Characteristics and 3D formation of PVA and PEO electrospun nanofibers with embedded urea," *Journal of Applied Polymer Science*, vol. 131, no. 3, Article ID 39840, 2014.
- [18] L. Zhang, A. Aboagye, A. Kelkar, C. Lai, and H. Fong, "A review: carbon nanofibers from electrospun polyacrylonitrile and their applications," *Journal of Materials Science*, vol. 49, no. 2, pp. 463–480, 2014.
- [19] N. Diouri and M. Baitoul, "Effect of carbon nanotubes dispersion on morphology, internal structure and thermal stability of electrospun poly(vinyl alcohol)/carbon nanotubes nanofibers," *Optical and Quantum Electronics*, vol. 46, no. 1, pp. 259–269, 2014.
- [20] M. A. AlMaadeed, R. Kahraman, P. Noorunnisa Khanam, and N. Madi, "Date palm wood flour/glass fibre reinforced hybrid composites of recycled polypropylene: mechanical and thermal properties," *Materials and Design*, vol. 42, pp. 289–294, 2012.

## Research Article

# Development of a Composite Electrospun Polyethylene Terephthalate-Polyglycolic Acid Material: Potential Use as a Drug-Eluting Vascular Graft

Christoph S. Nabzdyk,<sup>1</sup> Maggie Chun,<sup>1</sup> Saif G. Pathan,<sup>2</sup> David W. Nelson,<sup>2</sup> Jin-Oh You,<sup>3,4</sup> Matthew D. Phaneuf,<sup>2</sup> Frank W. LoGerfo,<sup>1</sup> and Leena Pradhan-Nabzdyk<sup>1</sup>

<sup>1</sup>Division of Vascular and Endovascular Surgery, Beth Israel Deaconess Medical Center, Harvard Medical School, Boston, MA 02215, USA

<sup>2</sup>BioSurfaces, Inc., Ashland, MA 01721, USA

<sup>3</sup>Harvard School of Engineering and Applied Sciences, Cambridge, MA 02138, USA

<sup>4</sup>Department of Engineering Chemistry, Chungbuk National University, Cheongju, Chungbuk 28644, Republic of Korea

Correspondence should be addressed to Leena Pradhan-Nabzdyk; [lpradhan@bidmc.harvard.edu](mailto:lpradhan@bidmc.harvard.edu)

Received 15 April 2015; Revised 24 July 2015; Accepted 3 August 2015

Academic Editor: Mircea Chipara

Copyright © 2015 Christoph S. Nabzdyk et al. This is an open access article distributed under the Creative Commons Attribution License, which permits unrestricted use, distribution, and reproduction in any medium, provided the original work is properly cited.

Intimal hyperplasia (IH), an excessive wound healing response of an injured vessel wall after bypass grafting, typically leads to prosthetic bypass graft failure. In an approach to ameliorate IH, nondegradable poly(ethylene terephthalate) or PET, which has been used in prosthetic vascular grafts for over 60 years, and biodegradable poly(glycolic acid) or PGA were electrospun using different techniques to generate a material that may serve as permanent scaffold and as a drug/biologic delivery device. PET and PGA polymers were electrospun from either a single-blended solution (ePET/ePGA-s) or two separate polymer solutions (ePET/ePGA-d). ePET/ePGA-d material revealed two distinct fibers and was significantly stronger than the single fiber ePET/ePGA-s material. After 21 days of incubation in PBS, ePET-PGA-s showed fiber strand breaks likely due to the degradation of the PGA within the ePET-ePGA-s fiber, while the ePET/ePGA-d material showed intact ePET fibers even after ePGA fiber degradation. The ePET/ePGA- material was able to release red fluorescent dye for at least 14 days. Attachment of human aortic smooth muscle cells (AoSMCs) was similar to both materials. ePET/ePGA-d materials maybe a step towards bypass graft materials that can be custom-designed to promote cellular attachment while serving as a drug delivery platform for IH prevention.

## 1. Introduction

Prosthetic bypass graft failure is most frequently a result of intimal hyperplasia (IH) at the distal anastomosis [1]. IH is the result of an excessive wound healing response of an injured vessel wall after bypass grafting or angioplasty. Hallmarks of IH are endothelial activation followed by the ad luminal migration of synthetic smooth muscle cells that secrete significant amounts of extracellular matrix. This eventually leads to a hemodynamically relevant luminal narrowing of the conduit. Poly(ethylene terephthalate) or PET has been used for arterial bypass grafts for over 60 years in woven or knitted constructs, both of which require sealants

to prevent blood seepage through the graft wall. None of these structural variants have provided a scaffold that mimicked extracellular matrix (ECM), a major component of a blood native vessel onto which cells can grow.

Electrospinning is a versatile technology that can yield nanofiber materials. Interestingly, the materials' ultrastructure resembles that of ECM [2]. Electrospinning can be used for controlled fiber modification and nanocomposite substrate integration [3, 4]. The materials' ultrastructure characteristically consists of crisscrossing nano- to micrometer thick fibrils, resembling extracellular matrix. This ultrastructure not only results in a large surface area, which could be utilized for drug delivery, but also allows cellular trafficking.

Aside from optimizing prosthetic bypass grafts, researchers have attempted to prevent IH formation via drug release from the prosthetic graft surface [5].

Microarray analysis of developing canine IH lesions identified various target genes that were dysregulated for up to four weeks after bypass graft implantation [6]. RNAi interference may become a promising technology that may help modulate expression of genes contributing to IH and other cardiovascular diseases [7–9]. As cellular signaling networks are highly redundant, it may be necessary to modulate/silence multiple genes in either a synchronous or metachronous fashion. In a previous study from our group, short-term RNAi release from dip-coated electrospun PET grafts was shown to significantly silence target gene-expression of infiltrating human aortic smooth muscle cells [2]. siRNA dip-coating of ePET did not interfere with cell adhesion, infiltration, or cell viability [2].

The next logical step was to introduce a degradable component into the ePET material using electrospinning technology that could act as reservoir for siRNA or other therapeutic compounds with the goal to prolong siRNA release from within the material. Poly(glycolic acid) or PGA, a biocompatible ester that degrades predictably by ester hydrolysis, appears to be a good candidate biomaterial to provide localized drug delivery. The final construct must meet the following requirements: (1) degradable component has to completely degrade over a predictable period of time, (2) composite material has to retain its backbone structure of robust ePET, (3) introduction of a degradable component should not interfere with cell attachment, and (4) therapeutic compound should be preferentially stored in the degradable component and not in the nondegradable ePET.

The goal of this study is to design and evaluate a composite electrospun material that consists of a nondegradable ePET backbone and interspersed degradable polyglycolic acid (PGA) fibers for biodegradation, simulated drug release, and cell attachment.

## 2. Methods

**2.1. Electrospinning of ePET/ePGA Materials.** Electrospinning of ePET, ePGA, single solution ePET/ePGA (ePET/ePGA-s), and dual solution ePET/ePGA (ePET/ePGA-d) was done using a computer-automated electrospinning apparatus. PET (10% w : v) and/or PGA (10% w : v) polymer chips were dissolved in hexafluoroisopropanol (HFIP) and mixed for a minimum of 48 hours on an inversion mixer at 45 rpm. The PET, PGA, PET/PGA-s (blended), and PET/PGA-d (electrospun at the same time from different solutions) were each electrospun using a steady rate of 3 mL solution/hour at +20 kV for 60 minutes. The resulting electrospun materials were collected onto a Teflon-coated mandrel (30 cm diameter). In another set of experiments, DyLight 549 was added to the PGA and PET solutions, respectively, prior to electrospinning. The electrospun materials were dried for 48 hours at 40°C at 99.9% vacuum. All materials were sterilized via ethylene oxide at 25°C for 12 hours under humidified conditions in an Anprolene Sterilizer. Expanded polytetrafluoroethylene (PTFE), one of the more commonly

used materials for prosthetic vascular grafts, served as a clinical reference material for the surface morphology and cell culture studies.

**2.2. Evaluation of Tensile Strength of ePET, ePGA, ePET/PGA-s, and ePET-PGA-d Materials.** Sheets of ePET, ePGA, ePET/ePGA-s, and ePET/ePGA-d were cut into rectangular strips (20 mm × 5 mm;  $n = 5$  segments/test group/test condition), with thickness measured using an Ames Thickness Gauge. Strength testing was carried out using a Q-Test Tensile Strength apparatus (MTS Systems, Cary, NC) with a 25 lb load cell and clamps set at a gap distance of 5 mm. The clamp traverse speed was set at a 200 mm/min strain rate until break.

**2.3. Degradation and DyLight 549 Release Studies.**  $5 \times 5$  mm<sup>2</sup> segments of ePET, ePET/ePGA-s, and ePET/ePGA-d materials were placed in sterile phosphate buffered saline (PBS) and incubated at 37°C on an orbital shaker for up to 21 days. Samples were rinsed, air-dried, and evaluated using scanning electron microscopy (SEM) or confocal imaging, respectively, using standard techniques.

**2.4. Quantification of AoSMC Attachment to PTFE Electrospun Material.** Primary human aortic smooth muscle cells (AoSMCs) (Lonza, Walkersville, MD) (passages 4–8) were cultured as described previously [10].  $5 \times 5$  mm<sup>2</sup> segments of each material were cut and placed into 96-well tissue culture plates. AoSMCs (40,000 cells/well) were seeded on top of PTFE, ePET, ePET/ePGA-s, and ePET/ePGA-d materials and allowed to attach. After 3 hours, segments were removed, rinsed, and placed in a new well. AlamarBlue<sup>®</sup> assay was then used to assess cell attachment [2, 10]. AoSMC attachment to the tissue culture well alone served as the positive attachment control and Alamar blue within an empty well served as a negative control.

**2.5. Statistical Analysis.** One-way analysis of variance (ANOVA) with Bonferroni post hoc correction was applied. A  $p$  value < 0.05 was considered significant.

## 3. Results

**3.1. Fiber Morphology.** While the PTFE graft material consisted of predominantly parallel-aligned fibers with little interfiber space arranged between thick nodes (Figure 1(a)), the ePET material consisted of a fiber mesh with variable interfiber spaces with relatively reduced fiber diameter distribution (Figure 1(b)). ePGA, ePET/ePGA-s, and ePET/PGA-d fibers also showed distinct fiber strand architecture (Figures 1(c)–1(f); left panel).

**3.2. Polymer Degradation Using SEM.** Degradation studies of the ePGA material alone over a 21-day period revealed initial fiber swelling and gradual degradation (Figures 1(c) and 1(d); middle and right panel). Degradation of ePET-PGA-s material resulted in strand breaks between 14 and 21 days (Figure 1(e); middle and right panel) whereas the ePET/ePGA-d material showed that only ePGA fibers

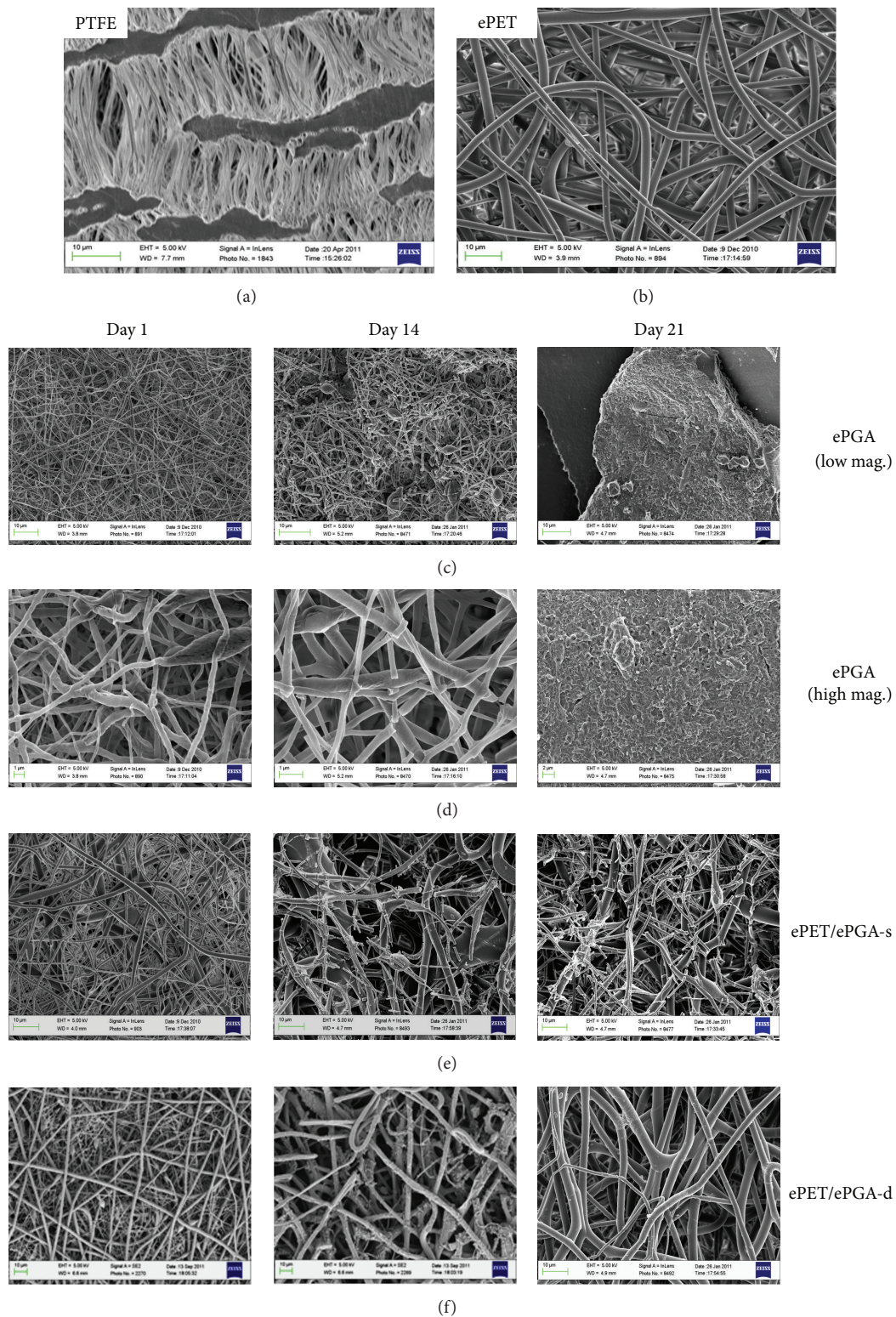


FIGURE 1: Evaluation of surface morphology of control and electrospun materials via SEM: representative SEM pictures of PTFE and ePET (a and b). SEM analysis of ePGA fiber degradation as a single or a composite material with PET. ePGA fibers gradually degrade over 14–21 days in PBS (c and d). In contrast, after ePGA degradation the ePET/ePGA-s (e) or ePET/ePGA-d materials (f) still have a fibrous composition due to the nondegrading ePET fibers. Note the strand breaks in the ePET/ePGA-s group (presumably due to PGA degradation) while no strand breaks occurred in the ePET/ePGA-d group.

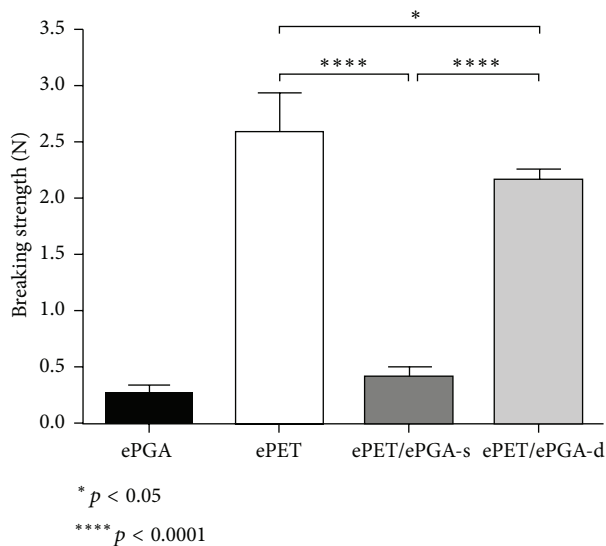


FIGURE 2: Evaluation of tensile strength of the electrospun materials: electrospun materials were evaluated for tensile strength. ePET is the strongest material, while ePGA is the weakest. ePET/ePGA-d had significantly higher strength as compared to ePET/ePGA-s.

degrade over time, leaving an intact ePET fiber network behind (Figure 1(f); middle and right panel) that closely resembles the network of single strand ePET fibers seen in Figure 1(b). ePET/ePGA-d thus has the potential of retaining all of its strength meanwhile allowing more porous architecture for cells to infiltrate and heal the graft as the electrospun PGA component degrades and releases the active siRNA.

**3.3. Tensile Strength.** ePET materials had significantly more strength ( $2.57 \pm 0.34$  N) as compared to ePET/PGA-d ( $2.16 \pm 0.10$  N) and ePET/PGA-s ( $0.42 \pm 0.07$  N) materials, respectively ( $p \leq 0.0001$ ) (Figure 2). Maintaining the ePGA as a separate fiber allowed the ePET/PGA-d material to retain a majority of its strength as compared to ePET/PGA-s, which was significantly weaker. ePGA material alone ( $0.25 \pm 0.08$  N) was the weakest of all of the materials evaluated. We also observed that, compared to ePET/PGA-d, ePET had a slightly higher (19%) strength.

**3.4. Identification of ePGA Fiber Location via Using Fluorescent Labeling.** A clear separation between fluorescently labeled ePGA and nonlabeled ePET strands can be seen in the ePET/ePGA-d materials indicating no cross-reaction between the two individual polymers (Figure 3(a)). The electrospinning procedure allowed for adjustable fiber ratio within the length of the ePET/ePGA-d polymer (Figure 3(b)).

**3.5. DyLight 549 Release from ePGA.** Confocal imaging showed that DyLight 549 was released from ePGA of the ePET/PGA-d polymer over 14 days (Figure 4). This DyLight 549 release profile correlated well with the observed degradation rate of the ePGA fibers.

**3.6. Cell Attachment.** AoSMC attachment to both ePET and ePET/ePGA-d polymers was significantly higher as compared to PTFE (Figure 5). AoSMC attachment to all of the

electrospun materials was higher than that of culture plate. The introduction of ePGA fibers in both of the composite polymers did not appear to alter the attachment to the ePET backbone fiber mesh.

## 4. Discussion

Electrospinning can be used to generate various materials from different polymers [3, 4]. In this study, coelectrospinning resulted in a composite material of a nondegradable and a degradable polymer without polymer cross-reaction. Coelectrospinning of the PET with PGA results in the least reduction of tensile strength as compared to a single solution electrospin. This strength data validates that blending the solutions results in comingling of fibers that may ultimately reduce overall device strength.

More importantly, a compound can be incorporated and released upon ePGA degradation as indicated by DyLight release. The molecular weight of the DyLight molecule is similar to that of bioactive agents such as antiproliferative drugs and siRNA. Even after PGA degradation, there were no strand breaks observed in ePET/ePGA-d materials after 21 days in solution, which is reassuring in regard to the tensile strength of the polymer. Given that ePET/ePGA-d polymer contains a nondegradable and load-bearing component in the form of ePET, mechanical failure of the proposed graft is not a concern, especially when compared to fully degradable bypass grafts [3, 11, 12].

AoSMC attachment was not affected when ePGA was introduced into the composite polymer. This is an important finding, as an ideal graft design should promote initial cell attachment and growth. Further, the electrospinning protocols allowed for fiber density variation within the coelectrospun polymer, which could be used to generate therapeutic compound gradients within the graft.



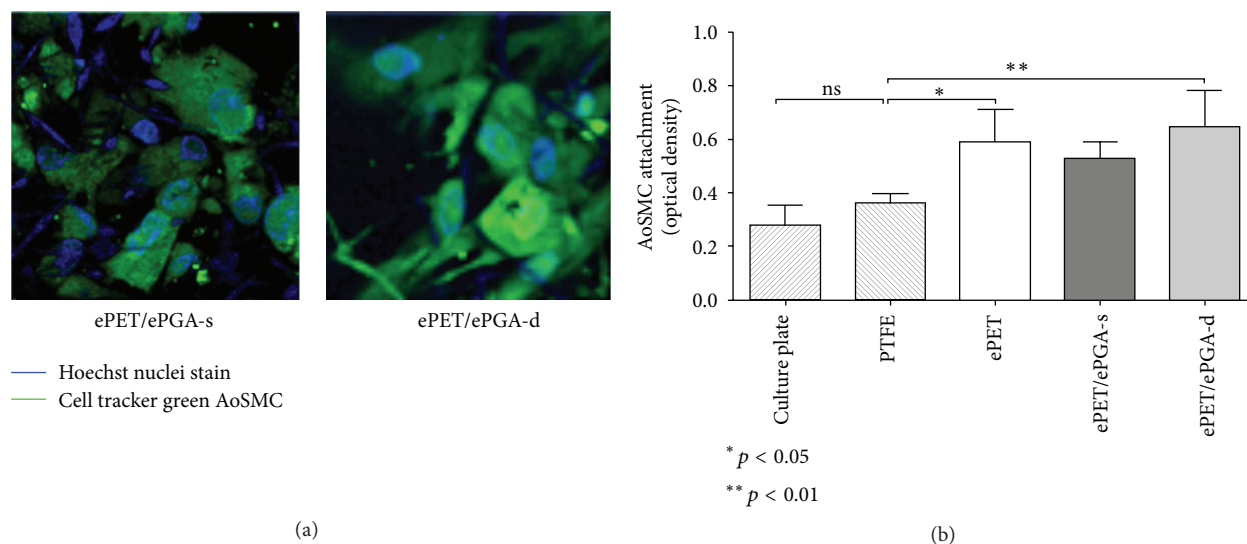


FIGURE 5: AoSMC attachment to electrospun materials: confocal imaging (a) and Alamar blue assay evaluating AoSMC attachment to composite electrospun polymers (b). AoSMC attachment was greatest in the electrospun materials as compared to the attachment on the PTFE and tissue culture plate, respectively. There was no significant difference in AoSMC binding between the electrospun materials.

This data provides first evidence that coelectrospinning of ePET/ePGA may be a viable option for sustained local drug delivery from within a prosthetic arterial bypass graft. This technology will be combined in future experiments with our previously published approach for short-term siRNA release from electrospun PET materials [2]. Additional studies will extensively analyze drug/siRNA loading and delivering capacities, biocompatibility, and tensile strength *in vitro* and *in vivo* to evaluate the material's properties as drug delivering vascular prostheses. Introduction of other polymers such as poly(lactic-co-glycolic acid) (PLGA) and polycaprolactone (PCL) with slower degradation rates than PGA may aid in providing sequential and even more sustained drug/siRNA release from the material [3, 11, 12] while possibly adding a stronger polymer to the cospin. These polymer moderations could act synergistically to comprehensively modulate the tissue response to material implantation. This approach may become a platform technology for various biomaterial modifications and applications for implantable surgical devices and possibly arterial bypass grafts.

### Conflict of Interests

The authors declare that there is no conflict of interests regarding the publication of this paper.

### Acknowledgments

This work was supported by NIH 5R01 HL021796-30, NIH 2R01 HL086741-08, T32 HL007734-21, and the William J. von Liebig Foundation funds to Frank W. LoGerfo.

### References

- [1] V. S. Sottirai, J. S. T. Yao, W. R. Flinn, and R. C. Batson, "Intimal hyperplasia and neointima: an ultrastructural analysis

- of thrombosed grafts in humans," *Surgery*, vol. 93, no. 6, pp. 809–817, 1983.
- [2] C. S. Nabzdyk, M. C. Chun, H. S. Oliver-Allen et al., "Gene silencing in human aortic smooth muscle cells induced by PEI-siRNA complexes released from dip-coated electrospun poly(ethylene terephthalate) grafts," *Biomaterials*, vol. 35, no. 9, pp. 3071–3079, 2014.
- [3] S. Wang, X. M. Mo, B. J. Jiang et al., "Fabrication of small-diameter vascular scaffolds by heparin-bonded P(LLA-CL) composite nanofibers to improve graft patency," *International Journal of Nanomedicine*, vol. 8, pp. 2131–2139, 2013.
- [4] J. Han, S. Farah, A. J. Domb, and P. I. Lelkes, "Electrospun rapamycin-eluting polyurethane fibers for vascular grafts," *Pharmaceutical Research*, vol. 30, no. 7, pp. 1735–1748, 2013.
- [5] C. Cagiannos, O. R. Abul-Khoudoud, W. DeRijk et al., "Rapamycin-coated expanded polytetrafluoroethylene bypass grafts exhibit decreased anastomotic neointimal hyperplasia in a porcine model," *Journal of Vascular Surgery*, vol. 42, no. 5, pp. 980–988, 2005.
- [6] M. Bhasin, Z. Huang, L. Pradhan-Nabzdyk et al., "Temporal network based analysis of cell specific vein graft transcriptome defines key pathways and hub genes in implantation injury," *PLoS ONE*, vol. 7, no. 6, Article ID e39123, 2012.
- [7] S. M. Elbashir, J. Harborth, W. Lendeckel, A. Yalcin, K. Weber, and T. Tuschl, "Duplexes of 21-nucleotide RNAs mediate RNA interference in cultured mammalian cells," *Nature*, vol. 411, no. 6836, pp. 494–498, 2001.
- [8] C. S. Nabzdyk, H. Lancero, K. P. Nguyen, S. Salek, and M. S. Conte, "RNA interference-mediated survivin gene knockdown induces growth arrest and reduced migration of vascular smooth muscle cells," *American Journal of Physiology—Heart and Circulatory Physiology*, vol. 301, no. 5, pp. H1841–H1849, 2011.
- [9] L. Pradhan-Nabzdyk, C. Huang, F. W. LoGerfo, and C. S. Nabzdyk, "Current siRNA targets in atherosclerosis and aortic aneurysm," *Discovery Medicine*, vol. 17, no. 95, pp. 233–246, 2014.

- [10] S. Yoshida, C. S. Nabzdyk, L. Pradhan, and F. W. Logerfo, "Thrombospondin-2 gene silencing in human aortic smooth muscle cells improves cell attachment," *Journal of the American College of Surgeons*, vol. 213, no. 5, pp. 668–676, 2011.
- [11] S. Chung, N. P. Ingle, G. A. Montero, S. H. Kim, and M. W. King, "Bioresorbable elastomeric vascular tissue engineering scaffolds via melt spinning and electrospinning," *Acta Biomaterialia*, vol. 6, no. 6, pp. 1958–1967, 2010.
- [12] M. Chen, S. Gao, M. Dong et al., "Chitosan/siRNA nanoparticles encapsulated in PLGA nanofibers for siRNA delivery," *ACS Nano*, vol. 6, no. 6, pp. 4835–4844, 2012.

## Research Article

# Synthesis of Salt Responsive Spherical Polymer Brushes

Na Su,<sup>1</sup> Houbin Li,<sup>2,3</sup> Yu Huang,<sup>2</sup> and Xiongzi Zhang<sup>4</sup>

<sup>1</sup>School of Printing and Packaging Engineering, Shanghai Publishing and Printing College, Shanghai 200093, China

<sup>2</sup>School of Printing and Packaging, Wuhan University, Wuhan 430079, China

<sup>3</sup>State Key Laboratory of Pulp and Paper Engineering, South China University of Technology, Guangzhou 510006, China

<sup>4</sup>College of Chemistry and Molecular Sciences, Wuhan University, Wuhan 430072, China

Correspondence should be addressed to Na Su; [suna@whu.edu.cn](mailto:suna@whu.edu.cn)

Received 5 April 2015; Accepted 12 July 2015

Academic Editor: Mircea Chipara

Copyright © 2015 Na Su et al. This is an open access article distributed under the Creative Commons Attribution License, which permits unrestricted use, distribution, and reproduction in any medium, provided the original work is properly cited.

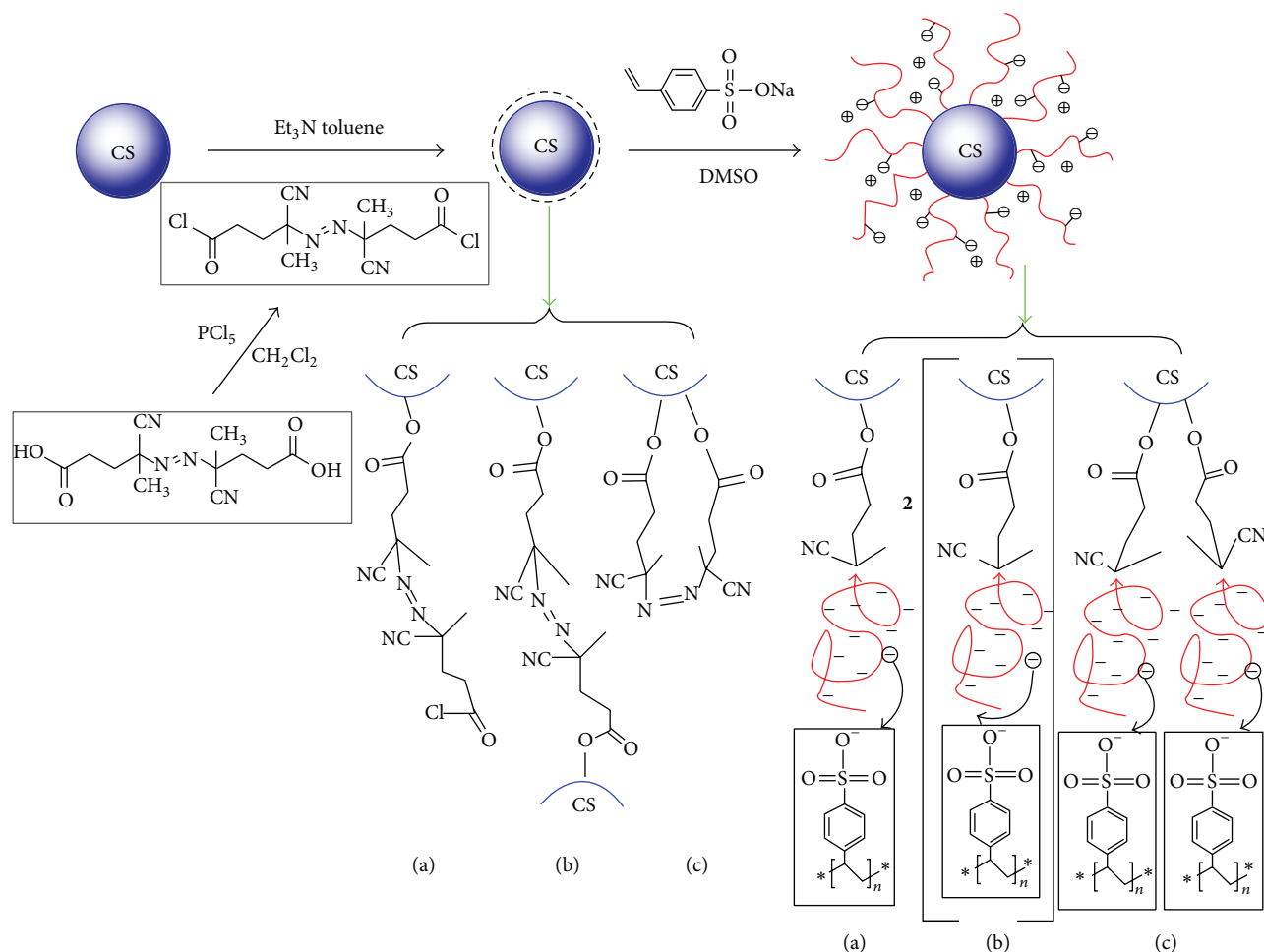
A facile preparation of novel salt responsive spherical polymer brushes (SPB) consisting of a carbon spheres core and a shell of sodium polystyrene sulfonate (PSSNa) was described. The SPB were characterized by scanning electron microscopy (SEM), transmission electron microscopy (TEM), Fourier transform infrared spectroscopy (FTIR), and thermogravimetric analysis (TGA). The radius  $R$  of carbon spheres and hydrodynamic radius  $R_h$  of SPB were ca. 370 nm and 785 nm, respectively. The brushes had  $M_w$  of 393600 g/mol with polydispersity  $M_w/M_n$  of 1.58. Furthermore, the dependence of PSSNa brushes on ionic strength and pH was investigated.

## 1. Introduction

Spherical polymer brushes (SPB) are formed by grafting charged polymers densely to the surface of spheres so that polymer chains can stretch away in brush-like conformation [1]. Recently, SPB have attracted wide attention in the field of polymer science due to entirely new properties that come from the strong electrostatic interaction between densely grafted charged chains. This strong electrostatic interaction will lead to a significant stretching of the chains as long as the surrounding medium is a good solvent for the attached polymer chains. However, the swelling of polyelectrolyte brushes may be sensitive to some parameters of the medium such as pH value, ionic strength, and temperature, which make it a wide range of potential applications in catalysis [2, 3], drug delivery [4], protein separation [5], papermaking [6], and printed electronics [7]. Printed electronics technology is based on the principle of printed electronics manufacturing technology [8]. The application in the field of printed electronics [7, 9] for SPB is mainly because that the brush-like conformation [1] of SPB can serve as the nanoreactors for conductive nanoparticles [10]. Undoubtedly, the synthesis process and property of SPB are crucial to its application.

For one thing, carbon materials with the intrinsic characteristics of light weight, high thermal resistance, and high strength are widely used in sensing [11], super capacitors [12], and catalysis [13], so SPB with carbon spheres (CS) have become an interesting research object for many researchers. Jin et al. [14] grafted polymers (PMMA, PS, and PGMA) onto the surface of CS by a surface-initiated ATRP process, and the wetting ability and dispersibility of crude CS were improved. Wang et al. [15] modified polystyrene-based activated CS to improve their adsorption properties of dibenzothiophene. Zhang et al. [16] synthesized SPB by grafting poly(diallyl dimethyl ammonium chloride) (p-DMDAAC) on the surface of CS for potential applications in papermaking. Compared to SPB with SiO<sub>2</sub> cores we have prepared [17], SPB with CS cores have potential applications in printing electronics because of excellent electrical conductivity of carbon materials.

For another thing, as the nanoreactors of conductive nanoparticles, SPB should have high molecular weight of brushes and controllable swelling behavior. Therefore, salt responsive SPB consisting of a CS core and a shell of sodium polystyrene sulfonate (PSSNa) brushes by surface-initiated polymerization (a technique of “grafting from”) were synthesized in this paper. In comparison with the molecular



SCHEME 1: Schematic representations of synthesis process of SPB. Number 2 refers to double-ended form grafted on hetero-CS.

weight of brushes by the method of conventional free radical polymerization in our previous work [18], a relatively higher maximum thickness of polymer chains was obtained by this technique and is easily controlled concerning layer thickness, graft density, charge density, and swelling behavior [19]. CS was prepared by hydrothermal method. Compared with other methods such as pyrolysis of hydrocarbons [14], chemical vapor deposition [20], and laser ablation [21], this technique has easy operation, low cost, and low pollution. The synthesis of SPB included two steps (Scheme 1). Azo initiator was firstly initiated to the surface of CS; surface-initiated polymerization of sodium 4-vinylbenzenesulfonate monomer was then conducted.

## 2. Materials and Methods

**2.1. Materials.** 4,4'-Azobis(4-cyanovaleric acid) and sodium 4-vinylbenzenesulfonate (NaSS) were purchased from Aladdin Reagent Co., Ltd. (Shanghai, China) in analytical grade and used as received.  $\text{PCl}_5$  was obtained from Shanghai Tingxin Chemical Factory (Shanghai, China). Dichloromethane, toluene, methanol, ethanol, triethylamine, dimethyl sulfoxide (DMSO), and D-(+)-glucose ( $\text{C}_6\text{H}_{12}\text{O}_6 \cdot \text{H}_2\text{O}$ )

were obtained from Sinopharm Chemical Reagent Co., Ltd. (Shanghai, China). Toluene was refluxed over sodium and dichloromethane was distilled over calcium hydride ( $\text{CaH}_2$ ) prior to use. All other chemicals were of analytical grade and used without any further treatment.

**2.2. Synthesis of Carbon Spheres.** 6 g of glucose was dissolved in 50 mL deionized water and the solution was sealed in a Teflon-lined stainless steel autoclave and heated at  $180^\circ\text{C}$  for 6 h. The products were filtered off, washed three times with ethanol and deionized water, respectively, and freeze-dried by freezing at  $-30^\circ\text{C}$  for 24 h.

**2.3. Synthesis of 4,4'-Azobis(4-cyanovaleric acid).** 5.6 g of 4,4'-azobis(4-cyanovaleric acid) (20 mmol) was suspended in 40 mL dry dichloromethane. The white suspension was cooled to  $0^\circ\text{C}$  in an ice bath. About 8.32 g of  $\text{PCl}_5$  (40 mmol) in 100 mL dry dichloromethane was added dropwise to the reaction mixture. Then the reaction mixture was allowed to warm up to room temperature and stirred overnight. After several hours, the solution became clear and was concentrated to about 20 mL. A white solid can be obtained by adding 300 mL cold n-hexane to the concentrated solution.

The solid was then filtered and dried overnight under vacuum. FTIR (KBr): 2994, 2944, 2240, and 1790  $\text{cm}^{-1}$ ;  $^1\text{H}$  NMR ( $\text{CDCl}_3$ , ppm): 2.9–3.2 (m, 4H,  $\text{CH}_2\text{CO}$ ), 2.4–2.7 (m, 4H,  $\text{CH}_2\text{C}$ ), and 1.7 (s, 6H,  $\text{CH}_3$ ).

**2.4. Immobilization of Azo Initiator on Carbon Spheres Surface.** 1.0 g of CS was dispersed in 30 mL dry toluene followed by addition of 3.17 g of 4,4'-azobis(4-cyanopentanoyl chloride) and 3 mL triethylamine. The mixture was stirred at room temperature for 24 h. The products were centrifuged and washed three times with toluene and methanol, respectively, before being dried overnight in a vacuum oven.

**2.5. Synthesis of Anionic Spherical Polyelectrolyte Brushes.** 1.65 g of sodium 4-vinylbenzenesulfonate monomer and above azo initiator-immobilized CS were added to 20 mL DMSO. Polymerization was carried out at 60°C for 6 h under nitrogen atmosphere. The products were then purified and dried in vacuum at 60°C for 12 h.

**2.6. Characterization.** Scanning electron microscopy (SEM) [Quanta 200] and transmission electron microscopy (TEM) [JEM-2100] were used to observe the morphologies of samples. The chemical compositions of samples were analyzed by energy dispersive X-ray spectrometer (EDX) [Quanta 200]. A qualitative structure analysis of SPB was shown from Fourier transform infrared spectroscopy (FTIR) [Nicolet AVATAR 360]. The  $^1\text{H}$  NMR was measured on a MERCURY-VX300 spectrometer (Variant, USA). UV-visible spectrum was recorded in the region of 200–800 nm using UV-3100 spectrometer (Shimadzu, Japan). Thermogravimetric analysis (TGA) was conducted on a SETSYS-1750 at the heating rate of 10°C/min from 25 to 750°C under a nitrogen flow. The average initial sample mass was ca. 5.0 mg. The weight of all grafted PSSNa brushes ( $m$ ) could be defined by

$$m = m_0 \times \frac{w_0\% - w_1\%}{w\% - w_1\%}, \quad (1)$$

where  $m_0$  is the weight of SPB used for TGA,  $w_0\%$  is weight loss of SPB during the temperature from 200 to 800°C,  $w_1\%$  is mass loss of CS in the same temperature, and  $w\%$  stands for mass loss of PSSNa brushes.

Gel permeation chromatography (GPC) measurement was carried out on Spectra SERIES P100 to obtain the molecular weight and its distribution in PSSNa brushes. The surface grafting density could be defined as moles of polymer graft per gram [mole/g] or per square [mole/ $\text{m}^2$ ] of the matrix. Considering the surface area of carbon particles, the calculation of surface grafting density could also be achieved by chains per square nanometer surface. When the average molecular weight ( $M_w$ ) and the weight of all grafted PSSNa brushes ( $m$ ) are provided, the surface grafting density  $\sigma$  can be calculated using

$$\sigma = \frac{m}{4\pi r_c^2 \times M_w}. \quad (2)$$

The hydrodynamic radius  $R_h$  of SPB and thickness  $L$  of brushes were measured by dynamic light scattering (DLS) using zeta potential/particle sizer (Nicomp 380, USA).

### 3. Results and Discussion

**3.1. Morphology.** The morphologies of CS and SPB are displayed in Figure 1. The CS shows a smooth surface (Figure 1(a)) and the radius  $R$  of CS is ca. 370 nm from DLS result. Unlike the morphologies of CS, an overlayer can be observed in the SEM (Figure 1(b)) and TEM images of SPB (Figures 1(e) and 1(f)), indicating the successful preparation of SPB [14]. The hydrodynamic radius  $R_h$  of SPB is ca. 785 nm determined by DLS. The EDX analysis in Figure 1(c) represents the chemical composition of azo initiator-immobilized CS. The signals corresponding to nitrogen and chlorine appear on the spectrum, suggesting that the azo initiator has been immobilized on CS surface.

**3.2. FTIR Analyses.** Figure 2 shows the FTIR spectra of carbon spheres, azo initiator-immobilized carbon spheres, and SPB. For CS, main peaks at 1705 and 1616  $\text{cm}^{-1}$  are assigned to C=O and C=C vibrations, respectively. Besides, the bands in the region of 1000–1500  $\text{cm}^{-1}$  (Figure 2(a)), corresponding to the C–OH stretching and –OH bending vibrations, indicate the existence of large numbers of residual hydroxy groups [22]. The absorptions of initiator-immobilized CS at 2240 and 1826  $\text{cm}^{-1}$  are attributed to –CN stretching vibrations and C=O stretching vibration (Figure 2(b)), respectively. It demonstrates that azo initiator has been attached on the surface of CS, which is also supported by the EDX analysis. In the spectra of SPB (Figure 2(c)), asymmetric  $\text{SO}_3$  stretching bands at 1177 and 1129  $\text{cm}^{-1}$  as well as symmetric  $\text{SO}_3$  stretching bands at 1043 and 1009  $\text{cm}^{-1}$  can be clearly observed, implying the existence of grafted PSSNa chains [23]. It is noteworthy that C=O stretching vibration of CS at 1705  $\text{cm}^{-1}$  can still be seen in Figure 2(c). All these observations confirm the successful polymerization of SPB by the above method.

**3.3. UV-Vis Absorption Spectra Analyses.** The UV-vis absorption spectra of carbon spheres, SPB, and PSSNa are presented in Figure 3. No absorption occurs in the UV-vis absorption spectrum of carbon spheres (Figure 3(a)). This is because amorphous carbon in the carbon spheres is synthesized by hydrothermal method [24]. However, two characteristic absorptions of PSSNa at 221 and 256 nm can be observed in Figure 4(b), belonging to  $\pi \rightarrow \pi^*$  electron transition from the benzene ring in PSSNa [25]. In the spectrum of SPB (Figure 3(c)), two absorptions of benzene ring from PSSNa are still present, suggesting that the PSSNa chains have been successfully grafted to surface of carbon spheres.

**3.4. Thermal Analyses.** In order to calculate the weight of grafted PSSNa brushes on the surface of modified CS cores, the thermal gravimetric analysis of samples in a nitrogen atmosphere at 60% RH is illustrated (Figure 4). The weight loss below 200°C is probably caused by the loss of absorbed water for all the samples. The weight loss of CS between 200 and 800°C is about 42.7% (Figure 4(a)). And the stage from 200°C to 400°C mainly implies the loss of CS [17]. For pure PSSNa (Figure 4(c)), a 30.5% weight loss occurs at 200–800°C. The mass loss from 400°C to 450°C is mainly

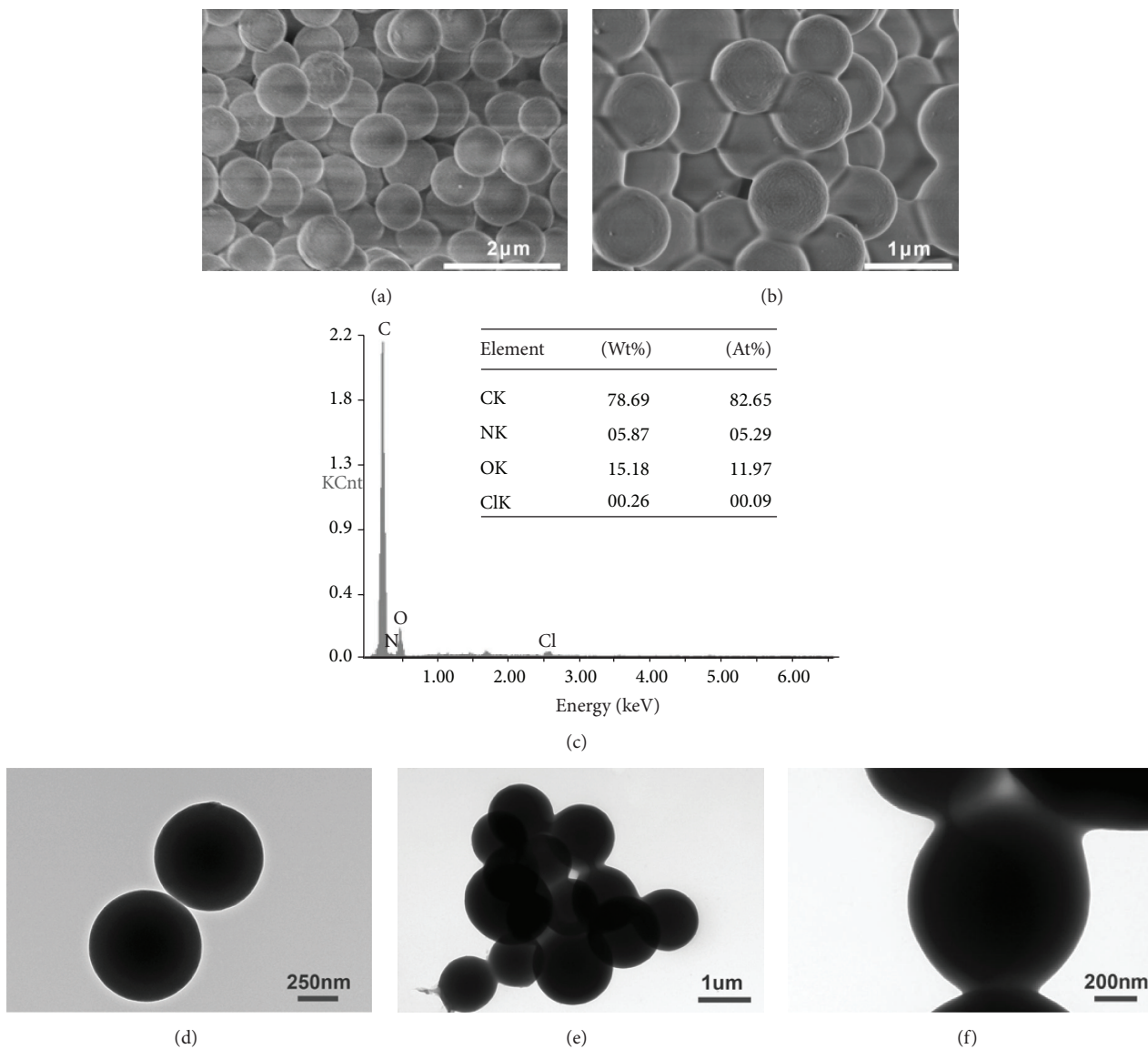


FIGURE 1: SEM images of (a) CS and (b) SPB; (c) EDX analysis of azo initiator-immobilized CS; TEM images of (d) CS and (e-f) SPB.

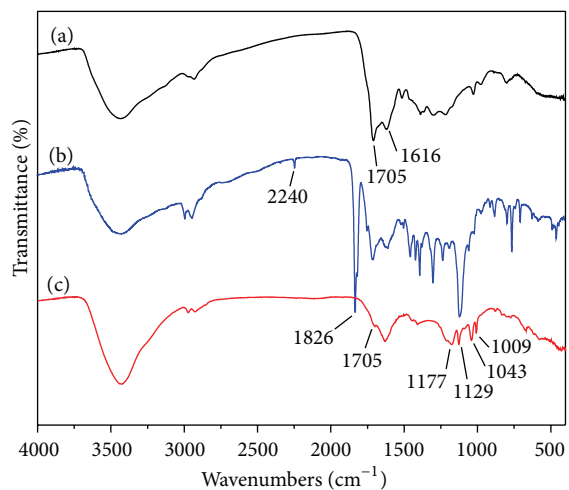


FIGURE 2: FTIR spectra of (a) CS, (b) azo initiator-immobilized CS, and (c) SPB.

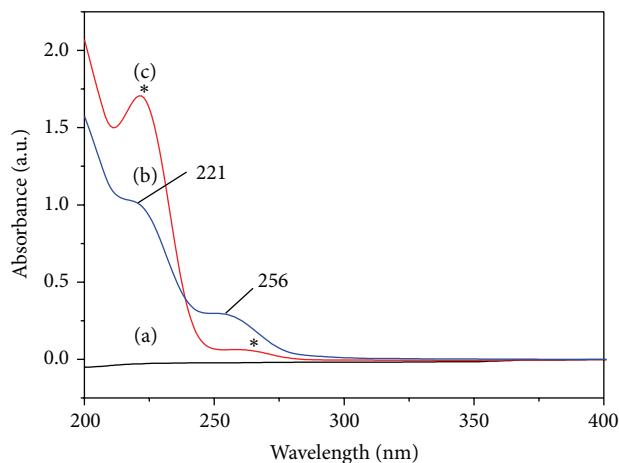


FIGURE 3: UV-vis absorption spectra of (a) carbon spheres, (b) PSSNa, and (c) SPB.

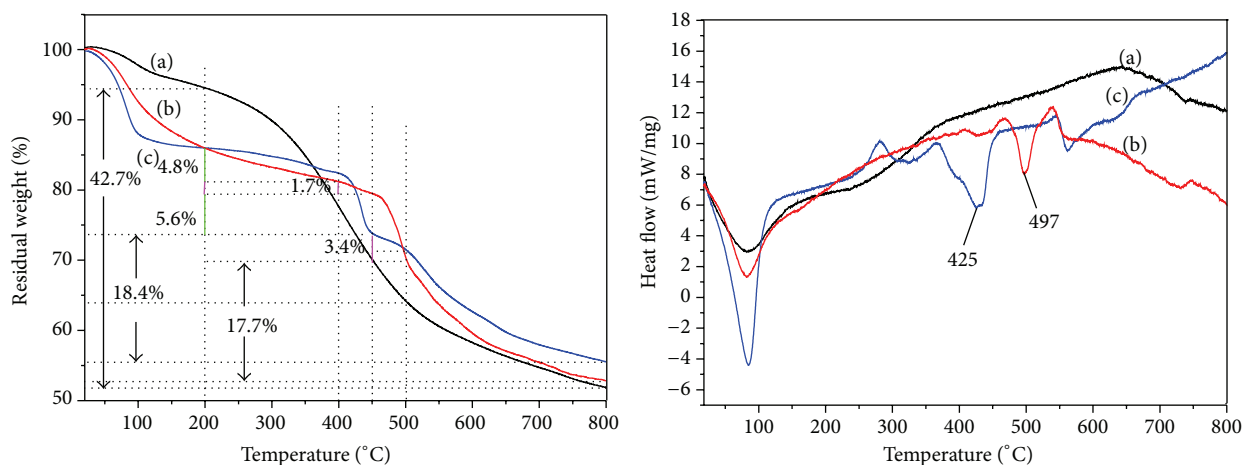


FIGURE 4: Thermal gravimetric analysis of (a) CS, (b) SPB, and (c) PSSNa.

the decomposition of PSSNa [26]. The main thermal decomposition starting at 425°C is attributed to the degradation of the polymer backbone.

As shown in Figure 4(b), the weight loss of SPB within the temperature range of 200 to 800°C is approximately 33.2%. A 9% weight loss occurs during the period from 450°C to 500°C. Compared with PSSNa, SPB exhibit higher thermal stability and the major degradation begins at 497°C. More energy is required, which suggests that the polymer has been bonded to azo initiator-immobilized carbon spheres. The weight of all grafted PSSNa brushes could be calculated from (1).

**3.5. Molecular Weight of the Brushes.** According to the previous work on similar systems, the molecular weight and its distribution of the brushes are about the same as those of the free polymers [27, 28]. Thus, the free polymers in the solution are collected and purified for GPC determination. Taking 0.1 M NaCl (aq) as mobile phase, PEG is used as the internal standard at room temperature. The free polymers have  $M_w$  of 393600 g/mol with polydispersity  $M_w/M_n$  of 1.58. The surface grafting density is  $8.38 \times 10^{-9} \mu\text{mol}/\text{nm}^2$  according to (2).

**3.6. Dependence of Brushes Thickness  $L$  on the Ionic Strength and pH.** The influence of the ionic strength on the swelling behavior of the SPB is investigated by DLS. Figure 5 represents the dependence of zeta potential and brushes thickness  $L$  on ionic strength. Here the thickness  $L$  can be obtained from the hydrodynamic radius  $R_h$  and the core radius  $R$  of the carbon spheres through  $L = R_h - R$  [17]. As illustrated in Figure 5, SPB are electrically charged in solution at low salt concentration and a stable dispersion of particles is obtained. Then an increase of salt concentration results in a decrease of absolute value of zeta potential (Figure 5(a)), as well as a decrease of  $L$  for both kinds of counterions (Figure 5(b)); moreover, divalent counterions lead to an even more drastic shrinking of brushes. As an increase of salt concentration, dispersions of SPB are no longer stable. The reason for this phenomenon is that the swelling of SPB is dominated by electrostatic repulsive force among the chains, and raising ionic strength by adding large amounts of salt, however, will screen electrostatic interaction and lead to the shrinking of brush layers. Similar results have been obtained in previous theoretical studies [29] and experimental studies [27, 30].

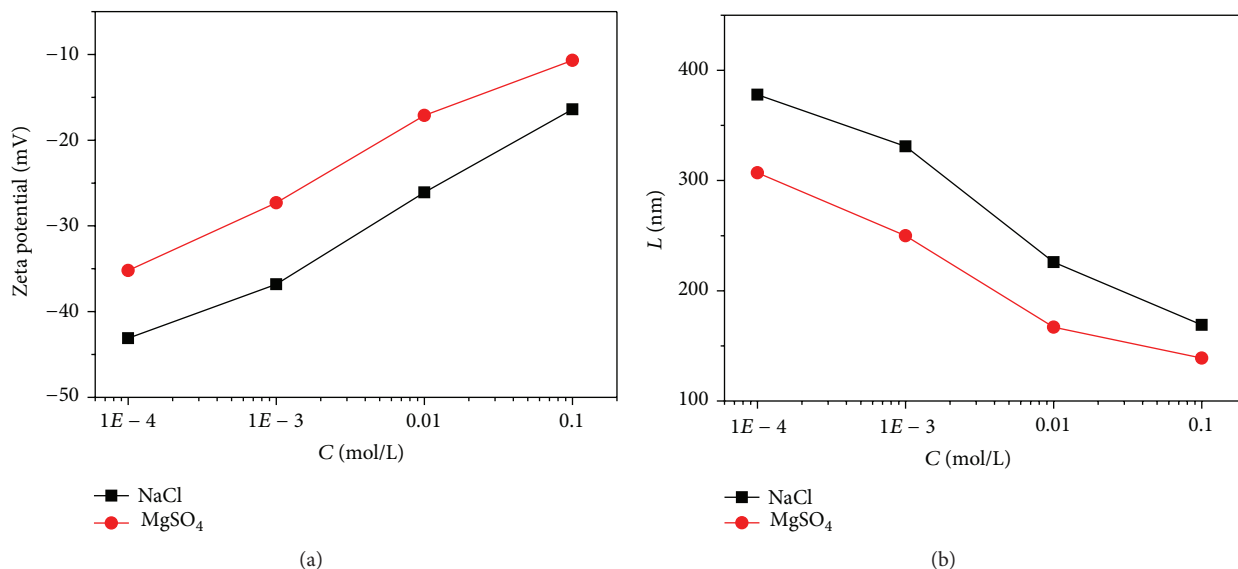


FIGURE 5: (a) Zeta potential and (b) thickness  $L$  of SPB as a function of different concentration of counterions in solution.

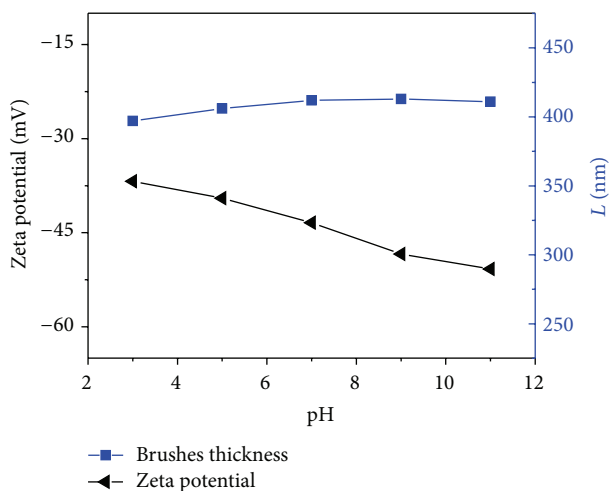


FIGURE 6: Zeta potential and thickness  $L$  of SPB as a function of different pH.

The zeta potential and thickness  $L$  of SPB in solution with different pH are shown in Figure 6. SPB are always electrical when the pH value of solution changes from 3 to 11 and the variation of zeta potential in the solution with different pH is small. It is also found that change of pH value has little effect on the thickness of brushes and SPB can be stably dispersed in the solution with different pH. The reason for this is that PSSNa is strong polyelectrolyte and can be completely ionized in solution; thus the change of pH of solution will not have an impact on the ionization [31].

#### 4. Conclusions

The SPB consisting of a carbon spheres core and a shell of PSSNa have been prepared successfully using a technique of “grafting from.” Different characterization methods demonstrate that synthesized SPB have well-defined morphology,

long polymer chains, and a narrow molecular weight distribution. The shrinking of brushes is sensitive to ionic strength for both monovalent and divalent counterions; moreover, divalent counterions lead to a more drastic shrinking. The change of pH of solution will not have an impact on the shrinking of brushes.

#### Conflict of Interests

The authors declare that there is no conflict of interests regarding the publication of this paper.

#### Acknowledgments

This work is supported by Innovation Program of Shanghai Municipal Education Commission (15ZZ112) and National Natural Science Foundational of China (31170558).

## References

- [1] M. Ballauff and O. Borisov, "Polyelectrolyte brushes," *Current Opinion in Colloid and Interface Science*, vol. 11, no. 6, pp. 316–323, 2006.
- [2] J. Chen, P. Xiao, J. Gu et al., "A smart hybrid system of Au nanoparticle immobilized PDMAEMA brushes for thermally adjustable catalysis," *Chemical Communications*, vol. 50, no. 10, pp. 1212–1214, 2014.
- [3] Y. Lu, A. Wittmann, and M. Ballauff, "Supramolecular structures generated by spherical polyelectrolyte brushes and their application in catalysis," *Macromolecular Rapid Communications*, vol. 30, no. 9–10, pp. 806–815, 2009.
- [4] X. Lu, R. Jiang, M. Yang et al., "Monodispersed grafted conjugated polyelectrolyte-stabilized magnetic nanoparticles as multifunctional platform for cellular imaging and drug delivery," *Journal of Materials Chemistry B*, vol. 2, no. 4, pp. 376–386, 2014.
- [5] F. Xu, J. H. Geiger, G. L. Baker, and M. L. Bruening, "Polymer brush-modified magnetic nanoparticles for his-tagged protein purification," *Langmuir*, vol. 27, no. 6, pp. 3106–3112, 2011.
- [6] Y. Mei, C. Abetz, O. Birkert, V. Schädler, R. J. Leyrer, and M. Ballauff, "Interaction of spherical polyelectrolyte brushes with calcium carbonate and cellulose fibers: mechanistic studies and their application in papermaking," *Journal of Applied Polymer Science*, vol. 102, no. 1, pp. 233–241, 2006.
- [7] A. N. Korovin, V. G. Sergeev, O. A. Pyshkina, and L. Tsarkova, "Spherical polyelectrolyte brushes as templates for stable dispersions of polyaniline based conducting particles," *Macromolecular Symposia*, vol. 317–318, no. 1, pp. 137–141, 2012.
- [8] A. Malinauskas, "Chemical deposition of conducting polymers," *Polymer*, vol. 42, no. 9, pp. 3957–3972, 2001.
- [9] Y. Huang, X. Zhang, X. Huang, H. Li, and C. Huang, "Preparation of conductive polypyrrole composite particles based on spherical polyelectrolyte brushes," *Materials Express*, vol. 5, no. 1, pp. 56–62, 2015.
- [10] Y. Lu, Y. Mei, R. Walker, M. Ballauff, and M. Drechsler, "'Nanotree'-type spherical polymer brush particles as templates for metallic nanoparticles," *Polymer*, vol. 47, no. 14, pp. 4985–4995, 2006.
- [11] Y. D. Xia and R. Mokaya, "Ordered mesoporous carbon hollow spheres nanocast using mesoporous silica via chemical vapor deposition," *Advanced Materials*, vol. 16, no. 11, pp. 886–891, 2004.
- [12] R. Alcántara, P. Lavela, G. F. Ortiz, and J. L. Tirado, "Carbon microspheres obtained from resorcinol-formaldehyde as high-capacity electrodes for sodium-ion batteries," *Electrochemical and Solid-State Letters*, vol. 8, no. 4, pp. A222–A225, 2005.
- [13] H.-S. Qian, F.-M. Han, B. Zhang, Y.-C. Guo, J. Yue, and B.-X. Peng, "Non-catalytic CVD preparation of carbon spheres with a specific size," *Carbon*, vol. 42, no. 4, pp. 761–766, 2004.
- [14] Y. Z. Jin, C. Gao, H. W. Kroto, and T. Maekawa, "Polymer-grafted carbon spheres by surface-initiated atom transfer radical polymerization," *Macromolecular Rapid Communications*, vol. 26, no. 14, pp. 1133–1139, 2005.
- [15] Q. Wang, X. Liang, W. Qiao et al., "Modification of polystyrene-based activated carbon spheres to improve adsorption of dibenzothioophene," *Applied Surface Science*, vol. 255, no. 6, pp. 3499–3506, 2009.
- [16] Q. Zhang, H. B. Li, P. Zhang, Y. He, and Y. Wang, "Surface modification and characterization of carbon spheres by grafting polyelectrolyte brushes," *Nanoscale Research Letters*, vol. 9, article 283, 2014.
- [17] N. Su, H. B. Li, H. M. Zheng, S. P. Yi, and X. H. Liu, "Synthesis and characterization of poly(sodium-p-styrenesulfonate)/modified SiO<sub>2</sub> spherical brushes," *eXPRESS Polymer Letters*, vol. 6, no. 8, pp. 680–686, 2012.
- [18] N. Su and Z. M. Cao, "Preparation and characterization of poly(dimethyl diallyl ammonium chloride)/modified SiO<sub>2</sub> spherical brushes," *Applied Mechanics and Materials*, vol. 731, pp. 569–572, 2015.
- [19] H. Zhang and J. Rühle, "Interaction of strong polyelectrolytes with surface-attached polyelectrolyte brushes-polymer brushes as substrates for the layer-by-layer deposition of polyelectrolytes," *Macromolecules*, vol. 36, no. 17, pp. 6593–6598, 2003.
- [20] J.-Y. Miao, D. W. Hwang, K. V. Narasimhulu et al., "Synthesis and properties of carbon nanospheres grown by CVD using Kaolin supported transition metal catalysts," *Carbon*, vol. 42, no. 4, pp. 813–822, 2004.
- [21] Y. Ma, Z. Hu, K. Huo et al., "A practical route to the production of carbon nanocages," *Carbon*, vol. 43, no. 8, pp. 1667–1672, 2005.
- [22] X. Sun and Y. Li, "Colloidal carbon spheres and their core/shell structures with noble-metal nanoparticles," *Angewandte Chemie*, vol. 43, no. 5, pp. 597–601, 2004.
- [23] A. N. Korovin, V. G. Sergeev, O. A. Pyshkina et al., "Nanoreactor-assisted polymerization toward stable dispersions of conductive composite particles," *Macromolecular Rapid Communications*, vol. 32, no. 5, pp. 462–467, 2011.
- [24] Y. Zhang, J. Zhang, Y. Zhong et al., "Direct fabrication of organic carbon coated VO<sub>2</sub>(B) (VO<sub>2</sub>(B)@C) core-shell structured nanobelts by one step hydrothermal route and its formation mechanism," *Applied Surface Science*, vol. 263, pp. 124–131, 2012.
- [25] Q. Zhao, J. Qian, Q. An, and B. Du, "Speedy fabrication of free-standing layer-by-layer multilayer films by using polyelectrolyte complex particles as building blocks," *Journal of Materials Chemistry*, vol. 19, no. 44, pp. 8448–8455, 2009.
- [26] X. Xiao, R. Liu, F. Liu, X. Zheng, and D. Zhu, "Effect of poly(sodium 4-styrene-sulfonate) on the crystal growth of hydroxyapatite prepared by hydrothermal method," *Materials Chemistry and Physics*, vol. 120, no. 2–3, pp. 603–607, 2010.
- [27] H. Zhang and J. Rühle, "Swelling of poly(methacrylic acid) brushes: influence of monovalent salts in the environment," *Macromolecules*, vol. 38, no. 11, pp. 4855–4860, 2005.
- [28] G. K. Raghuraman, J. Rühle, and R. Dhamodharan, "Grafting of PMMA brushes on titania nanoparticulate surface via surface-initiated conventional radical and 'controlled' radical polymerization (ATRP)," *Journal of Nanoparticle Research*, vol. 10, no. 3, pp. 415–427, 2008.
- [29] M. Biesalski and J. Rühle, "Scaling laws for the swelling of neutral and charged polymer brushes in good solvents," *Macromolecules*, vol. 35, no. 2, pp. 499–507, 2002.
- [30] X. Guo and M. Ballauff, "Spherical polyelectrolyte brushes: Comparison between annealed and quenched brushes," *Physical Review E*, vol. 64, no. 5, 2001.
- [31] T. Isojima, M. Lattuada, J. B. V. Sande, and T. A. Hatton, "Reversible clustering of pH- and temperature-responsive Janus magnetic nanoparticles," *ACS Nano*, vol. 2, no. 9, pp. 1799–1806, 2008.

## Research Article

# Temperature Effect on Electrical Treeing and Partial Discharge Characteristics of Silicone Rubber-Based Nanocomposites

Mohd Hafizi Ahmad,<sup>1</sup> Nouruddeen Bashir,<sup>1</sup> Zolkafle Buntat,<sup>1</sup> Yanuar Z. Arief,<sup>1</sup>  
Abdul Azim Abd Jamil,<sup>2</sup> Mohamed Afendi Mohamed Piah,<sup>1</sup> Abubakar A. Suleiman,<sup>1</sup>  
Steve Dodd,<sup>3</sup> and Nikola Chalashkanov<sup>3</sup>

<sup>1</sup>*Institute of High Voltage and High Current, Faculty of Electrical Engineering, Universiti Teknologi Malaysia, 81310 Johor Bahru, Johor, Malaysia*

<sup>2</sup>*School of Electronics and Electrical Engineering, Universiti Sains Malaysia, 14300 Nibong Tebal, Penang, Malaysia*

<sup>3</sup>*Department of Engineering, University of Leicester, Leicester LE1 7RH, UK*

Correspondence should be addressed to Mohd Hafizi Ahmad; [mohdhafizi@fke.utm.my](mailto:mohdhafizi@fke.utm.my)

Received 27 April 2015; Accepted 28 June 2015

Academic Editor: Mircea Chipara

Copyright © 2015 Mohd Hafizi Ahmad et al. This is an open access article distributed under the Creative Commons Attribution License, which permits unrestricted use, distribution, and reproduction in any medium, provided the original work is properly cited.

This study investigated electrical treeing and its associated phase-resolved partial discharge (PD) activities in room-temperature, vulcanized silicone rubber/organomontmorillonite nanocomposite sample materials over a range of temperatures in order to assess the effect of temperature on different filler concentrations under AC voltage. The samples were prepared with three levels of nanofiller content: 0% by weight (wt), 1% by wt, and 3% by wt. The electrical treeing and PD activities of these samples were investigated at temperatures of 20°C, 40°C, and 60°C. The results show that the characteristics of the electrical tree changed with increasing temperature. The tree inception times decreased at 20°C due to space charge dynamics, and the tree growth time increased at 40°C due to the increase in the number of cross-link network structures caused by the vulcanization process. At 60°C, more enhanced and reinforced properties of the silicone rubber-based nanocomposite samples occurred. This led to an increase in electrical tree inception time and electrical tree growth time. However, the PD characteristics, particularly the mean phase angle of occurrence of the positive and negative discharge distributions, were insensitive to variations in temperature. This reflects an enhanced stability in the nanocomposite electrical properties compared with the base polymer.

## 1. Introduction

Polymeric materials are gaining prominence among utilities as their preferred insulating materials for underground power cables largely due to their high dielectric strength (in MV/cm), very low dielectric losses, high tensile strength, and resistance to electrical degradation [1]. Power cables are subjected to high and continuous voltage as well as mechanical and thermal stresses that induce and accelerate the cable ageing and insulation breakdown. Electrical treeing is one such breakdown phenomenon that occurs in insulation cables, and many researchers have presented studies done on electrical treeing phenomena in insulation cables [2–7]. Treeing occurs inside the dielectric when partial discharges are initiated and progresses under electrical stress through

paths that are tree-like. To curb the growth of the electrical tree, many researchers have used microcomposite materials as fillers to enhance the electrical and mechanical strength of the polymer. However, the increasing demand for power and further research has led to the discovery and use of nanocomposite polymers with the addition of nanofillers due to their excellent performance [8–10]. One such nanocomposite that is currently receiving attention as a nanofiller in HV cable insulation is organomontmorillonite (oMMT). Results from the use of oMMT as a nanofiller in ethylene-vinyl acetate, low-density polyethylene, polyethylene (PE), and epoxy resin have shown improvement in the electrical performance of these insulating materials, such as increases in tree inception voltage, tree initiation time, and time to breakdown and slower tree propagation [11–14].

In power cables, silicone rubber (SiR) is one of the most widely used insulating materials for cable stress cones, jointing, and insulation materials [15–18]. Recently, some electrical treeing studies that investigated the electrical performance of SiR filled with oMMT nanofiller as an insulating material have reported promising results [19–23]. Furthermore, most of the power cables in service operate at temperatures in the range of 50°C to 60°C [24, 25]. However, studies carried out on SiR/oMMT nanocomposites were limited to those on the effect of filler content on the performance of the insulation at ambient temperature. And thus electrical treeing associated with partial discharge studies on the effect of temperature on SiR/oMMT nanocomposites are lacking. In view of the foregoing, this work presents an investigation on the effect of temperature on electrical treeing and partial discharge characteristics of silicone rubber-based nanocomposite insulation. Findings from this study indicated that temperature and filler concentrations have effect on electrical treeing and partial discharge characteristics of polymeric insulation.

## 2. Nanoclay

Nanoclay belongs to the family of phyllosilicates, which are also known as layered silicates. Nanoclay is classified into four typical groups: smectite, kaolin, chlorite, and illite. Montmorillonite belongs to the smectite group. The layered silicate crystal lattice consists of a two-dimensional, sheet-like structure, where the central octahedral of the alumina sheet or magnesia is placed between two silica tetrahedron sheets. The oxygen ions of the octahedral sheet are shared by both the octahedral sheet and the tetrahedral sheet, while the gallery or interlayer region is formed by Van der Waals forces that hold the layers together. Isomorphic substitution within the layers will generate negative charges, which will be counterbalanced by alkali and alkaline earth cations inside the galleries [27]. The thickness of the layers is of the order of 1 nm. Thus, the clay layers are truly nanoparticulate. Based on information in the literature [27], the original layer silicates can only be dispersed in hydrophilic polymers, such as polyvinyl alcohol and polyethylene oxide. Thus, the normally or naturally hydrophilic layer silicates should be modified to become organophilic so that they can be more compatible with other polymer matrices. As a result, the exfoliation and intercalation of various polymers can be achieved.

Various modification methods are being used in the production of organically modified nanoclay. Early methods used amino acids [28]; however, primary, secondary, tertiary, or quaternary alkyl-ammonium cations were subsequently and widely used because they can be changed easily with the ions located between the layers. Alkyl-ammonium cations can provide sufficient functional groups that can react with the polymer matrix, thereby starting monomer polymerisation and enhancing the strength of the interface. The alkyl-ammonium cations also expand the clay galleries (interlayer spacing) due to reduced surface energy, and consequently the polymer chains can penetrate the clay gallery space or be intercalated into the galleries [29].

There are three possible structures of polymer/layered silicate, and this depends on the types of the layered silicate,

organic modifier, polymer matrix, and method of polymer nanocomposites preparation. The nanocomposite is said to be agglomerated when the polymer matrix is not able to expand and unable to cover the distances between the interlayer galleries and also unable to expel tactoids from the polymer to form microcomposites. The exfoliated or delaminated polymer nanocomposite is achieved when the individual silicate layers are uniformly dispersed in a continuous polymer matrix by an average distance. The intercalated structure is achieved when a single extended polymer chain is intercalated between the silicate layers, which results in a well-ordered multilayer [29].

A modified version of the montmorillonite nanoclay type is oMMT or organoclay. The modification of the montmorillonite nanoclay to an organoclay alters it, organically making the oMMT more organophilic and compatible with hydrophobic materials, such as silicone rubber, epoxy resin, and PE. Organoclays are reported to have charge carrier trapping properties (electronegative), provide an improved balance of stiffness and toughness, possess flame retardant properties that offer a reduction in relative heat release, and reduce dripping by forming char. They are also cheaper than other nanomaterials because they are produced in existing full-scale production facilities and because their basic materials come from readily available natural sources [13, 30].

## 3. Experimental Technique

**3.1. Sample Preparation.** The silicone rubber (SiR) used in this study was *Sylgard 184* silicone elastomer which comes together with dimethyl, methylhydrogen siloxane as a hardener. Meanwhile, the oMMT used in this study was Nanomer 1.30P supplied by Nanocor Inc., USA. A detailed description on the materials, method used to prepare the organomontmorillonite by adding octadecylamine and concentrated hydrochloric acid, and also leaf-like sample preparation can be found in [17, 28] and [29], respectively.

**3.2. Dispersion and Characterization Study.** Dispersion of the nanoparticles inside the investigated materials was observed under a Carl Zeiss Supra 35 Field Emission Scanning Electron Microscope (FESEM), which is an ultrahigh-resolution microscope. Prior to FESEM observation, each fractured surface of nanocomposite sample was sputter-coated with a thin layer of platinum using a Bio-Rad sputter coater under vacuum pressure for one minute at 20 mA and 1.6 kV to provide electrical conductivity. The nanocomposite samples were then examined at 10 kV of acceleration voltage. In addition, the dispersion of nanofiller inside the silicone rubber material was also observed by 200 kV high-resolution transmission electron microscope (HRTEM). The sample was sliced into excellent quality ultrathin 200 nm thick slices by using a Leica EM FC7 cryoultramicrotome.

A Fourier transform infrared spectrometer (FTIR) was used to identify the functional groups on the surface and in the bulk of the used filler and in the polymer-based nanocomposite samples. These functional groups help to

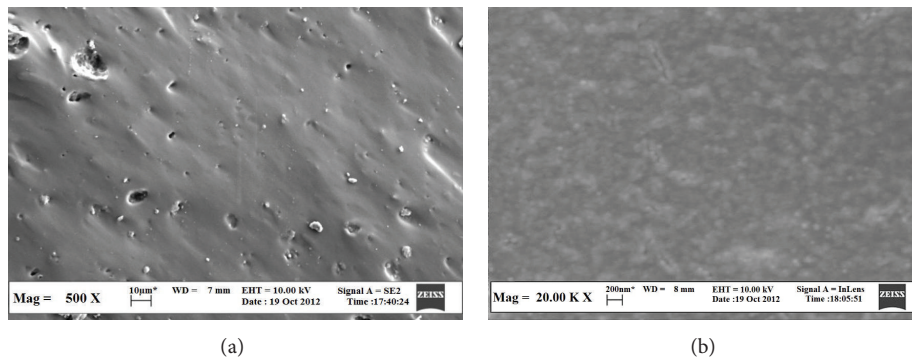


FIGURE 1: FESEM images of fractured surfaces for silicone rubber-based nanocomposites: (a) 1 wt% and (b) 3 wt%.

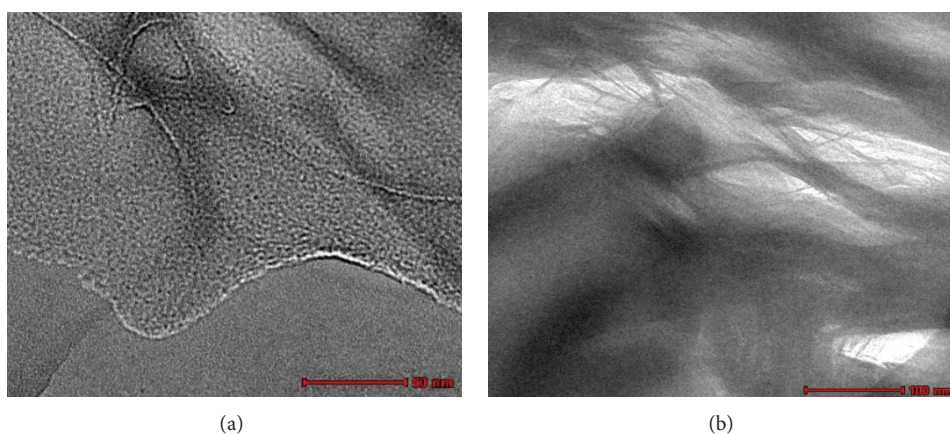


FIGURE 2: TEM micrographs of silicone rubber-based nanocomposites: (a) 1 wt% and (b) 3 wt%.

clarify the interaction between the nanofiller and the polymer (silicone rubber) at the interface of the nanocomposites. A Perkin Elmer FTIR spectrometer was used to obtain the IR spectra. The polymer specimens were analysed at  $1\text{ cm}^{-1}$  resolution, and 16 scans were averaged in the transmittance mode at wavelengths in the range of  $370\text{--}4000\text{ cm}^{-1}$ . The nanofillers were pressed with potassium bromide (KBr) at a pressure of 6 bars to form a thin film disc for FTIR measurements. The thin film disc was then placed in a sample cap of diffuse reflectance fitment. Before the FTIR preparation, the oMMT nanofiller and the sample of silicone rubber-based nanocomposites were dried at  $105^\circ\text{C}$  for more than 48 hours to ensure removal of all moisture for the FTIR analysis. The spectra were analysed via the software provided with the instrument.

**3.3. Experimental Procedure.** The electrical treeing-PD test rig consists of a step-up transformer, fibre optic transmitter and receiver, high voltage supply, Peltier cooled Charged Couple Device (CCD) camera with back illumination, light emitting diode (LED), digital storage oscilloscope, temperature controller with cartridge heater, specimen holder, glass test cell, RLC load circuit, and personal computer. A detailed description of the test rig and experimental procedure using the test rig can be found in [29–31].

## 4. Results and Discussion

**4.1. Nanofiller Dispersion via FESEM.** The FESEM and TEM images are depicted in Figures 1 and 2, respectively. These visual analyses were able to characterize and clarify the dispersion, degree, and homogeneity of agglomeration of the nanoparticles into the nanocompounds. Under a magnification of 500 times, several tactoids were visible and can be seen in Figure 1(a) where the agglomerated nanoparticle sizes are larger than  $100\text{ nm}$ ; the nanoparticle sizes in Figure 1(b) are smaller and less than  $100\text{ nm}$ .

**4.2. Electrical Treeing, PD, and Effect of Temperature.** All the electrical trees were noted to have grown below an estimated electrical tree inception voltage of  $10\text{ kVrms}$  at  $50\text{ Hz}$ . Images of the light emitted from PD within the tree channels that were recorded before voltage was removed at the end of each experiment are shown in Figures 3 and 4. These composite images of light emission are due to the partial discharge activity (grey scale) superimposed on the back-illuminated images (red/black) of the tree structure. These images show the spatial extent of the PDs within the tree channel that formed. All trees formed were found to have a branched structure.

In the case of neat resin samples ( $0\text{ wt\% oMMT}$ ), the tree inception time was found to have decreased with increase in

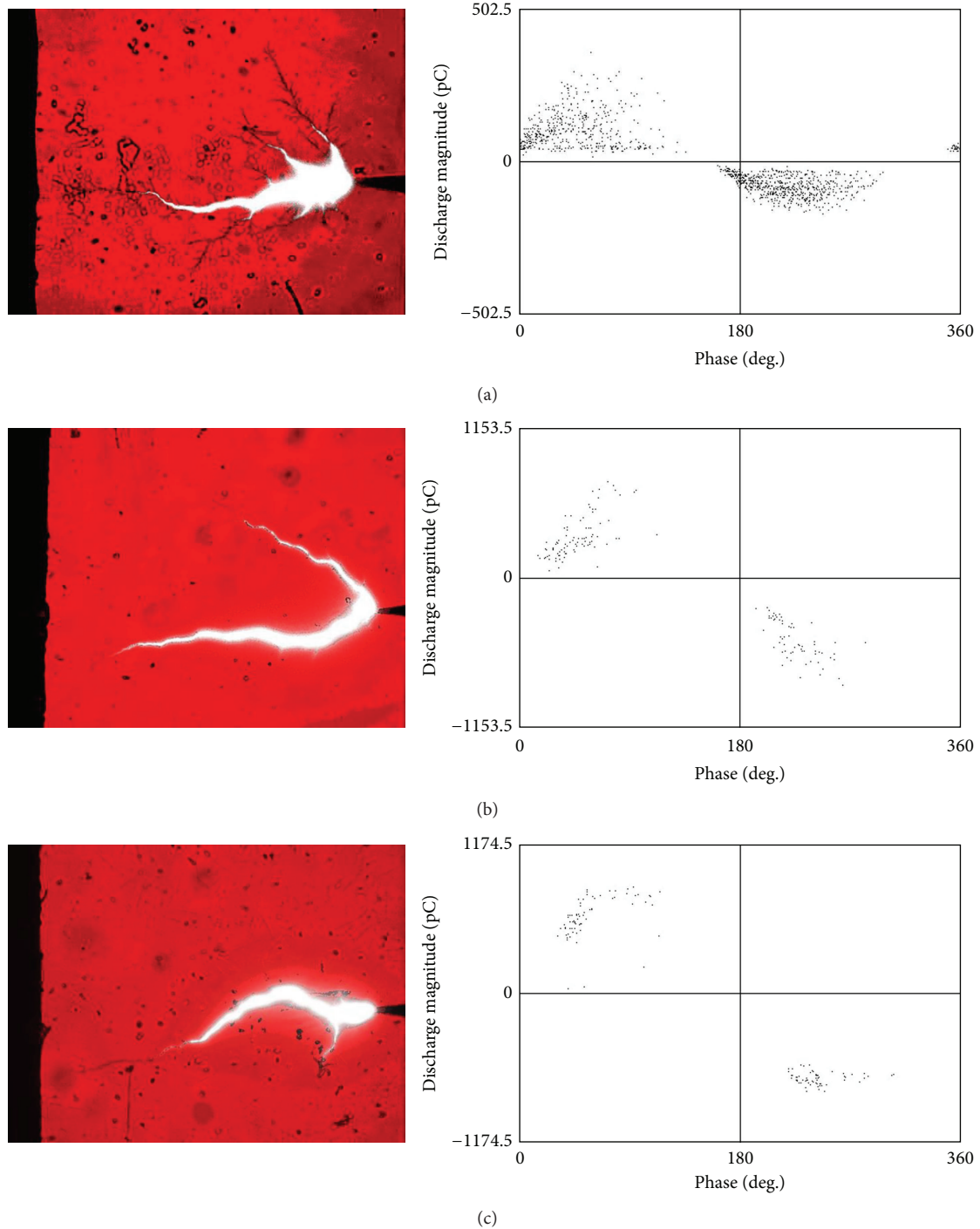


FIGURE 3: Electrical treeing associated with the PD phase-resolved patterns of neat silicone rubber: (a) at 20°C, (b) at 40°C, and (c) at 60°C.

temperature from 19 seconds at 20°C to 5 seconds at 60°C. In contrast, the tree growth time required for the tree to grow approximately 95% of the pin-edge distance increased from 80 seconds at 20°C to approximately 29 minutes at 60°C. The tree initiation process starts from injection and extraction of space charges in which the charge carrier dynamics depend significantly on temperature as these processes are mostly thermally activated mechanisms [32]. Thus, the increase in

temperature enhances the dynamics of the space charge, reducing the tree initiation time. In addition, the increase in temperature gives rise to an increase in the number of cross-link network structures caused by the vulcanization process. This results in more trapping sites for charge carriers where the charge carriers get trapped around the boundary of the polymer chains, reducing the charge carrier mobility. This slows down the growth of the electrical tree due to

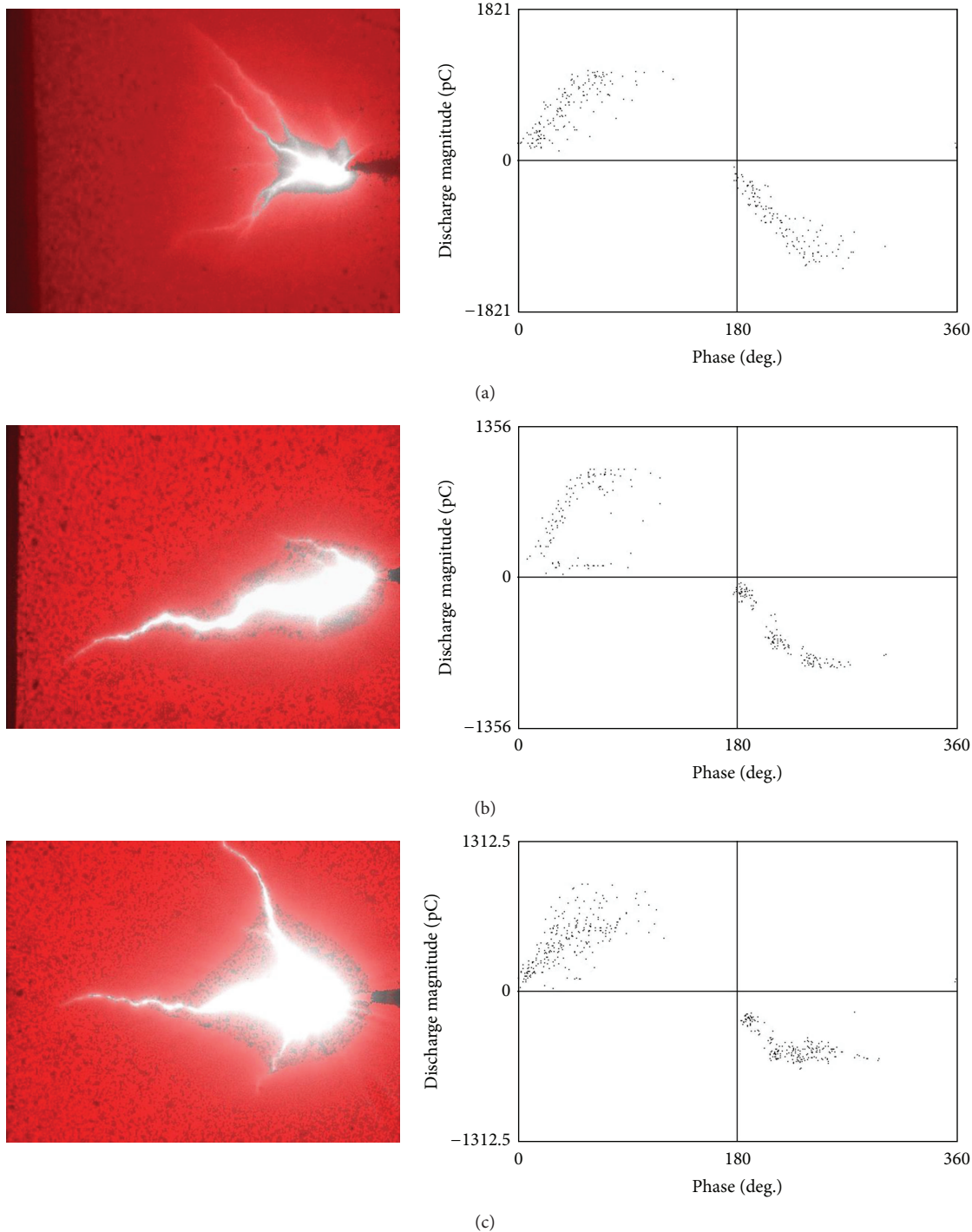


FIGURE 4: Electrical treeing associated with the PD phase-resolved patterns of silicone rubber-based nanocomposite (1 wt%): (a) at 20°C, (b) at 40°C, and (c) at 60°C.

more time and energy required to detrapp the charge carriers for conduction. In addition, the increase in the number of cross-link networks also creates a more rigid polymer with an immobilized polymer chain. Consequently, more energy and time are required to break the bond to create a void or cavity, which eventually generates PD and causes the growth of electrical treeing.

In the case of the 1wt% oMMT nanocomposites, the inception time first increased and then decreased with increasing temperature. The registered tree inception times were 20 seconds, 100 seconds, and 83 seconds at 20°C, 40°C, and 60°C, respectively. Nevertheless, the addition of nanofiller enhanced the tree initiation time even though the temperatures increased. As mentioned before, the space

charge dynamics were enhanced by increasing the temperature. However, the effect of temperature on space charges in silicone rubber-based nanocomposites was not obvious since the addition of nanoparticles trapped the charge carriers around or inside the particles. Thus, these trapped charge carriers require high energy to move from one trap to another trap or to get extracted from the polymer. This results in a slower degradation rate and more time for tree initiation.

The tree growth times were significantly higher for the 1 wt% oMMT nanocomposite samples than for the neat silicone rubber samples. The tree growth times were found to increase from 10 minutes at 20°C to 46 minutes at 60°C due to the promotion of more cross-link networks as trapping sites. Moreover, the trapping sites were also enhanced due to the inclusion of nanoparticles. Thus, the injected and accumulated space charges were unable to drift or detrapp since most of the space charges were trapped at the polymer chains and around or inside the nanoparticle. This resulted in more energy and time being needed for space charges to cause electrical tree propagation, thus prolonging the electrical growth time.

The initiation of a tree is a sign of initial conduction in the dielectric. Since conductivity is proportional to the elementary charge, carrier density, and carrier mobility [33], reduction of conductivity is presumably due to the capture of mobile carriers at polymer/filler interfaces. In silicone rubber-based nanocomposites material (3 wt%), the large total interfacial areas contribute to increasing the trapping probability of charge carriers. The increase of charge trap areas/sites leads to a reduction in charge mobility, which in turn reduces conduction. The trapping probability was also enhanced due to the vulcanization process, which made the nanocomposites more rigid; consequently, more energy and time were required for polymer decomposition. However, due to insufficient field energy, the trapped charge carriers (electrons and holes) combine at the recombination centre and emit the photon that is responsible for light emission. Therefore, in the case of the 3 wt% oMMT nanocomposites, no tree inception was observed; even after 4 hours of voltage application, only weak light emission and sporadic PDs were recorded.

By comparing the effect of the nanofiller at individual temperatures, we can note and justify the advantages or benefits and reinforcement properties of adding the nanofiller. At a low temperature of 20°C, the tree inception time of silicone rubber nanocomposite (1 wt%) was almost similar to the corresponding neat silicone rubber. This insensitive characteristic was due to the agglomeration in the nanocomposite sample (1 wt%) as seen in the FESEM image in Figure 1(a). In addition, the TEM micrograph in Figure 2(a) shows that the clay silicate layers do not maintain their original parallel layers with a scattered layered structure. Thus, agglomeration nullifies the capability of electrical tree initiation resistance of nanoparticles, resulting in insensitive parameters. However, the increase in filler loading increased the growth time of electrical treeing due to the trapping of charge carriers.

When the temperature was increased to 40°C, tree inception time and tree growth time increased with increases in filler loading from 0 wt% to 3 wt%. These enhancements in

electrical tree resistance result from the increase in the charge carrier trapping density and also from the increase in cross-link network structures. These changes result in difficulty in initiating an electrical tree since more field energy is needed to enhance growth.

More enhanced and reinforced properties of silicone rubber-based nanocomposites are noticed at a temperature of 60°C. This postcure temperature promoted more cross-link network structures, thereby contributing to the formation of a more rigid polymer. This enhancement leads to an increase in electrical tree inception time and electrical tree growth time since nanofillers act as trapping sites and potential physical barriers to the growth of an electrical tree in the direction of the electric field.

The composite CCD images shown in Figures 3, 4, and 5 demonstrate that, for all samples in which trees grew, the PDs occur throughout the main body of the tree structure. This indicates that the tree channels were effectively electrically nonconducting, such that a sufficient potential difference could exist along the tree channels to initiate PDs within them. In addition to the composite images captured, the phase-resolved PD patterns were also recorded. Generally, the PD pulses mainly occurred in the first and third quadrants of the voltage waveform.

The results of the phase-resolved PD data are shown in Table 1. In the case of neat SiR, the average PD magnitude was found to increase with increase in temperature while the average number of PDs per second was found to decrease with increase in temperature. A significant shift in the average phase of PD occurrence of both the positive and negative discharge distributions took place simultaneously. The average phase of occurrence of the positive PDs increased from 37° at 20°C to 55° at 60°C. Similar dependence on temperature of the PD phases was found for electrical tree growth in the flexible epoxy resin. This phase shift is attributed to an increase in the electrical conductivity of the epoxy resin with increasing temperature, leading to decreased accumulation of the space charge surrounding the tree structure.

However, the reverse situation has been reported for an epoxy resin sample; that study showed PD numbers increasing and PD magnitudes decreasing with increasing temperature from 20°C to 70°C [34]. This dissimilarity between epoxy resin and silicone rubber is probably due to the increase in vulcanization/cross-link numbers in silicone rubber matrices with increasing temperature; this has been discussed thoroughly by Du et al. [15, 35].

In the case of the 1 wt% oMMT nanocomposite, the average PD magnitude was found to decrease with increasing temperature from 450 pC at 20°C to 257 pC at 60°C. However, the other three PD physical parameters remained relatively insensitive to the changes in temperature. The decrease in PD magnitude when the temperature increased in silicone rubber-based nanocomposites (1 wt%) is because the addition of nanoparticles contributes to the trapping of space charges; in this process, the electrons injected from the electrode move towards the opposite electrode and are trapped at the nanoparticle surfaces and inside the nanoparticles. When the applied field is sufficiently high, it can cause ionization of the nanoparticle within the polymer. Thus, an internal field will

TABLE I: Summary of partial discharge statistical parameters.

Type of sample	PD characteristics	20°C			40°C			60°C		
		Min	Max	Ave.	Min	Max	Ave.	Min	Max	Ave.
Neat SiR	Discharge magnitude (pC)	83	218	160	57	387	280	70	610	332
	Number of PDs (s <sup>-1</sup> )	687	1244	952	117	7571	199	65	649	197
	Phase of occurrence of positive PDs (°)	34	41	37	36	60	44	44	93	55
	Phase of occurrence of negative PDs (°)	215	220	218	218	244	226	223	247	239
	Dissipated power (mW)	0.87	1.40	1.24	0.35	3.4	0.54	0.05	0.997	0.668
SiR/1 wt % oMMT	Discharge magnitude (pC)	31	641	450	5	492	294	137	478	257
	Number of PDs (s <sup>-1</sup> )	249	1831	495	1	581	338	416	831	580
	Phase of occurrence of positive PDs (°)	33	86	44	36	61	47	34	44	38
	Phase of occurrence of negative PDs (°)	209	275	223	209	274	217	212	225	217
	Dissipated power (mW)	0.22	3.50	1.91	0.061	1.5	0.94	0.75	2.00	1.395
SiR/3 wt % oMMT	Discharge magnitude (pC)	2	45	22	2	6	4	2	11	4
	Number of PDs (s <sup>-1</sup> )	1	643	181	1	64	27	1	25	4
	Phase of occurrence of positive PDs (°)	17	142	80	5	94	46	52	133	75
	Phase of occurrence of negative PDs (°)	154	306	280	177	272	226	164	265	222
	Dissipated power (μW)	0.34	163	35.7	0.002	3.7	1.13	0.03	0.98	0.15

be created to oppose the direction of the applied field, making the net field inside the nanoparticle greater than the discharge inception field and thereby extinguishing the discharge. This reduces the PD magnitude. If the applied field is high enough and exceeds the internal field, the discharge will occur again. However, the particles tend to agglomerate, resulting in the less interfacial area and leading to lesser charge carriers getting trapped around the particle surfaces (localized states). Due to repetition and a sufficiently high electric field, the trap sites provided by microparticles for electron localizations are not sufficient and so lead to electron drift (detrapping). This causes charge movements (mobility) that give a higher PD repetition rate. As a result, agglomeration nullifies the capability of PD resistance of the nanoparticles.

The addition of 3 wt% oMMT nanoparticles in silicone rubber caused electrical tree inhibition; no electrical trees were observed during the time span of the experiment (4 hours at 10 kVrms, 50 Hz). Only localized light emission, recognized as electroluminescence, was detected at the needle tip when using the CCD camera. It appears that the SiR matrices were reinforced by the addition of 3 wt% oMMT nanofillers to an extent that prevented the formation of an initial void with a sufficient dimension required for PD generation and subsequent electrical tree initiation. The PD magnitudes and PD numbers decreased with the increase in temperature from 20°C to 60°C; the PD magnitudes decreased from 22 pC to 4 pC. However, the phase of positive PDs was found to be insensitive to temperature changes, whereas the phase of negative PDs shifted to the lower values with the increase in temperature.

Based on FESEM images in Figure 1(b), the nanofillers were distributed uniformly with sizes less than 100 nm. The micrograph in Figure 2(b) shows that the oMMT was in the form of incompletely exfoliated mixed intercalation, indicating that the silicate layers were uniformly separated as the particles were quite long in length. The TEM image

in Figure 2(b) shows that the nanocomposite material containing oMMT particles differed from the form shown in the FESEM image of Figure 1(b). However, the oMMT particles still maintained the parallel layered structures even though the gap increased.

Thus, oMMT possesses the advantages of nanoparticles, such as a large interfacial area (surface area) that allows large charge carrier trapping, charge dissipation due to recombination, electron scattering, large interaction zones, and a proximity effect [36]. These properties reduce the charge mobility and energy needed for conduction, thereby reducing PD magnitudes, PD numbers, and other PD parameters. The charge carriers are unable to move (drift) due to insufficient kinetic energy and remain at the electrode tip; most are dissipated by electron-hole recombination, which releases energy (photon) in the form of light.

Moreover, the small discharges detected in the nanocomposites material were probably swarming partial microdischarges (SPMD); this is related to the existence of microvoids at the polymer/electrode interface due to imperfect bonding between the tungsten needle and the silicone rubber. Tanaka [37] reported that small PDs of less than 1 pC were detected in a void prior to tree initiation. SPMD phenomena can be found in [38–40]. Thus, the detection of PD prior to tree initiation may have been caused by the microvoids at the needle tip due to charge carrier recombination. The holes and electrons were injected into the polymer during the positive and negative half-cycle of the AC voltage and were trapped in the recombination centres. Light is emitted when the electron-hole recombination occurs at the luminescent centre [41]. However, the electric field intensity was insufficient to initiate electrical treeing due to low energy.

In polymer nanocomposites, the nanoparticles act as charge carrier trap with high barrier potentials. These trapped carriers need more energy to get extracted from one trap to another trap. This would slow down the growth of electrical

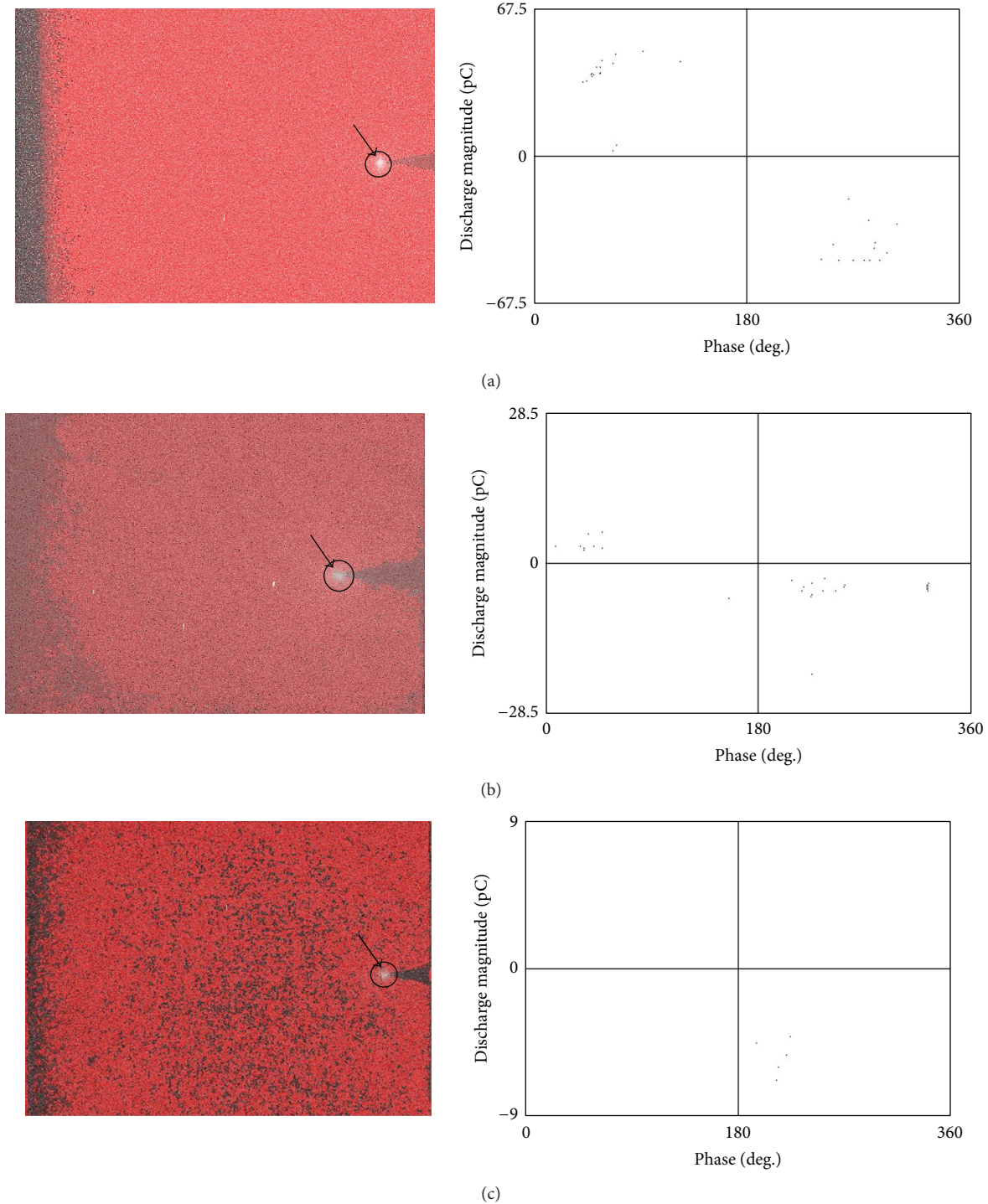


FIGURE 5: Electrical treeing associated with the PD phase-resolved patterns of silicone rubber-based nanocomposite (3 wt%): (a) at 20°C, (b) at 40°C, and (c) at 60°C; arrows indicate weak light emissions.

treeing [42]. With the addition of 1 wt% oMMT nanofillers, tree inception time and propagation time were distinctly enhanced. However, PD magnitudes and PD numbers of silicone rubber-based nanocomposite (1 wt%) became insensitive with the increase in temperature as evidenced by the PD magnitudes being higher than neat silicone rubber at 20°C

and 40°C whereas the PD numbers of silicone rubber-based nanocomposite (1 wt%) were greater than neat silicone rubber at 40°C and 60°C. We attribute the reason for the increase in PD magnitudes and PD numbers to agglomeration of the nanofiller in the silicone rubber matrix. The tactoids represent the weak points that could enhance PD repetition inside

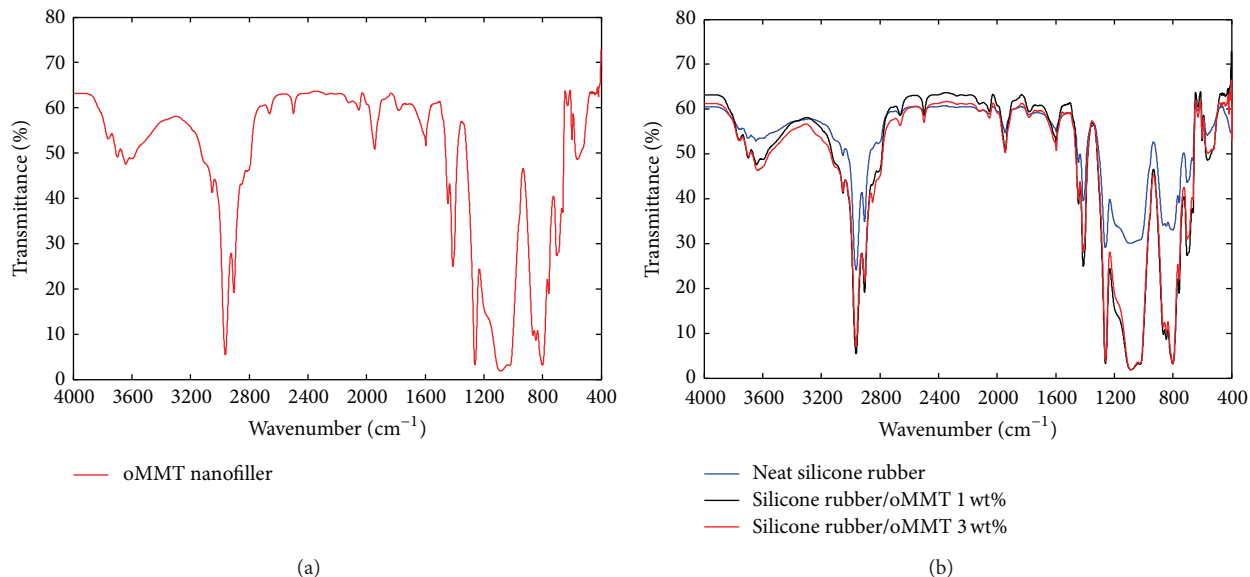


FIGURE 6: FTIR spectra. (a) oMMT nanofiller is denoted by the red line. (b) Neat silicone rubber is denoted by the blue line, silicone rubber-based nanocomposite (1 wt%) is denoted by the black line, and silicone rubber-based nanocomposite (3 wt%) is denoted by the red line.

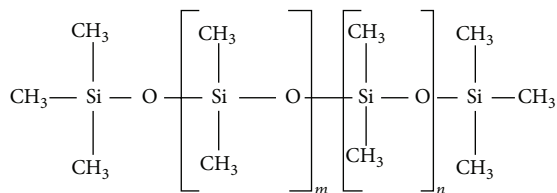


FIGURE 7: Chemical structure of polydimethylsiloxane of silicone rubber [26].

the polymer. This is depicted in Figure 1(a), which shows agglomeration of filler particles sizes greater than 100 nm occurring inside the silicone rubber-based nanocomposite sample with 1 wt% oMMT nanofiller. However, agglomerated nanoparticles larger than 100 nm are considered to be microparticles. Microparticles have also contributed to the suppression of an electrical tree [43, 44] by acting as a physical barrier to the growth of tree channels, resulting in the tree forming more side branches when it collided with the microparticles.

## 5. Chemical Bonding Study via FTIR

FTIR spectra could be used to show the nature of bonding or chemical changes of neat silicone rubber and silicone rubber-based nanocomposite structures. FTIR spectra of oMMT filler and silicone rubber-based nanocomposites (1 wt% and 3 wt%) are depicted in Figure 6. The chemical structure (ring molecule) of silicone rubber is depicted in Figure 7 [26].

Silicone rubber consists of organic methyl groups (CH<sub>3</sub>) and a silicone-oxygen backbone. The methyl groups are responsible for water repellence, surface hardness, and non-combustibility, whereas the vinyl groups (CH=CH<sub>2</sub>) help

TABLE 2: Neat silicone rubber IR band characteristics (polydimethylsiloxane) [48].

Wavenumber (cm <sup>-1</sup> )	Bond
3700–3200	OH
2960–2762	CH in CH <sub>3</sub>
1640	OH in H <sub>2</sub> O
1440–1410	CH
1270–1255	Si–CH <sub>3</sub>
1200–1000	Si–O–Si
870–850	Si(CH <sub>3</sub> ) <sub>3</sub>
840–790	Si(CH <sub>3</sub> ) <sub>2</sub>
700	Si(CH <sub>3</sub> )

to strengthen the rigidity of the molecular structure by creating easier cross-linkage of the molecules [45, 46]. The silicone rubber was vulcanized to give the required solid shape. Vulcanization and cross-linking are terms that refer to the formation of chemical bonds between polymeric chains attained under high pressure and high temperature [26]. The increase in the number of hydrocarbon vinyl groups (–CH<sub>2</sub>) is associated with the increase in the number of cross-links as this group is part of the silicone cross-link domain [47, 48]. Moreover, the presence of cross-links reduces the swelling (bending) capacity and inhibits the transfer of polymer chains into solution [49]. Possible bonds in the neat silicone rubber (polydimethylsiloxane, PDMS) are presented in Table 2.

Based on the FTIR spectra of the oMMT nanofiller in Figure 6(a), peaks occur at 3631 cm<sup>-1</sup>, 3427 cm<sup>-1</sup>, 3246 cm<sup>-1</sup>, 2920 cm<sup>-1</sup>, and 2850 cm<sup>-1</sup>. The peak at 3631 cm<sup>-1</sup> corresponds to broadening of the stretching vibration of hydroxyl groups (–OH), whereas the peaks at 3427 cm<sup>-1</sup> and 3246 cm<sup>-1</sup> indicate the stretching vibration of the amine

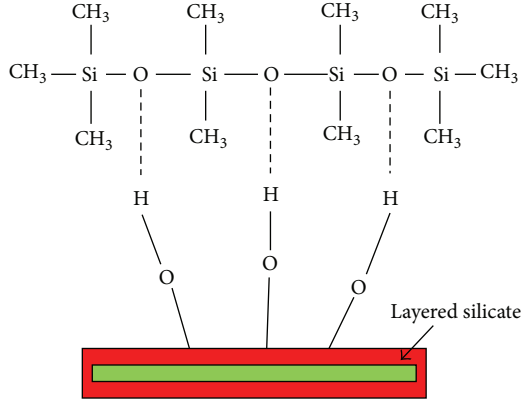


FIGURE 8: Possible interface model between nanoparticle and silicone rubber segments.

group (N-H) due to modification with octadecylamine. The peaks at  $2920\text{ cm}^{-1}$  and  $2850\text{ cm}^{-1}$  correspond to  $-\text{CH}$  stretching vibrations of the methyl group ( $-\text{CH}_3$ ). The presence of the hydroxyl ( $-\text{OH}$ ) group is likely to have originated from the  $-\text{OH}$  bond existing inside the oMMT nanofiller molecule and bonded to the nanoparticle/silicate layers surfaces by hydrogen bonding.

Likewise, the addition of oMMT nanofillers in the silicone rubber matrices increased the  $-\text{OH}$  functional groups results in the spectra band between  $3650\text{ cm}^{-1}$  and  $3500\text{ cm}^{-1}$ , which indicates the free  $-\text{OH}$  stretching vibration in Figure 6(b). By adding 1 wt% and 3 wt% oMMT nanofiller, the  $-\text{OH}$  bands broadened significantly due to the abundance of  $-\text{OH}$  groups. The hydroxyl groups on the surface of the nanoparticles led to the formation of hydrogen bonds between the hydroxyl groups ( $-\text{OH}$ ) and the oxygen in the siloxane, which is the backbone of silicone rubber (PDMS) matrix.

This interpretation agrees with the studies done by Fragiadakis and Pissis [50] and Ramirez et al. [51] that dealt with the hydrogen bonding between silica/PDMS filler/polymer and the separation studies done by Singha and Thomas [52] and Nelson et al. [53] that explained the influence of the hydrogen bond due to the presence of the hydroxyl functional groups at the surfaces of untreated ZnO and  $\text{TiO}_2$  added to epoxy resin. These hydrogen bonds form the strong bond and tightly bounded layers at the interfaces between the nanoparticle and the silicone rubber matrix, as depicted in Figure 8.

In addition, the thermal stability of silicone rubber nanocomposites has also improved due to the ability to resist dehydration at high temperature by the presence of a high number of hydroxyl ( $-\text{OH}$ ) groups at the nanoparticle surfaces. Dehydration may result in weaker filler-polymer matrix interfaces. The presence of a high number of hydroxyl groups helps in hydration and removes the heat to lower the temperature at the interface, improving the insulation properties [51, 54].

The broad peak that appears at  $\sim 1000\text{--}1200\text{ cm}^{-1}$  corresponds to  $\text{Si-O-Si}$  stretching, which may be due to

an increase in the oxidative cross-linking reaction resulting from oxidation of the hydrocarbon groups on the polymer main chain. This reaction would lead to cross-linking and increase the network chain concentration, leading to a brittle (hard) surface layer [55, 56]. In addition, the FTIR shows an increase in the number of hydrocarbon methyl ( $\text{CH}_3$ ) groups with increasing filler concentration. The bands at  $2975\text{--}2875\text{ cm}^{-1}$  correspond to the stretching vibration of the hydrocarbon methyl group. The transmittance amplitude also increased with the increase in filler content, which shows an increase in the alkyl groups. Therefore, the increase in filler concentration contributes to the increase in cross-link numbers of silicone rubber.

Sylgard 184 silicone rubber has a thermal stability between  $-45^\circ\text{C}$  and  $200^\circ\text{C}$  [57]. This excellent thermal stability is attributable to the high dissociation energy of the siloxane bond,  $\text{Si-O-Si}$ , which is highly stable at a value of  $445\text{ kJ/mol}$  [58]. However, the influence of temperature on the number of cross-links could be elucidated by referring to the following formula [35]:

$$E_m = \frac{3\chi RT}{M_{av}}, \quad (1)$$

where  $E_m$  is the elastic modulus,  $\chi$  is the density of silicone rubber,  $R$  is the gas constant,  $T$  is temperature, and  $M_{av}$  is the average molecular weight per vulcanization point in silicone rubber. The elastic modulus  $E$  increases with the decrease in average molecular weight  $M_{av}$ . The decrease in  $M_{av}$  results in an increase in the vulcanization point in silicone rubber. Thus, the increase in temperature  $T$  increases the elastic modulus  $E_m$  and thereby increases the vulcanization point density. The higher the elastic modulus, the stronger the forces that are required for material deformation. Therefore, the electrical tree becomes more difficult to propagate due to the increase in the elastic modulus as a function of temperature. The increase in  $E_m$  increased the number of molecular bonds due to the increase in vulcanization points or number of cross-links that are required to be broken down to form more coalesced cavities for electrical tree initiation and propagation.

As a result, the resistance of the electrical tree and PD caused by increasing vulcanization or cross-link numbers is due to the influence of temperature. The existence of the hydrogen bond between the nanoparticle surfaces and silicone rubber matrices has led to the existence of better adhesion at the filler/polymer interface, which requires higher dissociation energy to break the bonding for polymer decomposition. However, in the case of silicone rubber-based nanocomposites (1 wt% and 3 wt%), the difference in PD and electrical tree resistivity is due to a decrease in interfiller distance, which implies a better shielding effect of the nanoparticles by leaving very narrow regions of the material (silicone rubber) exposed to the discharges. The nanoparticles may form a physical barrier against the discharges and lead to the enormous increase in the discharge resistance performance. With an increase in temperature, the best PD and electrical tree resistance/inhibition performance was exhibited by the silicone rubber-based nanocomposite

(3 wt%) taking into account all inhibition factors as discussed earlier.

## 6. Conclusions

The effect of temperature on electrical tree growth and corresponding PD activity were investigated in silicone rubber with different levels of oMMT nanofiller content. The presence of nanofiller reduced the temperature dependence of the electrical properties of the silicone rubber matrix such that the phase distribution of PD activities became insensitive to changes in temperature. The introduction of 3 wt% oMMT nanofiller inhibited electrical tree initiation over the temperature range with a 4-hour interval for each experiment. Under high temperature, the vulcanization effect played a role in introducing more cross-linking in the silicone rubber chains. Therefore, under a high temperature up to 60°C, electrical treeing took more time to propagate at room-temperature vulcanized silicone rubber. The presence of a hydroxyl group at the surface of nanoparticles led to the formation of hydrogen bonds between the hydroxyl and the oxygen from the siloxane backbone of the silicone rubber matrix. The hydrogen bond helped in strengthening the interaction between the nanoparticles and the polymer matrix thus increased the physical bonding. This enhanced bonding increased the insulation properties, thereby resisting PD and electrical tree degradation. As a result, this study suggests that oMMT nanoclay as a nanofiller could be employed in insulating materials to improve their degradation due to internal discharges.

## Conflict of Interests

The authors declare no conflict of interests.

## Acknowledgments

The authors wish to thank Universiti Teknologi Malaysia and Ministry of Education for financial support through research Grants Vot nos. 01K07, 4F599, 4F398, and 06H77. Last but not least, special thanks are due to Professor Dr. John Fothergill from City University, UK, Dr. Steve Dodd, and Dr. Nikola Chalashkanov from University of Leicester, UK, for their kind contributions and help during the study.

## References

- [1] S. S. Bamji, "Electroluminescence—a technique to detect the initiation of degradation in polymeric insulation," *IEEE Electrical Insulation Magazine*, vol. 15, no. 3, pp. 6–18, 1999.
- [2] R. Sarathi and P. G. Raju, "Study of electrical treeing phenomena in XLPE cable samples using acoustic techniques," *Electric Power Systems Research*, vol. 73, no. 2, pp. 159–168, 2005.
- [3] M. Bao, X. Yin, and J. He, "Analysis of electrical tree propagation in XLPE power cable insulation," *Physica B: Condensed Matter*, vol. 406, no. 8, pp. 1556–1560, 2011.
- [4] X. Zheng and G. Chen, "Propagation mechanism of electrical tree in XLPE cable insulation by investigating a double electrical tree structure," *IEEE Transactions on Dielectrics and Electrical Insulation*, vol. 15, no. 3, pp. 800–807, 2008.
- [5] L. Ying and C. Xiaolong, "A novel method for the insulation thickness design of HV XLPE cable based on electrical treeing tests," *IEEE Transactions on Dielectrics and Electrical Insulation*, vol. 21, no. 4, pp. 1540–1546, 2014.
- [6] L. Ying and C. Xiaolong, "Electrical tree initiation in XLPE cable insulation by application of DC and impulse voltage," *IEEE Transactions on Dielectrics and Electrical Insulation*, vol. 20, no. 5, pp. 1691–1698, 2013.
- [7] E. M. Jarvid, A. B. Johansson, J. H. M. Blennow, M. R. Andersson, and S. M. Gubanski, "Evaluation of the performance of several object types for electrical treeing experiments," *IEEE Transactions on Dielectrics and Electrical Insulation*, vol. 20, no. 5, pp. 1712–1719, 2013.
- [8] J. K. Nelson, *Dielectric Polymer Nanocomposites*, Springer, Boston, Mass, USA, 2010.
- [9] X. Huang, F. Liu, P. Jiang, and T. Tanaka, "Is graphene oxide an insulating material?" in *Proceedings of the IEEE International Conference on Solid Dielectrics (ICSD '13)*, pp. 904–907, July 2013.
- [10] W. A. Izzati, Y. Z. Arief, Z. Adzis, and M. Shafanizam, "Partial discharge characteristics of polymer nanocomposite materials in electrical insulation: A review of sample preparation techniques, analysis methods, potential applications, and future trends," *The Scientific World Journal*, vol. 2014, Article ID 735070, 14 pages, 2014.
- [11] F. Guastavino, A. Dardano, S. Squarcia et al., "Electrical treeing in LDPE nanocomposite materials," in *Proceedings of the 2009 IEEE Conference on Electrical Insulation and Dielectric Phenomena*, pp. 697–700, June 2009.
- [12] F. Guastavino, A. Dardano, G. C. Montanari, L. Testa, and F. Bellucci, "Electrical treeing in EVA-boehmite and EVA-montmorillonite nanocomposites," in *Proceedings of the IEEE Electrical Insulation Conference (EIC '09)*, pp. 382–386, IEEE, Montreal, Canada, June 2009.
- [13] Z. Jinmei, G. Junguo, J. Quanquan, Z. Mingyan, and Z. Xiaohong, "Studies on electrical tree and partial discharge properties of PE/MMT nanocomposites," in *Proceedings of the International Symposium on Electrical Insulating Materials (ISEIM '08)*, pp. 311–314, September 2008.
- [14] S. Raetzke, Y. Ohki, T. Imai, T. Tanaka, and J. Kindersberger, "Tree initiation characteristics of epoxy resin and epoxy/clay nanocomposite," *IEEE Transactions on Dielectrics and Electrical Insulation*, vol. 16, no. 5, pp. 1473–1480, 2009.
- [15] B. X. Du, Z. L. M. Gao, and T. Han, "Effect of temperature on electrical tree in silicone rubber," in *Proceedings of the 10th IEEE International Conference on Solid Dielectrics*, pp. 1–4, 2010.
- [16] H. G. Yaworski, G. Craig, and D. Roberts, "The use of silicon gels for jointing power cables," in *Proceedings of the 14th IEEE Transmission and Distribution Conference*, pp. 396–401, September 1996.
- [17] R. R. Bukovnik and P. R. Carey, "Advances in silicone gel technology for cable accessories," in *Proceedings of the IEEE Power Engineering Society Transmission and Distribution Conference*, pp. 634–637, Dallas, Tex, USA, May 2006.
- [18] H. G. Yaworski and R. R. Bukovnik, "Silicone gel technology for power cable accessories," in *Proceedings of the IEEE/PES Transmission and Distribution Conference and Exposition*, vol. 2, pp. 837–842, November 2001.
- [19] A. A. A. Jamil, M. Kamarol, M. Mariatti et al., "Organomontmorillonite as an electrical treeing retardant for polymeric

- insulating materials,” in *Proceedings of the IEEE International Conference on Condition Monitoring and Diagnosis (CMD '12)*, pp. 237–240, September 2012.
- [20] B. X. Du, Z. L. Ma, Y. Gao, T. Han, and Y. S. Xia, “Effects of nano filler on treeing phenomena of silicone rubber nanocomposites,” in *Proceedings of the Annual Report Conference on Electrical Insulation and Dielectric Phenomena (CEIDP '11)*, pp. 788–791, October 2011.
- [21] M. Arroyo, M. A. López-Manchado, and B. Herrero, “Organomontmorillonite as substitute of carbon black in natural rubber compounds,” *Polymer*, vol. 44, no. 8, pp. 2447–2453, 2003.
- [22] A. A. A. Jamil, N. Bashir, M. H. Ahmad, Y. Z. Arief, M. Kamarol, and M. Mariatti, “Electrical treeing initiation and propagation in silicone rubber nanocomposites,” in *Proceedings of the IEEE Conference on Electrical Insulation and Dielectric Phenomena (CEIDP '13)*, pp. 502–505, IEEE, Shenzhen, China, October 2013.
- [23] R. Liao, G. Bai, L. Yang, H. Cheng, Y. Yuan, and J. Guan, “Improved electric strength and space charge characterization in LDPE composites with montmorillonite fillers,” *Journal of Nanomaterials*, vol. 2013, Article ID 712543, 7 pages, 2013.
- [24] R. Jongen, E. Gulski, and J. Smit, “Failures of medium voltage cable joints in relation to the ambient temperature,” in *Proceedings of the 20th International Conference and Exhibition on Electricity Distribution (CIRED '09)*, 11, p. 8, June 2009.
- [25] N. Shimizu, Y. Shibata, K. Ito, K. Imai, and M. Nawata, “Electrical tree at high temperature in XLPE and effect of oxygen,” in *Proceedings of the IEEE Conference on Electrical Insulation and Dielectric Phenomena*, vol. 1, pp. 329–332, October 2000.
- [26] J. Kindersberg, A. Scutz, H. Karner, and R. Huir, “Service performance, material design and applications of composite insulators with silicone rubber housings,” *CIGRE* 33–303, 1996.
- [27] F. Bellucci, D. Fabiani, G. C. Montanari, and L. Testa, “The processing of nanocomposites,” in *Dielectric Polymer Nanocomposites*, J. K. Nelson, Ed., pp. 31–64, Springer, Boston, Mass, USA, 2010.
- [28] Y. Kojima, A. Usuki, M. Kawasumi, A. Okada, T. Kurauchi, and O. Kamigaito, “One-pot synthesis of nylon 6-clay hybrid,” *Journal of Polymer Science Part A: Polymer Chemistry*, vol. 31, no. 7, pp. 1755–1758, 1993.
- [29] M. Alexandre and P. Dubois, “Polymer-layered silicate nanocomposites: preparation, properties and uses of a new class of materials,” *Materials Science and Engineering R: Reports*, vol. 28, no. 1, pp. 1–63, 2000.
- [30] S. Sinha Ray, K. Okamoto, and M. Okamoto, “Structure—property relationship in biodegradable poly(butylene succinate)/layered silicate nanocomposites,” *Macromolecules*, vol. 36, no. 7, pp. 2355–2367, 2003.
- [31] A. A. A. Jamil, M. H. B. Ahmad, M. Kamarol, M. Mariatti, and M. A. M. Piah, “Short-term breakdown in silicone rubber based nanocomposites caused by electrical treeing,” *Advanced Materials Research*, vol. 845, pp. 482–486, 2013.
- [32] I. A. Tsekmes, *Electrical characterization of polymeric DC mini-cables by means of space charge & conduction current measurements [BEng thesis]*, Delft University of Technology, 2012.
- [33] K. Ishimoto, E. Kanegae, Y. Ohki et al., “Superiority of dielectric properties of LDPE/MgO nanocomposites over microcomposites,” *IEEE Transactions on Dielectrics and Electrical Insulation*, vol. 16, no. 6, pp. 1735–1742, 2009.
- [34] N. M. Chalashkanov, S. J. Dodd, L. A. Dissado, and J. C. Fothergill, “Pulse sequence analysis on PD data from electrical trees in flexible epoxy resins,” in *Proceedings of the Annual Report Conference on Electrical Insulation and Dielectric Phenomena (CEIDP '11)*, pp. 776–779, October 2011.
- [35] B. X. Du, Z. L. Ma, Y. Gao, and T. Han, “Effect of ambient temperature on electrical treeing characteristics in silicone rubber,” *IEEE Transactions on Dielectrics and Electrical Insulation*, vol. 18, no. 2, pp. 401–407, 2011.
- [36] M. G. Danikas and T. Tanaka, “Nanocomposites—a review of electrical treeing and breakdown,” *IEEE Electrical Insulation Magazine*, vol. 25, no. 4, pp. 19–25, 2009.
- [37] T. Tanaka, “Internal partial discharge and material degradation,” *IEEE Transactions on Electrical Insulation*, vol. 21, no. 6, pp. 899–905, 1986.
- [38] M. G. Danikas, “Small partial discharges and their role in insulation deterioration,” *IEEE Transactions on Dielectrics and Electrical Insulation*, vol. 4, no. 6, pp. 863–867, 1997.
- [39] M. G. Danikas, “The definitions used for partial discharge phenomena,” *IEEE Transactions on Electrical Insulation*, vol. 28, no. 6, pp. 1075–1081, 1993.
- [40] T. Tanaka, “Partial discharge pulse distribution pattern analysis,” *IEE Proceedings: Science, Measurement and Technology*, vol. 142, no. 1, pp. 46–50, 1995.
- [41] T. Takahashi, J. Suzuki, H. Miyata et al., “Relation between electroluminescence and degradation in XLPE,” *IEEE Transactions on Dielectrics and Electrical Insulation*, vol. 8, no. 1, pp. 91–96, 2001.
- [42] S. Alapati and M. J. Thomas, “Electrical treeing and the associated PD characteristics in LDPE nanocomposites,” *IEEE Transactions on Dielectrics and Electrical Insulation*, vol. 19, no. 2, pp. 697–704, 2012.
- [43] R. Kurnianto, Y. Murakami, N. Hozumi, and M. Nagao, “Characterization of tree growth in inorganic-filler/epoxy resin composite material,” in *Proceedings of the 8th International Conference on Properties and Applications of Dielectric Materials (ICPADM '06)*, pp. 123–126, June 2006.
- [44] M. Nagao, K. Oda, K. Nishioka, Y. Muramoto, and N. Hozumi, “Effect of filler on treeing phenomenon in epoxy resin under AC voltage,” in *Proceedings of the International Symposium on Electrical Insulating Materials (ISEIM '01)*, pp. 611–614, IEEE, Himeji, Japan, 2001.
- [45] J. P. Reynders, I. R. Jandrell, and S. M. Reynders, “Review of aging and recovery of silicone rubber insulation for outdoor use,” *IEEE Transactions on Dielectrics and Electrical Insulation*, vol. 6, no. 5, pp. 620–631, 1999.
- [46] G. W. Gokel, *Dean's Handbook of Organic Chemistry*, McGraw-Hill, 2nd edition, 2004.
- [47] S. Ganga, G. R. Viswanath, and R. S. S. Aradhya, “Improved performance of silicone rubber insulation with nano fillers,” in *Proceedings of the IEEE 10th International Conference on the Properties and Applications of Dielectric Materials (ICPADM '12)*, pp. 1–4, IEEE, Bangalore, India, July 2012.
- [48] S.-H. Kim, E. A. Cherney, R. Hackam, and K. G. Rutherford, “Chemical changes at the surface of RTV silicone rubber coatings on insulators during dry-band arcing,” *IEEE Transactions on Dielectrics and Electrical Insulation*, vol. 1, no. 1, pp. 106–123, 1994.
- [49] C. Lee, K. J. K. Lim, Y. G. Y. Park, B. H. Ryu, and K. Y. Kim, “Radiation effects on electrical treeing resistance and mechanical characteristics of low density polyethylene containing barbituric acid derivatives,” in *Proceedings of the 6th International Conference on Properties and Applications of*

- Dielectric Materials*, vol. 1 of (Cat. No. 00CH36347), pp. 501–504, 2000.
- [50] D. Fragiadakis and P. Pissis, “Glass transition and segmental dynamics in poly(dimethylsiloxane)/silica nanocomposites studied by various techniques,” *Journal of Non-Crystalline Solids*, vol. 353, no. 47–51, pp. 4344–4352, 2007.
- [51] I. Ramirez, S. Jayaram, E. A. Cherney, M. Gauthier, and L. Simon, “Erosion resistance and mechanical properties of silicone nanocomposite insulation,” *IEEE Transactions on Dielectrics and Electrical Insulation*, vol. 16, no. 1, pp. 52–59, 2009.
- [52] S. Singha and M. J. Thomas, “Influence of filler loading on dielectric properties of epoxy-ZnO nanocomposites,” *IEEE Transactions on Dielectrics and Electrical Insulation*, vol. 16, no. 2, pp. 531–542, 2009.
- [53] J. K. Nelson, L. A. Utracki, R. K. MacCrone, and C. W. Reed, “Role of the Interface in determining the dielectric properties of nanocomposites,” in *Proceedings of the 17th Annual Meeting of the IEEE Lasers and Electro-Optics Society (LEOS '04)*, pp. 314–317, October 2004.
- [54] B. Venkatesulu and M. J. Thomas, “Erosion resistance of alumina-filled silicone rubber nanocomposites,” *IEEE Transactions on Dielectrics and Electrical Insulation*, vol. 17, no. 2, pp. 615–624, 2010.
- [55] B. Ma, J. Andersson, and S. M. Gubanski, “Evaluating resistance of polymeric materials for outdoor applications to corona and ozone,” *IEEE Transactions on Dielectrics and Electrical Insulation*, vol. 17, no. 2, pp. 555–565, 2010.
- [56] D. K. Thomas, “Network scission processes in peroxide cured methylvinyl silicone rubber,” *Polymer*, vol. 7, no. 2, pp. 99–105, 1966.
- [57] Dow Corning, Solar Sylgard 184 Silicone Elastomer Data Sheet.
- [58] A. E. Beezer and C. T. Mortimer, “Heats of formation and bond energies. Part XV. Chlorotrimethylsilane and hexamethyldisilazane,” *Journal of the Chemical Society A: Inorganic, Physical, Theoretical*, pp. 514–516, 1966.

## Research Article

# Space Charge Property of Polyethylene/Silica Nanocomposites at Different Elongations

Can Wang, Youyuan Wang, Peng Fan, and Ruijin Liao

State Key Laboratory of Power Transmission Equipment & System Security and New Technology, Chongqing University, Chongqing 400030, China

Correspondence should be addressed to Can Wang; 20094589@cqu.edu.cn

Received 22 December 2014; Revised 14 February 2015; Accepted 12 March 2015

Academic Editor: Mircea Chipara

Copyright © 2015 Can Wang et al. This is an open access article distributed under the Creative Commons Attribution License, which permits unrestricted use, distribution, and reproduction in any medium, provided the original work is properly cited.

This paper prepares polyethylene/silica nanocomposites with concentrations of 3 wt% and 5 wt% by using silicon dioxide (SiO<sub>2</sub>) nanopowder (nanosilica) with particle sizes of 15 and 50 nm. Samples whose elongations are 3%, 6%, and 10% are prepared. Pulsed electroacoustic technique is applied to evaluate the space charge distribution in samples. Test results show that homocharge near electrodes is generated in the polyethylene/silica nanocomposites. Nanocomposites with a nanoparticle concentration of 3 wt% and particle size of 15 nm suppress the accumulation of space charge effectively. The amount of space charge in the samples increases with the increase in elongation. At an elongation of 10%, packet-like space charge is generated in polyethylene/silica nanocomposites with the concentration of 5 wt% and particle sizes of 15 and 50 nm. The packet-like space charge in nanocomposites whose particle size is 50 nm is more obvious than that in nanocomposites whose particle size is 15 nm. The experiment results are explained by applying interface characteristics, dipole model, and induced dipole model.

## 1. Introduction

The accumulation of space charge in polymer insulation makes a change of electric field. The electric field near the inner and outer semiconductive shielding layers becomes seriously distorted when a DC electric field on XLPE cables is applied because of the accumulation of space charge; this condition may cause accelerated aging [1, 2]. Mechanical and electrical properties can be effectively improved through the use of nanomodified materials. The present study shows that the amount of space charge traps and the depths in polymer insulation can be reduced by adding nanoparticles, which may effectively minimize the accumulation of space charge and uniform electric field in polymer insulation [3–6].

Cables are inevitably affected by mechanical stress during manufacturing, transportation, installation, and operation. Such stress may cause the insulation materials of cables having elongation [7, 8]. However, current research does not consider the elongation of insulation materials. Consequently, additional research on the electrical properties of polymer insulation during elongation should be conducted. With regard to insulation materials with an accumulation of space

charge, there will be electrical trees by applying mechanical stress without electrical stress [9]. Research indicates that water tree in polymer insulation becomes serious when the cables' elongation is 6% under dynamic tensile stress at different frequencies [10]. The mechanical stress caused by the electric field is considered the reason for breakdown in polymer insulation [11]. Studies have confirmed that electrical and mechanical properties of polyethylene can be improved effectively by adding nanosilica. Similarly, the conclusion that the electrical properties of insulation may be affected by mechanical stress has been confirmed. However, research on the electrical properties of nanomodified materials during elongation is lacking. As such, more research on this area should be conducted.

In this study, polyethylene/silica nanocomposites with particle sizes of 15 and 50 nm and concentrations of 3 wt% and 5 wt% were prepared. Pulsed electroacoustic (PEA) technique was utilized to determine the characteristics of space charge in samples whose elongation is 3% and 6%. The experiment results were explained by applying interface characteristics, dipole model, and induced dipole model.

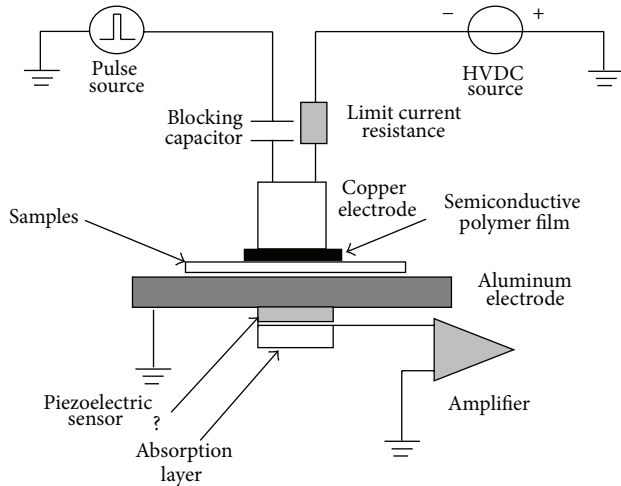


FIGURE 1: Schematic of the PEA device.

## 2. Test Method

**2.1. Test Samples.** Low density polyethylene (LDPE) materials produced by Lanzhou Petrochemical Company were selected and utilized. The model number of LDPE is 2426 H, the density is 0.910–0.925 mg/cm<sup>3</sup>, melt flow index is 2.1–2.2 g/10 min, and the melting point is 112°C. Nanometer material was produced by Shanghai Jingchun Scientific Co., Ltd. Mechanical blending method [12, 13] was applied to prepare the samples. The blending temperature is 120°C, and the blending time is 30 min. The sizes of nanoparticles are 15 and 50 nm, and the concentrations are 3 wt% and 5 wt%. The nanoparticles were dried in a vacuum dry oven for 24 h at 100°C and constant pressure. After blending, the materials were pressed into sheets in a flat vulcanizing machine at a temperature of 120°C, time of 15 min, and pressure of 12 MPa. The films, which were almost 0.19 μm, were cut into a dumbbell by using dumbbell tools and stressed in a tensile machine for 30 min. The samples were degassed in a vacuum dry oven for 24 h at 80°C to eliminate residual stress.

**2.2. PEA Technique.** The space charge characteristics of polyethylene/silica nanocomposites were investigated with PEA technique. The PEA device is shown Figure 1.

In the PEA device, the output of the high-voltage direct current source ranges from 0 to 20 kV. The output of the pulse source ranges from 0 to 0.2 kV, the pulse width is 5 ns, the frequency is 500 Hz, and the thickness of the piezoelectric sensor is 25 μm. The upper electrode is a copper electrode, and the lower electrode is an aluminum one. The PEA device can communicate with computers by using a LeCory7200 digital oscilloscope to collect the measuring signals. The resolution of PEA device is about  $1.2 \times 10^{-3} \text{ C/m}^3$ .

**2.3. Experimental Design.** The samples were stressed by a negative DC voltage for 60 min (electric field of 30 kV/mm). The space charge distribution was recorded at applied voltage times of 1, 10, 20, and 60 min. A short-circuit dissipation test was then applied, and the distribution of space charge at 1, 5, 10, and 20 min was recorded.

## 3. Results

**3.1. Accumulative Characteristics of Space Charge.** The space charge accumulation in an electric field of 30 kV/mm for polyethylene/silica nanocomposites with different elongations is shown in Figure 2.

There are heterocharges near positive and negative electrodes in the LDPE, as shown in Figure 2(a). By adding silica nanoparticles with a particle size of 15 nm and concentration of 3 wt%, the heterocharges near the positive and negative electrodes almost disappeared, shown in Figure 2(e). This result proves that polyethylene/silica nanocomposites can suppress the accumulation of space charge. Obvious homocharge accumulation near positive and negative electrodes was observed in the insulation material when the silica nanoparticles' size was 15 nm and the concentration was 5 wt%, shown in Figure 2(k). This result indicates that the addition of silica nanoparticles resulted in homocharge accumulation near positive and negative polarities. Compared with the polyethylene/silica nanocomposites whose particle size is 50 nm, homocharge accumulation occurred when the concentration was only 3 wt%, shown in Figure 2(i). Homocharge accumulation was more obvious in the polyethylene/silica nanocomposites when the concentration was 5 wt%. We conclude that homocharge accumulation occurs near positive and negative polarities in a DC electric field when silica nanoparticles are added; an increase in particle size enhances this homocharge accumulation. Therefore, appropriate silica nanoparticles whose particle size is not extremely large should be selected in the production of polyethylene/silica nanocomposites.

According to Figure 2, there are more space charges near positive and negative electrodes for the nanocomposites whose elongation is 3% and 6% compared with the nanocomposites without elongation. As shown in Figures 2(b) and 2(c), the homocharge accumulation near positive and negative electrodes is the highest in the LDPE and the larger the elongation is, the more obvious the space charge accumulation is. For the polyethylene/silica nanocomposites whose particle size is 50 nm, a packet-like space charge was observed in the nanocomposites when the elongation is 6%.

To investigate the packet-like space charge in the nanocomposites, we prepared LDPE, polyethylene/silica nanocomposites with a particle size of 15 nm and concentration of 5 wt%, and polyethylene/silica nanocomposites with a particle size of 50 nm and concentration of 5 wt% at an elongation of 10%. The space charge characteristics are shown in Figure 3.

Comparison of the three images in Figure 3 shows that homocharge accumulation is more obvious and more space charges exist in the nanocomposites when the elongation is 10%. However, no packet-like space charge was observed in the LDPE. When the particle size of the silica nanoparticles is 15 nm and the concentration is 5 wt%, a packet-like space charge is created in the polyethylene/silica nanocomposites at an elongation of 10%. For the polyethylene/silica nanocomposites whose particle size is 50 nm and concentration is 5 wt%, a packet-like space charge was also created;

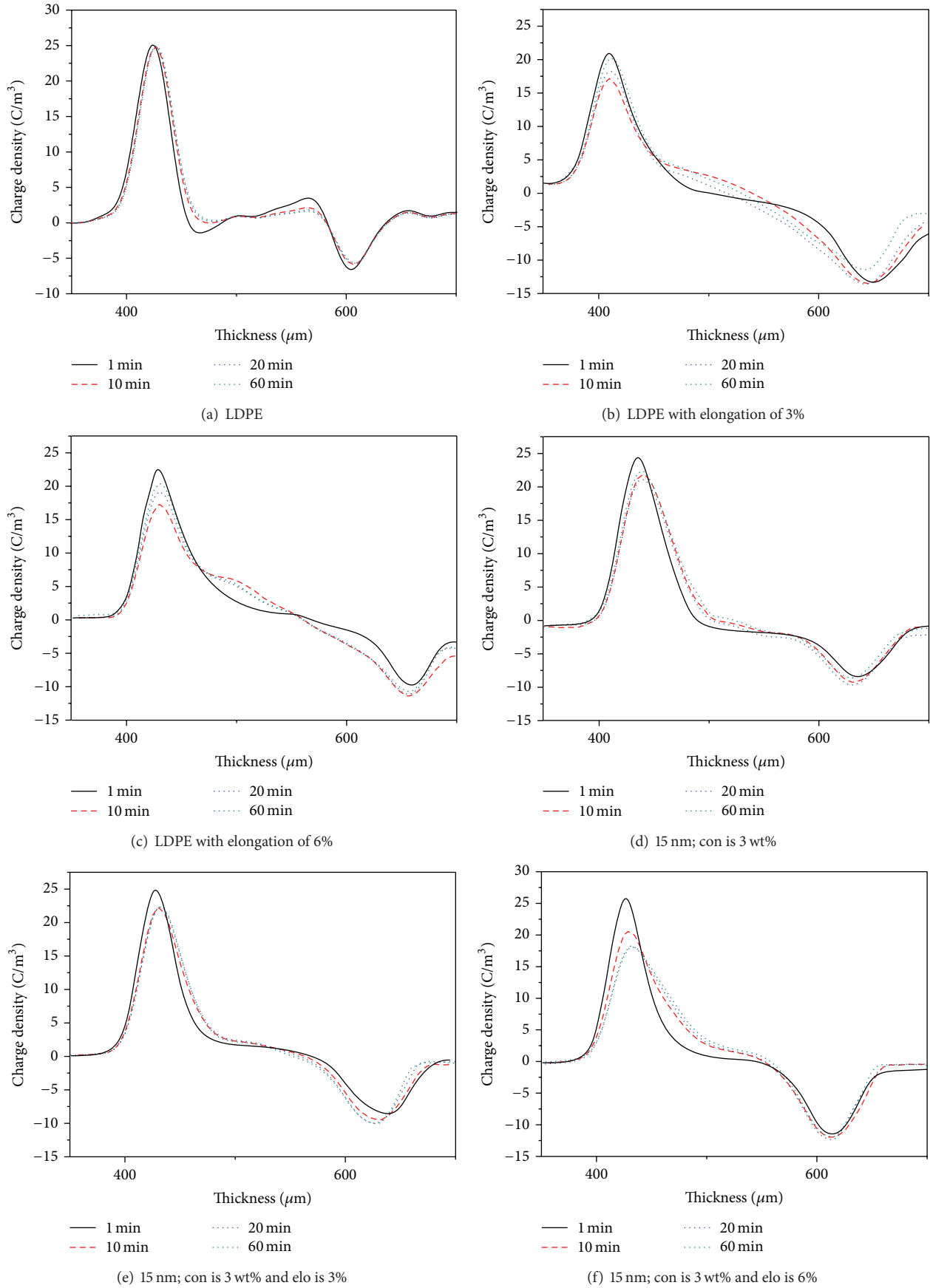


FIGURE 2: Continued.

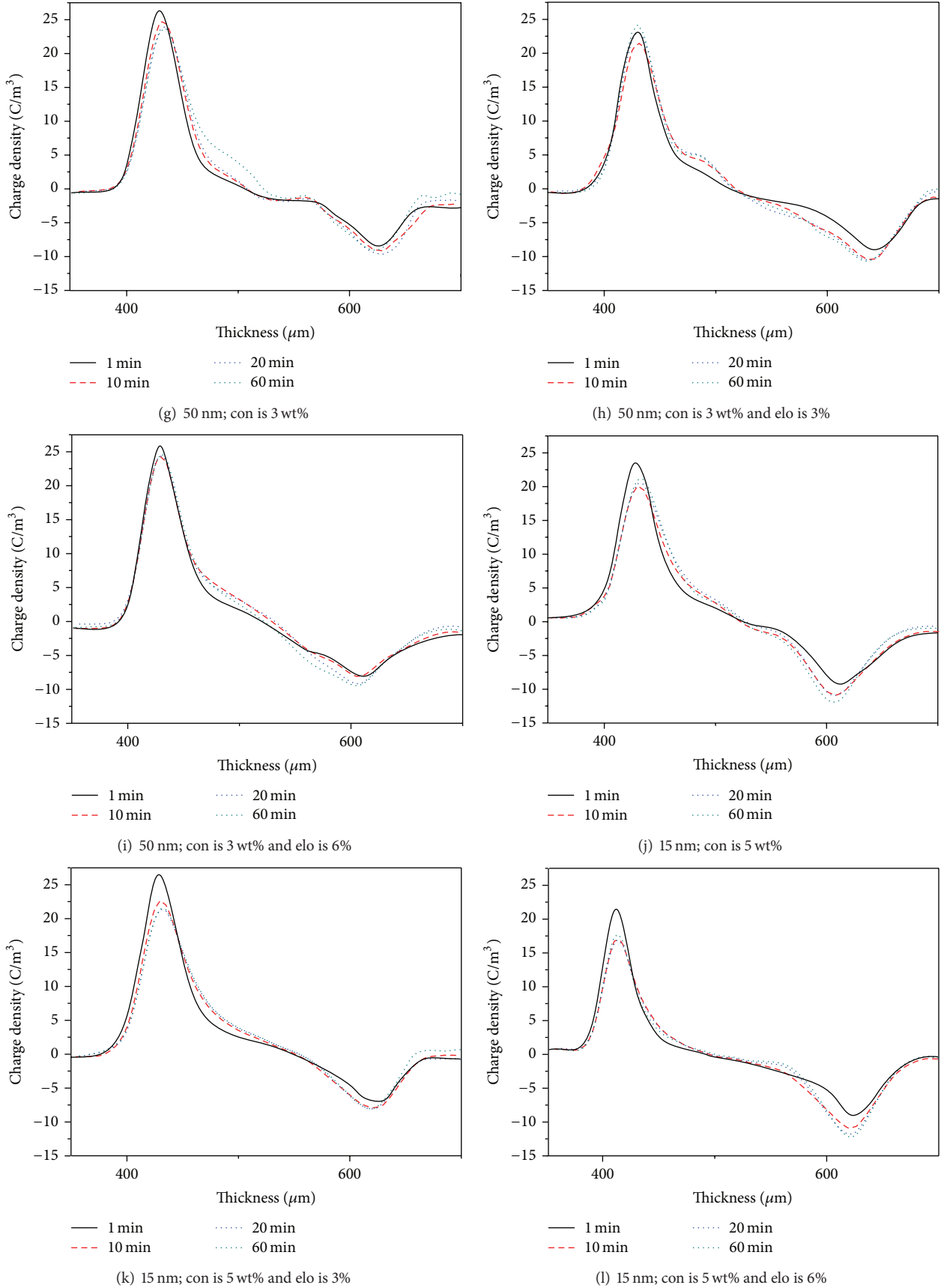


FIGURE 2: Continued.

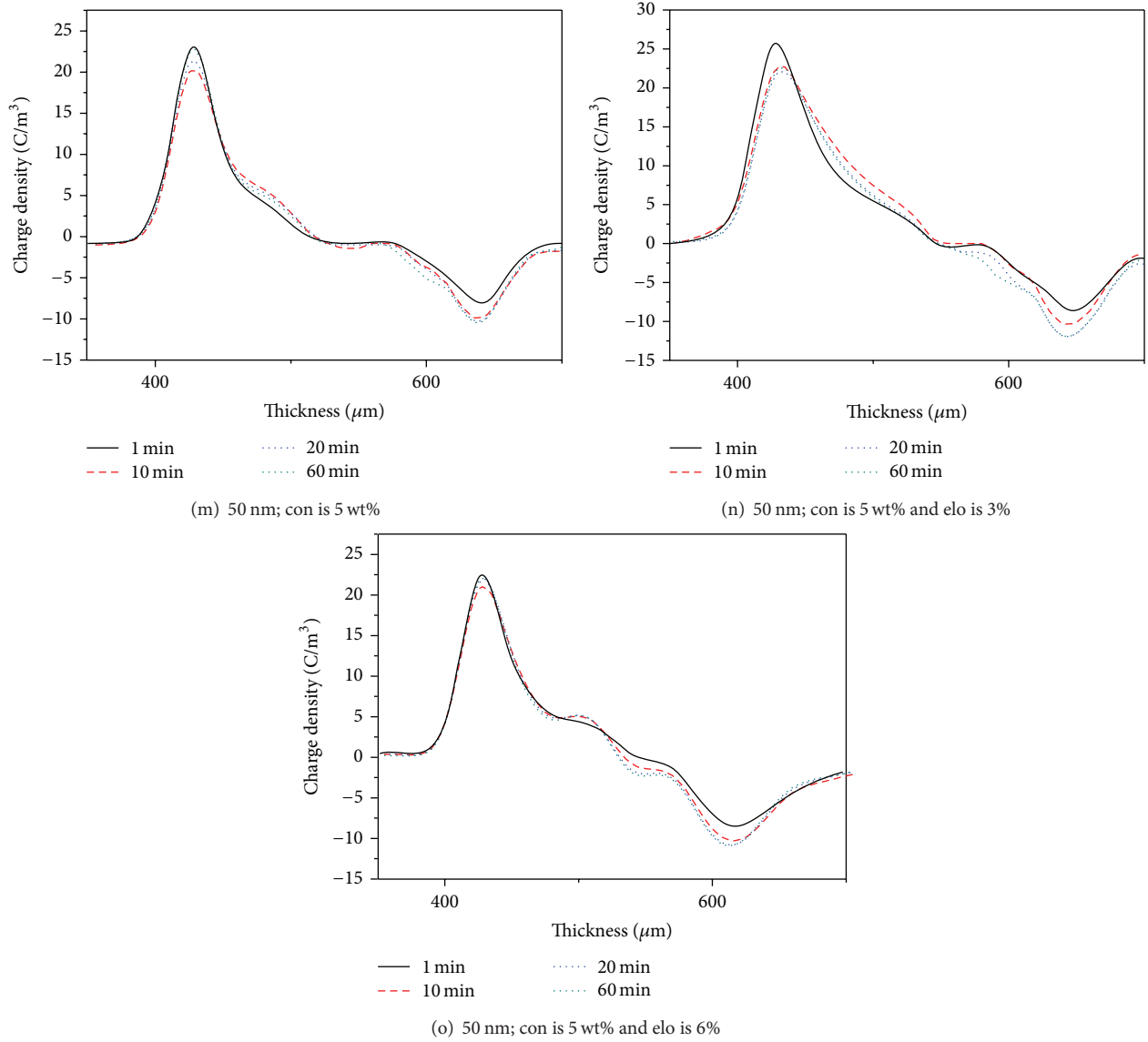


FIGURE 2: Accumulative characteristics of space charge (con represents concentration and elo represents elongation).

the amount of space charge is more than that in the nanocomposites whose particle size is 15 nm. In the nanocomposites with a packet-like space charge, less space charge between the packet-like space charge and electrodes was observed, which may be due to the mutual exclusion of homocharge.

Analyzing Figure 3(c), the packet-like space charges may fit Gaussian distributions. Calculating results shows that the packet-like space charge fits Gaussian distribution well when the time is 60 min, as shown in Figure 4.

The expressions of Figures 4(a) and 4(b) are shown as (1) and (2), respectively:

$$y = 2.77 + \left( \frac{140.06}{22.68 \times \sqrt{\pi/2}} \times e^{-2 \times ((x-514.23)/22.68)^2} \right) \quad (1)$$

$$y = -6.57 + \left( \frac{-78.83}{20.24 \times \sqrt{\pi/2}} \times e^{-2 \times ((x-563.74)/20.24)^2} \right), \quad (2)$$

where  $x$  is position of space charge and  $y$  is charge density.

According to the expressions, the widths of Gaussian distributions are almost equal, which represent the widths of packet-like space charge being very similar when time is 60 min.

**3.2. Detrapping Characteristics of Space Charge.** The dissipation characteristics of space charge are shown in Figure 4.

Studies have shown that the addition of silica nanoparticles can effectively suppress the space charge in nanocomposites and change some of the deep traps into shallow traps. Analysis of Figures 5(a), 5(d), and 5(j) shows that less space charge exists in the nanocomposites whose particle size is 15 nm than in the LDPE when the charge detrapping

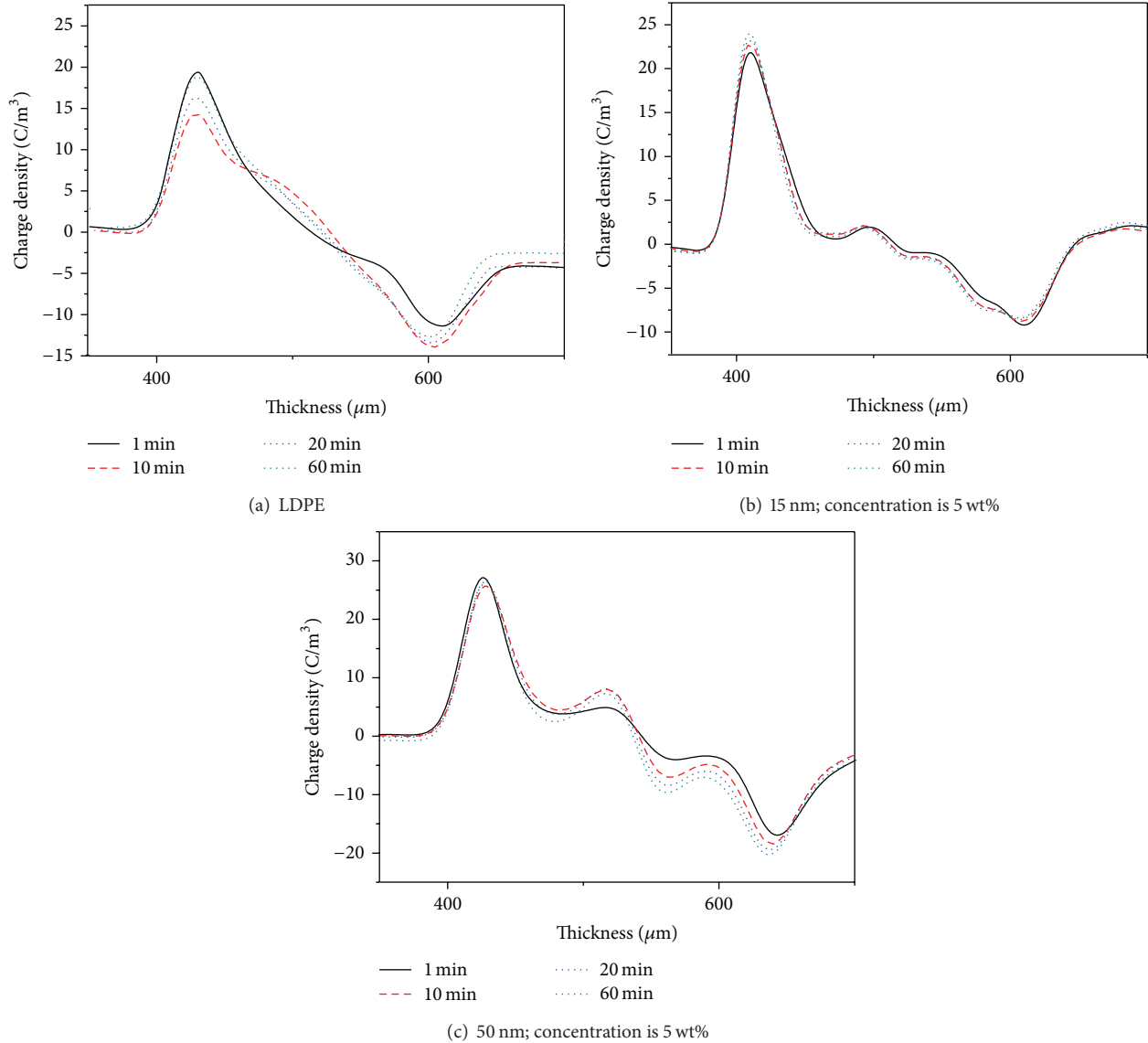


FIGURE 3: Accumulative characteristics of space charge with elongation of 10%.

time is 1 min. Moreover, its charge detrapping rate is higher than LDPE, and the remaining space charge is less. When the charge detrapping time is 1 min, the amount of space charge in the nanocomposites whose particle size is 15 nm is less than the particle size of the silica nanoparticles which is 50 nm, as shown in Figures 5(d), 5(g), 5(j), and 5(m).

Comparison of the three insulation materials with different elongations shows that the charge detrapping rate is higher in the nanocomposites whose particle size is 15 nm than in the LDPE; the detrapping of space charge achieved stability within a short period of time. However, the charge detrapping time is longer in the nanocomposites whose particle size is 15 nm than others; these materials also required more time to reach stability. For the three materials, the amount of space charge is larger in the nanocomposites that are in elongation when the charge detrapping time is 1 min.

With the increase in elongation, more space charges exist in the nanocomposites. Analysis of the curve whose charge detrapping time is 60 min shows that more deep traps are generated with the increase in elongation. Packet-like space charges are created in the polyethylene/silica nanocomposites whose particle size is 50 nm with elongation of 6%. Moreover, packet-like space charges exist in the polyethylene/silica nanocomposites when the charge detrapping time is 60 min. This result means that space charge accumulation is caused by deep traps in this section.

Comparison of the space charge characteristics of the three insulation materials in Figures 6 shows that the amount of space charge and deep traps is larger in the nanocomposites. Packet-like space charges exist in the polyethylene/silica nanocomposites whose particle size is 15 nm as a result of deep traps. Packet-like space charges also exist in the polyethylene/silica nanocomposites whose particle size is

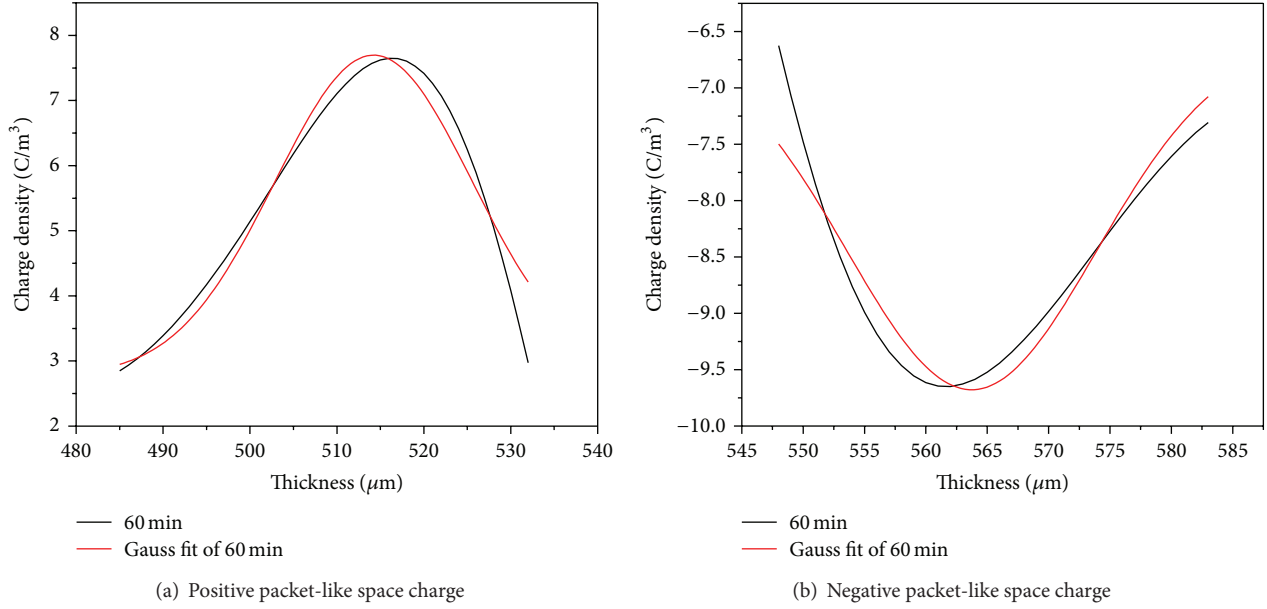


FIGURE 4: Fitting figure.

50 nm, which is more obvious than that in the nanocomposites whose particle size is 15 nm; the dissipation rate is high in the packet-like space charges as a result of deep traps.

## 4. Discussion

**4.1. Effect of Silica Nanoparticles on Space Charge in Polyethylene/Silica Nanocomposites.** Space charge in the nanocomposites is mainly caused by two factors: characteristics of materials and the additives. Given that polymer consists of amorphous and crystalline regions, the interface characteristic between the crystalline and amorphous regions causes a large amount of traps, which may cause the accumulation of electrons and holes. The accumulation of space charge in the LDPE is mainly caused by the crystalline interface and internal defects of materials [14]. As inorganic nanoparticles are added to polymer, nanoparticles occupy the free volume in the material or defect and consequently reduce the amount of free volume and transform the deep traps into shallow traps. The addition of nanoparticles also creates a new interfacial layer between nanoparticles and polymer matrix, which has a significant effect on the electrical properties of nanocomposites. Several researchers believe that the characteristics of this interface can explain the change of properties of materials [15]. Therefore, more research on the interface characteristics of nanocomposites should be conducted.

An assumption is that nanoparticles are spherical and arranged in a simple cubic lattice. Calculation based on weight percent leads to the following expression [16]:

$$D = \left\langle \left\{ \frac{\pi}{6} \left( \frac{\rho_n}{\rho_m} \right) \frac{100}{M} \left[ 1 - \frac{M}{100} \left( 1 - \frac{\rho_n}{\rho_m} \right) \right] \right\}^{1/3} - 1 \right\rangle d, \quad (3)$$

where  $\rho_n$  and  $\rho_m$  are the specific gravity for the nanofiller and polymer matrix, respectively.  $M$  is the weight fraction of nanofiller.  $D$  is interfiller distance and  $d$  is filler diameter.

The calculation expression of the surface area per unit volume is

$$S = \frac{\pi d^2}{(D+d)^3} = \pi \left( \frac{d}{D+d} \right)^2 \frac{1}{D+d}, \quad (4)$$

where  $S$  is total surface area in unit volume.

According to (1) and (2), the distance between two nanoparticles is 158 nm, and the total surface area in unit volume is  $0.872 \text{ km}^2/\text{m}^3$  when the nanoparticles' size is 50 nm and the concentration is 5 wt%. Similarly, the distance between two nanoparticles is 48 nm and total surface area in unit volume is  $2.8 \text{ km}^2/\text{m}^3$  when the particle size is 15 nm and the concentration is 5 wt%. We can see that the total surface area in unit volume is very large for the nanocomposites. The larger the particle size is, the larger the distance between particles is and the larger the total surface area in unit volume is.

Comparison of the space charge characteristics of LDPE and nanocomposites shows that the nanocomposites whose particle size is 15 nm and concentration is 3 wt% exhibit a significant suppression of space charge accumulation in the polyethylene/silica nanocomposites. This finding means the amount of traps caused by interface layer between silica nanoparticles and polymer matrix is smaller than the traps reduced by silica nanoparticles. Homocharge accumulations near positive and negative electrodes were observed in the polyethylene/silica nanocomposites when the sizes of the nanoparticles increase. More homocharges exist in the nanocomposites whose particle size is 50 nm than in the nanocomposites whose particle size is 15 nm. These phenomena can be explained by interface layer characteristics. When

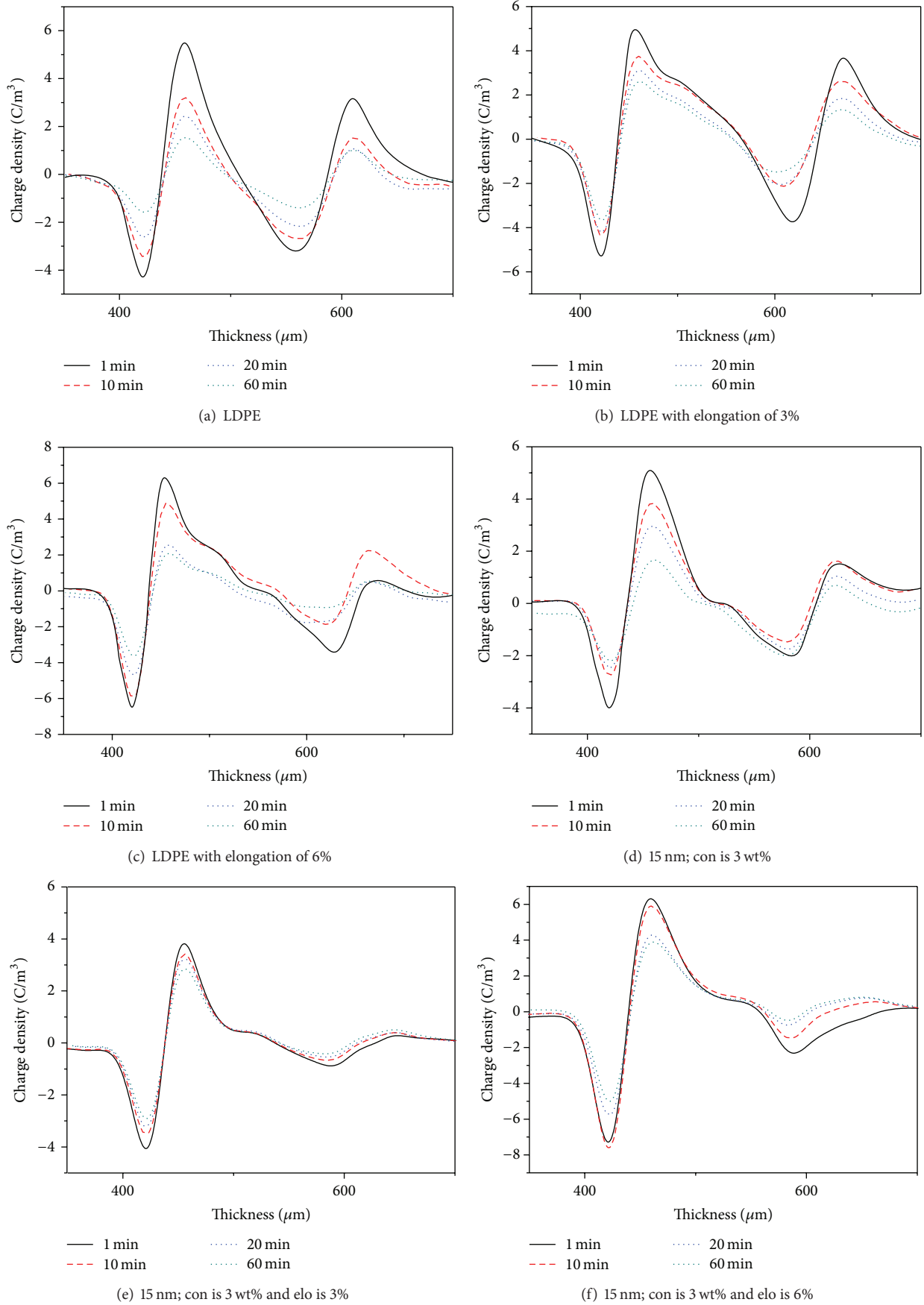


FIGURE 5: Continued.

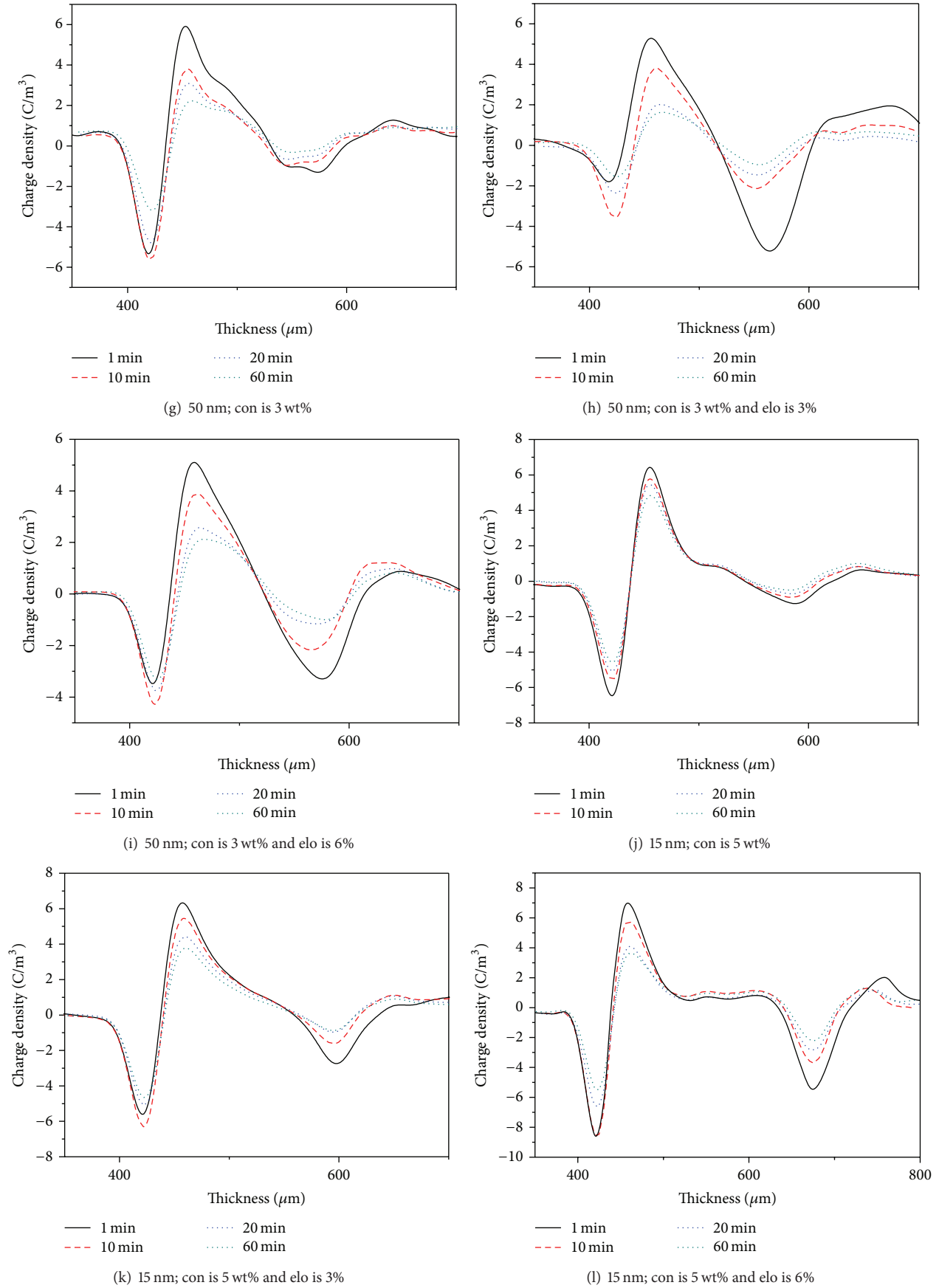


FIGURE 5: Continued.

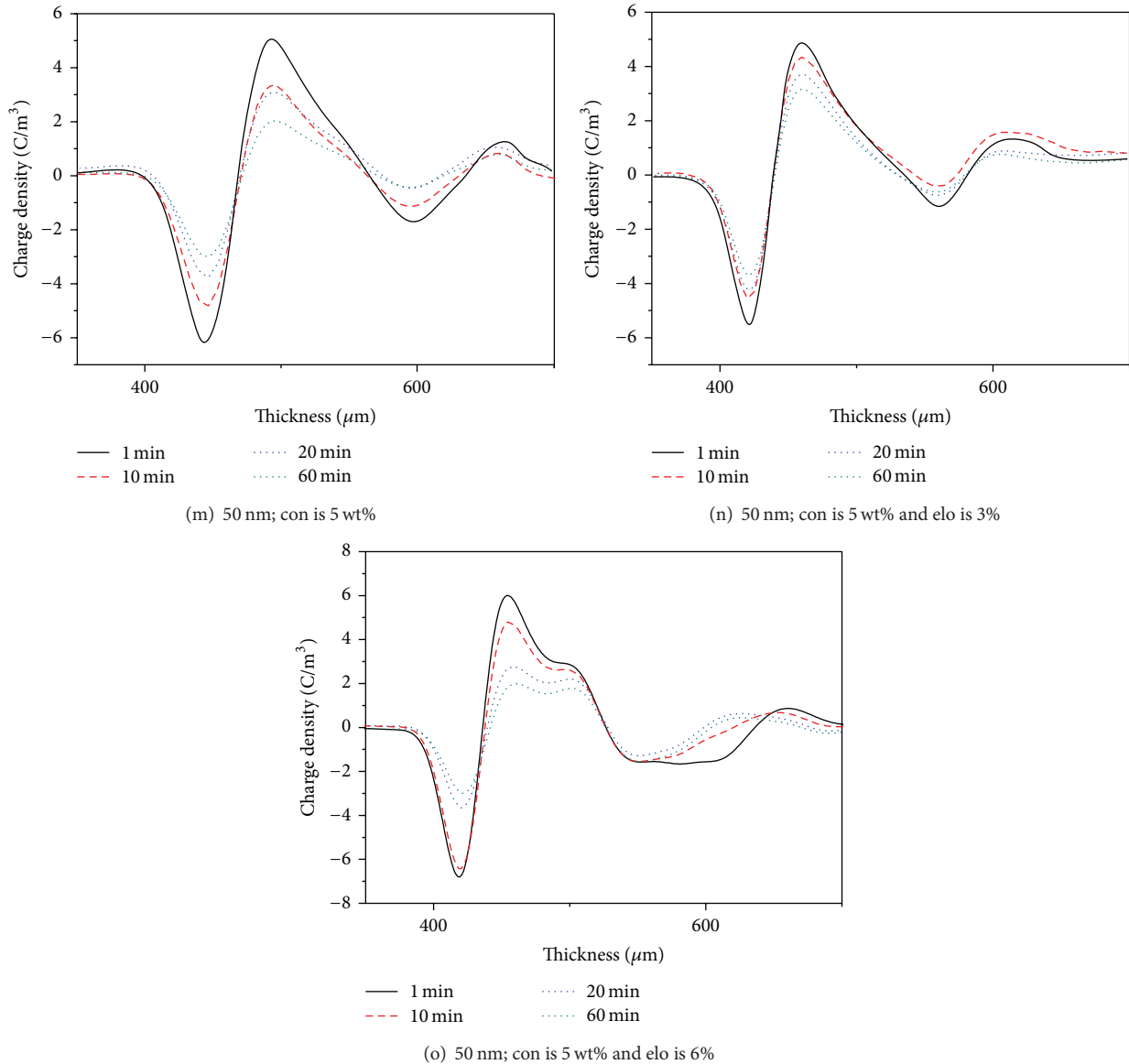


FIGURE 5: Detrapping characteristics of space charge (con represents concentration and elo represents elongation).

the particle size or concentration of nanoparticles is large, the total surface area in unit volume and the interface layer between nanoparticles and polymer matrix are also large. Therefore, the amount of space charge traps caused by the interface layer is also large, which makes the amount of space charge in the nanocomposites whose particle size is 50 nm become larger than that in the nanocomposites whose particle size is 15 nm.

A slightly obvious phenomenon was observed by analyzing the space charge characteristics of all nanocomposites, as shown in Figures 2(d), 2(g), and 2(j). The total amount of space charge accumulated near positive electrodes is larger than the space charge accumulated near negative electrodes in the nanocomposites. Triboelectricity can explain this phenomenon. According to the research of Tanaka et al. [16], triboelectricity exists in nanocomposites during the preparation process. Nanocomposites are negatively charged,

which may repel electrons. Of course, the effect of triboelectricity on the mobility of space charge is small and insignificant.

*4.2. Effect of Elongation on Space Charge in Polyethylene/Silica Nanocomposites.* No definite conclusions have been established regarding the status of nanoparticles in nanocomposites. The mode of action between nanoparticles and polymer matrix, the status of space charge traps in nanocomposites, and the inhibiting effect of nanoparticles on space charge remain unclear. According to the research of Takada et al. [17], many carbonyl (C=O) and hydroxyl (OH) defects exist in polymer; this existence may generate dipoles in a DC electric field which may cause dipole moments and electrical potential distribution. Electrical potential distribution can be regarded as space charge traps, and the value of the electric potential can be viewed as the depth of space

charge traps, to a certain extent. Takada et al. calculated the electrical potential distribution caused by dipoles. Their assumption was that the charge of carbonyl (C=O) and hydroxyl (OH) defects is  $q$  in polymer, and the distance between two dipoles is  $l$ . The dipole moments can be calculated by  $m = q * l$ . The electrical potential distribution,  $V(r, \theta, \phi)$ , is provided by (3) in spherical coordinates. Consider

$$V(r, \theta, \phi) = \frac{m \cos \phi}{\varepsilon_0 \varepsilon_r 4\pi r^2} \sin \theta, \quad (5)$$

where  $m$  is dipole moment,  $\varepsilon_0$  is absolute dielectric constant,  $\varepsilon_r$  is relative dielectric of polymer, and  $\phi$  and  $\theta$  represent spherical coordinates.

According to the test results of this study, as shown in Figure 2, the amount of space charge increases with the increase in elongation in the LDPE and nanocomposites. When the nanocomposites are in elongation, the distance between carbonyl (C=O) and hydroxyl (OH) defects is large. According to (3), the electrical potential distribution increases with the increase in distance  $l$ . This result indicates that the depth of space charge increases in nanocomposites. Therefore, the amount of space charge and deep traps increases.

According to the space charge characteristics of LDPE, as shown in Figure 3(a), the amount of space charge is larger near the electrodes than in the interior, which is roughly a trapezoidal decline. This result means that the surface of the LDPE may be vulnerable to elongation and carbonyl (C=O) and hydroxyl (OH) defects; the surface may have a larger elongation than the interior.

**4.3. Packet-Like Space Charge.** Small packet-like space charges were observed near positive and negative polarities in the polyethylene/silica nanocomposites whose particle size is 15 nm and concentration is 5 wt% when elongation is 10%. More obvious packet-like space charges were observed near positive and negative polarities in the polyethylene/silica nanocomposites whose particle size is 50 nm. The packet-like space charges are caused by deep traps in the polyethylene/silica nanocomposites, as revealed by the analysis of the dissipation characteristics. These phenomena can be explained from two aspects.

For polyethylene/silica nanocomposites, the assumption is that nanoparticles are spherical and the electric field is uniform. Hence, a certain amount of induction charges, which can be induced dipoles, exists at the surface of nanoparticles. Similarly, induced dipole moments and induction electromotive force exist. The surface charge density of dipole is [17]

$$\sigma_p = \varepsilon_0 E_0 \left( 1 - \frac{3\varepsilon_{r1}}{2\varepsilon_{r1} + \varepsilon_{r2}} \right) \cos \phi' \sin \phi', \quad (6)$$

where  $\varepsilon_0$  is absolute dielectric constant,  $\varepsilon_{r1}$  is dielectric constant of polymer, and  $\varepsilon_{r2}$  is dielectric constant of filler;  $\phi'$  represent spherical coordinates.

The electrical potential distribution,  $V(r, \theta, \phi)$ , is provided by (4) in spherical coordinates [17]. Consider

$$\begin{aligned} \frac{V(r, \phi)}{aE_0} &= \frac{1}{4\pi} \left[ 1 - \frac{3\varepsilon_{r1}}{2\varepsilon_{r1} + \varepsilon_{r2}} \right] \\ &\times \int_{-\pi}^{+\pi} \int_0^{+\pi} \frac{\sin^2 \theta' d\theta' \cos \phi' d\phi'}{\sqrt{1 + (r/a)^2 - 2(r/a) \sin \theta' \cos(\phi - \phi')}} \end{aligned} \quad (7)$$

where  $\varepsilon_0$  is absolute dielectric constant,  $\varepsilon_{r1}$  is dielectric constant of polymer and  $\varepsilon_{r2}$  is dielectric constant of filler,  $a$  is radius of particles,  $E_0$  is external field, and  $r, \theta', \phi', \phi$  represent spherical coordinates and more details are shown in [17, Figure 6].

When an external field  $E_0$  is applied to the nanocomposites, we can assume that the surface charge induced by  $E_0$  is positive on silicon atom and it is negative on oxygen atom. At the same time, because of the bond strength between silicon atom and oxygen atom, as the nanocomposites with elongation, the bond length of silicon atom and oxygen atom changes slightly. Therefore, the nanoparticles in polymer stressed by tensile force can also be supposed to be spherical whose diameter is larger than nanoparticles in polymer without tensile force. So (4) and (5) can also be appropriate. According to (5), relationships exist between electrical potential distribution and diameter of nanoparticles. This relationship means that when the diameter of nanoparticles is large, the electrical potential distribution and the depth of the space charge traps increase [17]. Therefore, stressed by tensile force, the space charge traps caused by electrical potential distribution change from shallow traps to deep traps. So it explains why there are more space charges in nanocomposites with elongations, which may induce packet-like space charge, as shown in Figures 3(b) and 3(c).

For the nanocomposites whose particle size is 15 and 50 nm, the diameter of nanoparticles increases with the increase in particle size. Therefore, according to (5), the electrical potential distribution of nanocomposites whose particle size is 50 nm is larger than nanocomposites whose particle size is 15 nm, which indicates that very obvious packet-like space charges exist in polyethylene/silica nanocomposites comparing with the polyethylene/silica nanocomposites whose particle size is 15 nm with small packet-like space charges, as shown in Figures 3(b) and 3(c).

However, the induced dipole model cannot completely explain the packet-like space charges. For the nanocomposites, no definite conclusion exists with regard to the types of force between nanoparticles and polymer matrix, which may be Van Edward force, covalent bond, molecular bond, or others. Several researchers believe that the type of force is a hydrogen bond in nanocomposites, which are prepared by mechanical blending [16]. Other researchers believe that the type of force is a covalent bond when vinylsilane is utilized to modify the interface of silica nanoparticles [18]. Considering the interface layer between nanoparticles and

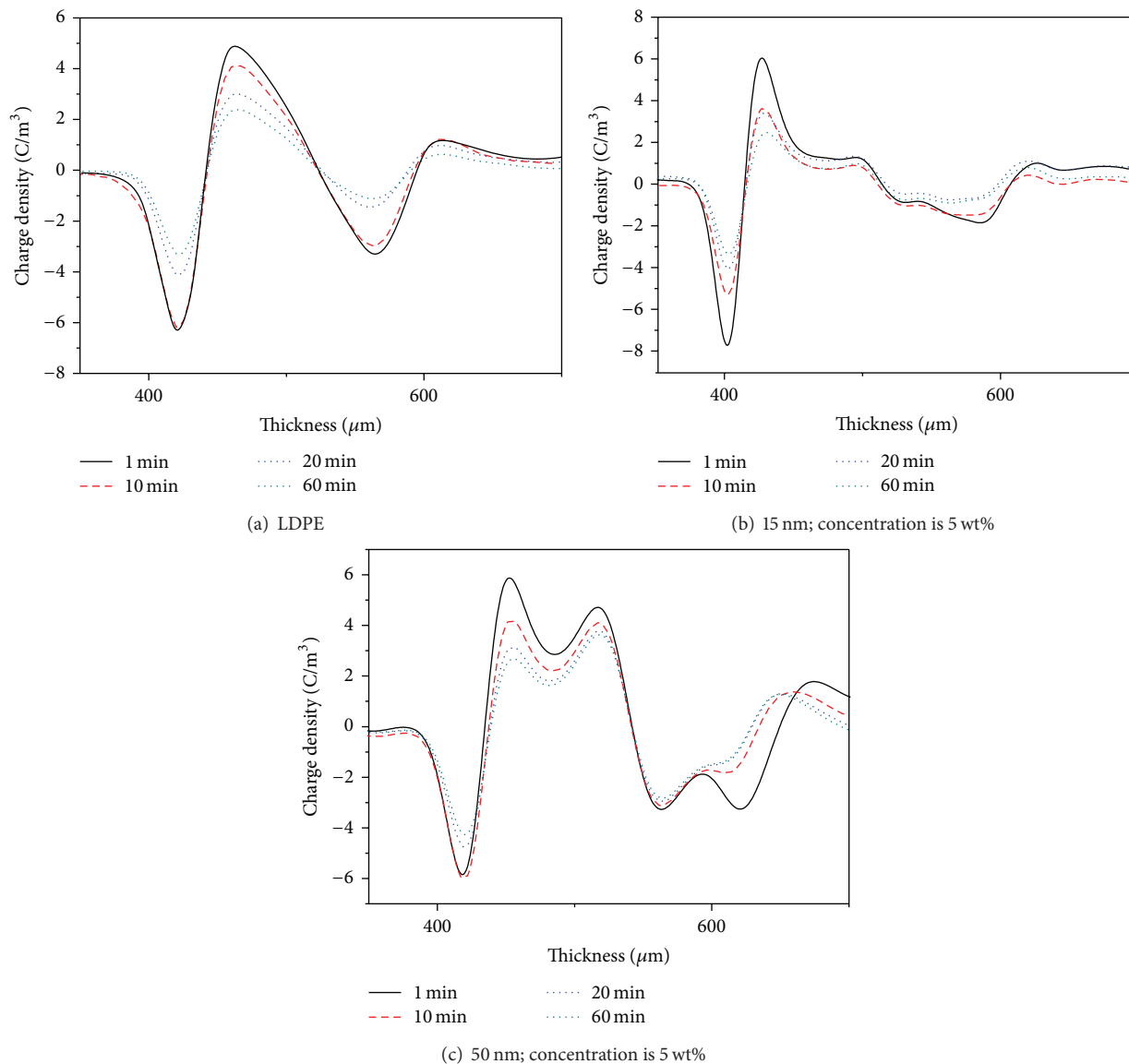


FIGURE 6: Detrapping characteristics of space charge with elongation of 10%.

polymer matrix, the force between polymer molecules can be regarded to be larger than the force between polymer matrix and nanoparticles. Therefore, the elongation between polymer matrix and nanoparticles is larger than the elongation between polymer molecules.

Owing to the interface layer characteristics, many shallow traps exist in the polyethylene/silica nanocomposites, which are distributed in the interface layer. There is a large increase in the interface layer when the nanocomposites are in elongation because of the small force between nanoparticles and polymer. Therefore, the area of the interface layer between nanoparticles and polymer matrix exhibits an obvious increase, which may change the shallow traps into deep traps and generate packet-like space charges.

According to the induced dipole model and interface layer characteristics, space charge accumulation should exist in all nanocomposites theoretically because the nanoparticles are distributed in all nanocomposites. However, the test

results in this study show that packet-like space charges exist in the interior of polyethylene/silica nanocomposites. This phenomenon can be explained by the repulsion of similar charges. The space charge near electrodes is forced to move to the interior of polyethylene/silica nanocomposites, which causes packet-like space charges.

## 5. Conclusions

This study investigated the space charge characteristics of polyethylene/silica nanocomposites whose elongation is 3% and 6%. The packet-like space charges in polyethylene/silica nanocomposites whose elongation is 10% were also examined. The main conclusions are as follows.

Suppressing the space charge in polyethylene/silica nanocomposites whose particle size is 15 nm and concentration is 3 wt% is effective. Homocharges near positive and negative electrodes are generated with the increase of particle size

and concentration in the polyethylene/silica nanocomposites. The interface layer characteristics between nanoparticles and polymer matrix were used to explain these phenomena. The effect of nanoparticles on space charge in polyethylene/silica nanocomposites is mainly caused by interface layer characteristics between nanoparticles and polymer matrix. By using (2), the total surface area in unit volume is  $0.872 \text{ km}^2/\text{m}^3$  in polyethylene/silica nanocomposites whose particle size is 50 nm; the total surface area in unit volume is  $2.8 \text{ km}^2/\text{m}^3$  in polyethylene/silica nanocomposites whose particle size is 15 nm. The difference is large. Therefore, the interface layer characteristics are the main reason for the effect of space charge characteristics in nanocomposites. The total surface area in unit volume increases with the increase in particle size and concentration.

With the increase in elongation, an obvious increase in space charge accumulation occurred in the three nanocomposites. The homocharges accumulated near electrodes in the LDPE and were reduced with the increase in depth of samples. A dipole model was used to explain this phenomenon. The electrical potential distribution caused by the dipole model, which consisted of carbonyl (C=O) and hydroxyl (OH) defects, can be regarded as the space charge traps in nanocomposites, to a certain extent. The bond length of the carbonyl (C=O) and hydroxyl (OH) defects may be larger when polyethylene/silica nanocomposites were in elongation. According to (3), the elongation of carbonyl (C=O) and hydroxyl (OH) defects caused the increase in electrical potential distribution, which in turn increased the amount of deep traps in polyethylene/silica nanocomposites and the amount of space charge.

Packet-like space charges were observed in polyethylene/silica nanocomposites whose particle size is 15 and 50 nm when elongation is 10%. The packet-like space charges are more obvious in the nanocomposites whose particle size is 50 nm. These phenomena can be explained from two aspects. First, induction charge exists on the surface of nanoparticles in the DC electric field; induced dipole and induction electromotive force are thus formed. The diameter of nanoparticles increases when nanocomposites are in elongation. According to (5), the amount of space charge and depth of charge traps increase with the increase in diameter of nanoparticles; this theory also explains why the amount of space charge increases with the increase in particle size. Second, the tensile force between nanoparticles and polymer matrix is weaker than that between polymer molecules because of the interface layer characteristics. Therefore, larger elongation exists between nanoparticles and polymer matrix, which may make the interface layer characteristics more obvious and could result in the generation of more charge traps. According to these theories, space charge is distributed in all nanocomposites. Packet-like space charges are created in polyethylene/silica nanocomposites because of the rejection of homocharges.

### Conflict of Interests

The authors declare that there is no conflict of interests regarding the publication of this paper.

### Acknowledgment

This research was supported by State Key Laboratory of Power Transmission Equipment & System Security and New Technology of China (2007DA10512713205).

### References

- [1] Y. Zhang, J. Lewiner, C. Alquié, and N. Hampton, "Evidence of strong correlation between space-charge buildup and breakdown in cable insulation," *IEEE Transactions on Dielectrics and Electrical Insulation*, vol. 3, no. 6, pp. 778–783, 1996.
- [2] S. Boggs, "A rational consideration of space charge," *IEEE Electrical Insulation Magazine*, vol. 20, no. 4, pp. 22–27, 2004.
- [3] J. K. Nelson, "Overview of nanodielectrics: insulating materials of the future," in *Proceedings of the Electrical Insulation Conference and Electrical Manufacturing Expo*, pp. 229–235, October 2007.
- [4] M. G. Danikas and T. Tanaka, "Nanocomposites—a review of electrical treeing and breakdown," *IEEE Transactions on Electrical Insulation Magazine*, vol. 25, no. 4, pp. 19–25, 2009.
- [5] K. S. Shah, R. C. Jain, V. Shrinet, A. K. Singh, and D. P. Bharambe, "High density polyethylene (HDPE) clay nanocomposite for dielectric applications," *IEEE Transactions on Dielectrics and Electrical Insulation*, vol. 16, no. 3, pp. 853–861, 2009.
- [6] Z. Li, Y. Yin, X. Dong, X. Li, and D. Xiao, "Effect of electrical stressing history on slow polarization behavior in composite of low-density polyethylene and nano-SiO<sub>x</sub>," *Japanese Journal of Applied Physics*, vol. 46, no. 9R, pp. 5908–5910, 2007.
- [7] A. Bulinski, S. S. Bamji, J. M. Braun, and J. Densley, "Water treeing degradation under combined mechanical and electrical stresses," in *Proceedings of the Conference on Electrical Insulation and Dielectric Phenomena, Annual Report*, pp. 610–617, Victoria, Canada, October 1992.
- [8] N. Amyot, E. David, S. Y. Lee, and I. H. Lee, "Influence of post-manufacturing residual mechanical stress and crosslinking by-products on dielectric strength of HV extruded cables," *IEEE Transactions on Dielectrics and Electrical Insulation*, vol. 9, no. 3, pp. 458–466, 2002.
- [9] F. Zheng, Z. Zhang, and C. Xiao, "Effect of applied mechanical stress on insulation of space charge breakdown," *Transactions of China Electrotechnical Society*, vol. 21, no. 2, pp. 31–34, 2006.
- [10] E. Ildstad, T. A. Lindseth, and H. Faremo, "Water treeing of XLPE cables during dynamic mechanical tension," in *Proceedings of the 19th IEEE International Symposium on Electrical Insulation (ISEI '12)*, pp. 628–631, San Juan, Puerto Rico, June 2012.
- [11] J. C. Fothergill, "Filamentary electromechanical breakdown," *IEEE Transactions on Electrical Insulation*, vol. 26, no. 6, pp. 1124–1129, 1991.
- [12] J. Wu, Y. Yin, L. Lan, Q. Wang, X. Li, and D. Xiao, "The influence of nano-filler concentration on space charge behavior in LDPE/silica nanocomposites," *Proceedings of the Chinese Society of Electrical Engineering*, vol. 32, no. 28, pp. 177–183, 2012.
- [13] J. Wu, Y. Yin, L. Lan, and et al, "Space charge trapping and conduction in low-density polyethylene/silica nanocomposite," *Japanese Journal of Applied Physics*, vol. 51, no. 4, Article ID 041602, 2012.
- [14] M. Meunier, N. Quirke, and A. Aslanides, "Molecular modeling of electron traps in polymer insulators: chemical defects and

- impurities," *The Journal of Chemical Physics*, vol. 115, no. 6, pp. 2876–2881, 2001.
- [15] T. J. Lewis, "Interfaces are the dominant feature of dielectrics at the nanometric level," *IEEE Transactions on Dielectrics and Electrical Insulation*, vol. 11, no. 5, pp. 739–753, 2004.
- [16] T. Tanaka, M. Kozako, N. Fuse, and Y. Ohki, "Proposal of a multi-core model for polymer nanocomposite dielectrics," *IEEE Transactions on Dielectrics and Electrical Insulation*, vol. 12, no. 4, pp. 669–681, 2005.
- [17] T. Takada, Y. Hayase, Y. Tanaka, and T. Okamoto, "Space charge trapping in electrical potential well caused by permanent and induced dipoles for LDPE/MgO nanocomposite," *IEEE Transactions on Dielectrics and Electrical Insulation*, vol. 15, no. 1, pp. 152–160, 2008.
- [18] M. Roy, J. K. Nelson, R. K. MacCrone, and L. S. Schadler, "Candidate mechanisms controlling the electrical characteristics of silica/XLPE nanodielectrics," *Journal of Materials Science*, vol. 42, no. 11, pp. 3789–3799, 2007.